Magnetotransport in Graphene and Related Two-dimensional Systems

Nathaniel Jian Huang

Hertford College, Oxford

Thesis submitted in fulfilment of the requirements
for the degree of
Doctor of Philosophy at the University of Oxford

Trinity, 2016

Magnetotransport in Graphene and Related Two-dimensional Systems

Nathaniel J. Huang, Hertford College, Oxford

Thesis submitted in fulfilment of the requirements for the degree of Doctor of Philosophy at the University of Oxford. Trinity, 2016

Abstract

This thesis describes studies on two-dimensional electron gases (2DEG) in graphene and related 2D systems. Magnetotransport investigations specifically in graphene and its bilayer system are demonstrated in detail, while the experimental techniques presented in this thesis are widely applicable to a large variety of other 2D materials.

Chapter 1 gives an introduction and motivation for the principal topic presented in this thesis, with a general introduction to carbon nano-materials and an overview of the current state of graphene-related research and technological development (RTD). Chapter 2 establishes a basic theoretical framework which is essential for interpreting the results presented in this thesis, starting with the crystal and electronic band structures of graphene and its bilayer, followed by high magnetic fields effects on transport properties in these 2D systems. Chapter 3 details the experimental methods directly related to the presented work.

The next three chapters report experimental results of three specific magnetotransport studies. Chapter 4 reports the disorder effects on epitaxial graphene in the vicinity of the Dirac point. Quadratic increases of carrier densities with temperature are found to be due to intrinsic thermal excitation combined with electron-hole puddles induced by charged impurities. It is also shown that the minimum conductivity increases with increasing disorder strength, in good agreement with quantum-mechanical numerical calculations. Chapter 5 reports measurements of the quantum Hall effect in epitaxial graphene showing the widest quantum Hall plateau observed to date extending over 50 T, attributed to a magnetic field dependent charge transfer process from charge reservoirs with exceptionally high densities of states in close proximity to the graphene. Using a realistic framework of broadened Landau levels this process is modelled in excellent agreement with experimental results. In Chapter 6, energy relaxation of hot carriers in graphene bilayer systems is investigated from measurements on Shubnikov-de Haas oscillations and weak localisation. The hot-electron energy loss rate follows the predicted T^4 power-law at carrier temperatures from 1.4 up to about 100 K, due to electron-acoustic phonon interactions. Comparisons are made between graphene monolayer and bilayer systems and a much stronger carrier density dependence of the energy loss rate is found in the bilayer system.

This thesis concludes with a summary of the most important findings of the topics that have been discussed. The significance and limitations of the present research are listed. Some suggestions and outlook are given for possible improvements and interesting areas of future research and development.

Acknowledgements

I would like to take this opportunity to record my heartfelt appreciation to all those who have helped me in any way during my studies and made this thesis possible.

Firstly I would like to thank my supervisor, Prof. Robin J. Nicholas, for his unwavering support and guidance. His enthusiasm and patience in teaching students, his rigorous attitude towards research, his immense knowledge in all aspects of physics and passion for passing it on have always encouraged me to become a better academic and a better person overall.

I am thankful for the opportunities that brought me into association with many brilliant researchers in the Nicholas Research Group. In particular I would like to thank Jack Alexander-Webber who trained me to operate almost every piece of equipment and shared his invaluable experience and expertise in the lab, and for his entertaining fine arts as well as the very much enjoyable speakers and chair combo he left when he moved to "the other place". Thanks to Samuel Stranks, Beate Dirks, Severin Habisreutinger, Jacob Wang, Joseph Sharkey, Giulio Mazzotta and Markus Dollmann for exchanging their ideas and insights about carbon nanotubes, porphyrins, perovskites, photovoltaics and various spectroscopy experiments at the group meetings, which I find extremely interesting and useful. Thank you all for many fond memories during our mutual days in the Clarendon Laboratory.

I am also grateful for the good fortune of having such amazing support staff in the Department of Physics, University of Oxford. I would not have been able to run my experiments smoothly (or have some lab-made ice cream) without the help and cryogenic supplies from Robert Storey, Tony Hickman and Kieran McCall in the Cryomagnetics Group. Many thanks to Paul Pattinson for keeping the cleanroom in the Denys Wilkinson Building as tidy and user-friendly as possible, and also for occasionally helping me wire-bond my fragile devices. Not forgetting Johan Fopma from the Central Electronics

Group who spent hours trying to fix various broken electronics in the lab.

While members in the Nicholas, Herz, Johnston, Snaith, Riede and Taylor groups in the Condensed Matter Physics sub-department have formed a diverse and interactive scientific community of Semiconductor Materials, Devices and Nanostructures, which I feel lucky enough to be a part of, Hertford College, on the other hand, has provided me with a pleasant place to relax and meet more friends. Many thanks to Elias de Hertford for founding something in 1282 which turned out to be sparklingly beautiful. A special thank you to the late Simpkin IV for your cute and soothing tail wags in the college quads.

I am most grateful to my collaborators outside of Oxford, for synthesising and providing wonderful high-quality samples at the same time contributing enormous effort to the projects. They are, JT Janssen and Sasha Tzalenchuk from the National Physical Laboratory (UK); Vladimir Antonov from Royal Holloway, University of London (UK); Tom Yager, Samuel Lara-Avila and Sergey Kubatkin from Chalmers University of Technology (Sweden); Rositsa Yakimova from Linköping University (Sweden); Rachael Myers-Ward, Virginia Wheeler and Kurt Gaskill from the US Naval Research Laboratory; and Duncan Maude from Laboratoire National des Champs Magnétiques Intenses (France). The projects in the UK were mainly supported by the UK EPSRC, the EU Graphene Flagship and the EMRP project GraphOhm. I also wish to acknowledge with gratitude the financial support from the China Scholarship Council.

I wish to thank my friends and colleagues who have kindly and enthusiastically read my typescripts, pointed out many errors, and gave me invaluable criticism and advice during my writing. Among others, Juliane Gong (Condensed Matter Physics, University of Oxford), Yufei Ji (Economics, McGill University) and Chuang Sun (Theoretical Physics, University of Oxford) are immortalised here. I am extremely grateful to all of my friends for their continuous support and companionship, the excellent food and drinks, the great adventures, and those countless happy times.

My final thanks go to my parents and grandparents, for their tremendous support and encouragement, for their unconditional love, and for millions of other things.

"What's the use of a good quotation if you can't change it?"

The Doctor

Publications

J. T.-W. Wang, J. M. Ball, E. M. Barea, A. Abate, J. A. Alexander-Webber, **J. Huang**, M. Saliba, I. Mora-Sero, J. Bisquert, H. J. Snaith, and R. J. Nicholas. Low-temperature processed electron collection layers of graphene/TiO_2 nanocomposites in thin film perovskite solar cells. *Nano Letters*, **14**, 724, (2014).

J. J. Sharkey, S. D. Stranks, **J. Huang**, J. A. Alexander-Webber, and R. J. Nicholas. Engineering nanostructures by binding single molecules to single-walled carbon nanotubes. *ACS Nano*, **8**, 12748, (2014).

J. Huang, J. A. Alexander-Webber, T. J. B. M. Janssen, A. Tzalenchuk, T. Yager, S. Lara-Avila, S. Kubatkin, R. L. Myers-Ward, V. D. Wheeler, D. K. Gaskill, and R. J. Nicholas. Hot carrier relaxation of Dirac fermions in bilayer epitaxial graphene. *Journal of Physics: Condensed Matter* **27**, 164202 (2015).

V. Babenko, A. T. Murdock, A. A. Koós, J. Britton, A. Crossley, P. Holdway, J. Moffat, **J. Huang**, J. A. Alexander-Webber, R. J. Nicholas, and N. Grobert. Rapid epitaxy-free graphene synthesis on silicidated polycrystalline platinum. *Nature Communications* **6**, 7536 (2015).

J. Huang, J. A. Alexander-Webber, A. M. R. Baker, T. J. B. M. Janssen, A. Tzalenchuk, V. Antonov, T. Yager, S. Lara-Avila, S. Kubatkin, R. Yakimova, and R. J. Nicholas. Physics of a disordered Dirac point in epitaxial graphene from temperature-dependent magnetotransport measurements. *Physical Review B* **92**, 075407 (2015).

M. Saliba, S. M. Wood, J. B. Patel, P. K. Nayak, **J. Huang**, J. A. Alexander-Webber, B. Wenger, S. D. Stranks, M. T. Hörantner, J. T.-W. Wang, R. J. Nicholas, L. M. Herz, M. B. Johnston, S. M. Morris, H. J. Snaith, and M. K. Riede. Structured organic-inorganic perovskite toward a distributed feedback laser. *Advanced Materials* **28**, 923, (2016).

J. A. Alexander-Webber, **J. Huang**, D. K. Maude, T. J. B. M. Janssen, A. Tzalenchuk, V. Antonov, T. Yager, S. Lara-Avila, S. Kubatkin, R. Yakimova, and R. J. Nicholas. Giant quantum Hall plateaus generated by charge transfer in epitaxial graphene. *Scientific Reports* **6**, 30296, (2016).

J. T.-W. Wang, Z. Wang, S. Pathak, W. Zhang, D. W. deQuilettes, F. Wisnivesky, **J. Huang**, P. Nayak, J. Patel, H. Yusof, Y. Vaynzof, R. Zhu, I. Ramirez, J. Zhang, C. Ducati, C. Grovenor, M. B. Johnston, D. S. Ginger, R. J. Nicholas, and H. J. Snaith. Efficient perovskite solar cells by metal ion doping. *Energy & Environmental Science* **9**, 2892, (2016).

Manuscripts in preparation/submitted

J. A. Alexander-Webber, **J. Huang**, C. Drasar, R. J. Nicholas, and A. I. Coldea. Two band magnetotransport in exfoliated thin films of $Cu_{0.2}Bi_2Se_3$ topological insulators. *in preparation.*

Contents

1 Introduction

This chapter gives an introduction and motivation for the principal topic presented in this thesis, graphene and related two-dimensional systems. What graphene is and its relation to carbon is introduced. Some of the most unique properties of graphene, and examples of different types of graphene-related 2D systems are discussed. This chapter closes with a brief overview of the current research and development on graphene-based technologies.

Contents

1.1 Introduction and Motivation

Semiconductors have been known and experimented with since the mid-19th century, however, it was not until 1947 the year when Bell Labs built the first transistor, the point-contact germanium transistor [1], that the significant impact of semiconductors on people's lives started to show. While the first transistor was made using germanium, silicon transistors were soon demonstrated to be more reliable as silicon has a larger bandgap [2]. Since then, the development of silicon-based semiconductor technologies has blossomed into the most important driving force in the information age, hence also known as the age of silicon.

Gordon Moore, Intel's co-founder, in 1965 predicted that the density of transistors in integrated circuits such as processors would double every year [3], with his modification later on in 1975 [4] to every two years. This prediction (Moore's law) has been accurate and exceptionally successful in guiding the semiconductor industry and research pace in the last five decades (Figure 1.1). However, from the first transistor to Intel's latest 14 nm FinFET transistors with a 3D tri-gate structure (Figure 1.2), keeping Moore's

law going is becoming more and more challenging. Despite the constantly increasing development costs for even faster processors and silicon's relatively low carrier mobility, the biggest challenge in silicon transistors lies in limiting the leakage power, which is also coupled with heat management, stability and controllability of such devices. To tackle these problems and improve performance, in addition to designing more sophisticated nanostructures such as FinFETs, novel materials as replacement of silicon are highly sought after.

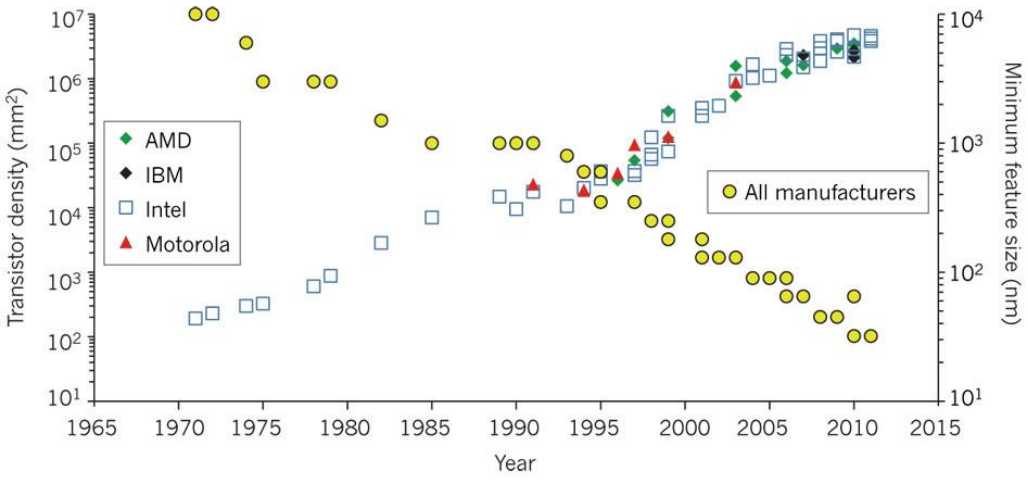

Figure 1.1: Transistor densities and minimum feature size in processors produced by main manufacturers from 1970s to 2010s. Adapted from Ref. [5].

The discovery of graphene [6], a truly two-dimensional material made of carbon atoms, has shed some light on the future development of semiconductors. Due to the two-dimensional nature with ultra-high in-plane thermal conductivity [7] and carrier mobility [8] in graphene, it has the potential to replace silicon for ultra-fast, smaller and more efficient transistors as building blocks of many next generation electronics. Apart from exceptional electronic and thermal properties, graphene also possesses many remarkable mechanical [9] and optical properties [10] which can be utilised to enable smarter devices and applications. More excitingly, recent advances in the graphene research also triggered numerous studies and developments in graphene-related two-

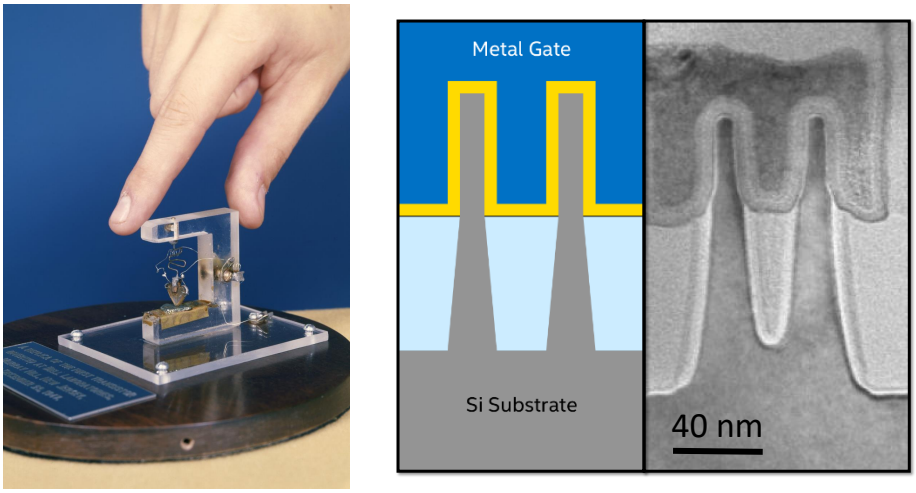

Figure 1.2: Replica of the world's first transistor invented in 1947 (left) and Intel's 2nd generation 14 nm tri-gate transistor commercialised in 2014 (right).

dimensional systems such as multilayer stacks of graphene, other families of 2D materials, as well as hybrid and heterostructure of these 2D materials, whose unique properties may be essentially complementary to those of graphene, as certain drawbacks related to graphene's electronic structure and synthesis techniques are currently hindering its direct incorporation into electronics [11–13]. Therefore, even though graphene may not yet be able to revolutionise semiconductor industry, with constant research and development of technologies designed specifically around graphene and graphene-related 2D materials, the age of carbon is nearing.

1.2 From carbon to graphene

1.2.1 Carbon in three dimensions

Carbon is the sixth chemical element in the periodic table and is probably the sixth earliest element exploited by mankind, dating back to as early as 3750 BCE [14], in the

form of charcoal to reduce copper ores in order to produce bronze. The true chemical analyses of carbon as an element, however, were not made until the late-18th century. Carbon is the 4th most abundant element in the universe and the 15th in Earth's lithosphere by mass. It originates mostly from the nucleosynthesis process in large stars, like many other light elements, with certain possibility to be produced in small stars by the α process [15, 16].

Atoms of carbon can be bonded together in many different ways. In our three-dimensional world, the best known natural allotropes are amorphous carbon, diamond and graphite, with physical properties vastly different from each other. In order to understand their differences, it is necessary to discuss carbon's electronic configuration. Each carbon atom has six electrons with two of them forming a filled $1s^2$ shell and the rest forming a configuration of $2s^2 2p_x^1 2p_y^1$ at the ground state. The energy required to excite one 2s electron into an empty $2p_z$ state is approximately 4.2 eV [16]. When molecules or solids are formed, the total energy of the system decreases due to spatial overlap of the electron wave functions (chemical bonds) of the consisting atoms, forming molecular orbitals in molecules and energy bands in solids. In the case of carbon, one at first glance may expect the formation of two covalent bonds utilising the partially filled $2p_x$ and $2p_y$ orbitals, however, this is not true since the energy released when forming bonds by mixing (hybridising) the 2s orbital with one, two or three 2p orbitals is more than enough to compensate the excitation energy required. Therefore, this energetically favoured orbital hybridisation process would always occur when forming metastable carbon-based substances. The three types of hybridisation processes, namely sp, sp^2 and sp^3, are shown in Figure 1.3.

In sp^3 hybridisation, all three 2p orbitals are hybridised with the 2s orbital, forming four equivalent sp^3 orbitals tetrahedrally coordinated with an angle of 109.5° from each other. In sp^2 hybridisation, only the $2p_x$ and $2p_y$ orbitals are hybridised with the 2s orbital, forming three equivalent sp^2 orbitals triangularly coordinated in the x-y plane

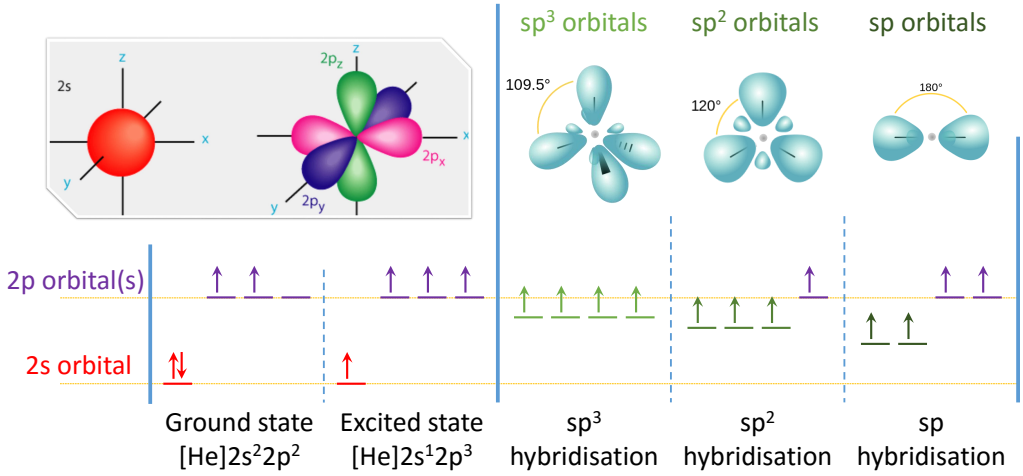

Figure 1.3: Electron configuration and orbital hybridisation of carbon.

with an angle of 120° from each other; the $2p_z$ remains un-hybridised. In sp hybridisation, only the $2p_x$ orbital is hybridised with the 2s orbital, forming two equivalent sp orbitals linearly coordinated in the x direction with an angle of 180° from each other; both the $2p_y$ and $2p_z$ remain un-hybridised. The covalent bond formed by end-to-end overlapping of orbitals (such as by the sp, sp^2 or sp^3 hybridised orbitals) is called the σ-bond and that by side-by-side overlapping of orbitals (such as by the un-hybridised p orbitals) is called the π-bond. In a simplified picture, the characteristics of these hybridised orbitals can also be viewed as linear combinations of those of the original un-hybridised orbitals, i.e., sp^3 = 25% s + 75% p, sp^2 = 33% s + 67% p, and sp = 50% s + 50% p. The above formulae are not entirely accurate but are qualitatively true and can be particularly useful when comparing the strengths and lengths of the carbon-carbon σ-bonds. As mentioned above, a 2p orbital is much higher in energy than a 2s orbital. Consequently, the sp^3-sp^3 σ-bond is the weakest with the longest bond length, while the sp-sp σ-bond is the strongest with the shortest bond length.

With all the above information in mind, we now proceed to examine some of the basic properties of the three well-known natural allotropes of carbon in three dimensions

shown in Figure 1.4.

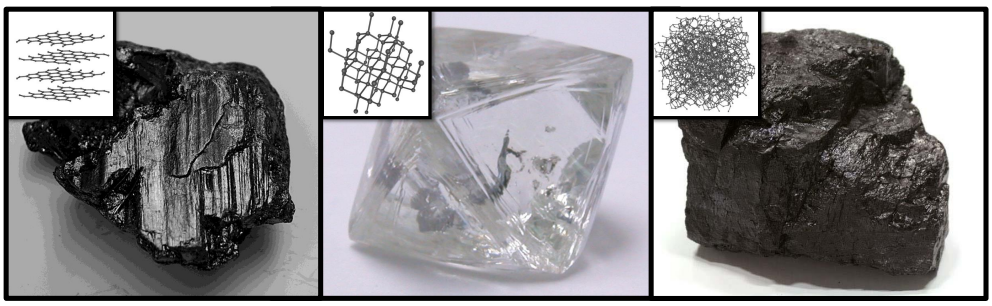

Figure 1.4: Photos of three main types of 3D carbon allotropes: natural graphite (left), raw diamond (middle) and bituminous coal (right), with top-left insets showing their structures.

Graphite In the form of sp^2 hybridisation, graphite is the most stable allotrope of carbon. Graphite has a layer-by-layer structure. Within each layer, carbon atoms are arranged in a honeycomb lattice connected by the in-plane sp^2 σ-bonds. Above and below the layer, π-bonds are formed with the electron wave function delocalised, making graphite electrically and thermally conductive along the planes. These π-bonds also help to create van der Waals bonds between each layer to keep them stacked together. Since van der Waals bonds originate from induced electric dipoles, electrical and thermal conductivities in the direction perpendicular to layers in graphite are relatively poor. Graphite can be often found in metamorphic rocks, igneous rocks and meteorites, and has been used widely in pencils, in batteries as anodes, and as refractories, lubricants, etc [17]. As will be shown later in this chapter, graphene is essentially one isolated layer from graphite and graphene multilayer is just a very thin portion of graphite.

Diamond Diamond is formed by sp^3 σ-bonds connecting carbon atoms, thus creating a three-dimensional tetragonal structure. Even though the sp^3 σ-bonds in diamond are not as strong as the sp^2 σ-bonds in graphite, their three-dimensionality has proven to be extremely rigid, with very few impurities and defects present in the crystal. Dia-

mond is one of the hardest and most thermally conductive materials. It also possesses remarkable optical properties [17, 18]. Diamond is an excellent electrical insulator with a wide bandgap of 5.5 eV [19]. Large, high quality diamond is usually regarded as one of the most desirable gemstones, while small and less pure diamond crystals are often found useful as cutting and polishing tools [17].

Amorphous carbon In amorphous carbon, unlike graphite or diamond, no crystalline order is present. Therefore, it is normally considered to be a random network of sp^2 and sp^3 sites [20]. In nature, amorphous carbon often refers to coal and soot. However, they are not true amorphous carbon since they, strictly speaking, are simply polycrystalline materials consisting of graphite-like and diamond-like crystals in a random matrix, not to mention the fact that they usually contain a considerable amount of non-carbon impurities.

1.2.2 Low-dimensional carbon allotropes

For thousands of years, known allotropes of carbon have been limited to the three-dimensional forms introduced above. With recent advances in physics, chemistry and materials science during the last few decades, series of low-dimensional carbon allotropes have been discovered. Ranging from the zero-dimensional fullerene, the one-dimensional carbon nanotube, to the two-dimensional graphene (see Figure 1.5), these low-dimensional allotropes have significantly expanded the carbon family.

Fullerene Fullerene is the name for a series of carbon molecules which have spherical or sometimes ellipsoidal structures formed by single surface of carbon atoms. It normally contains pentagonal and hexagonal rings with adjacent rings sharing a common polygon edge representing covalent carbon-carbon σ-bonds. In order to adapt the

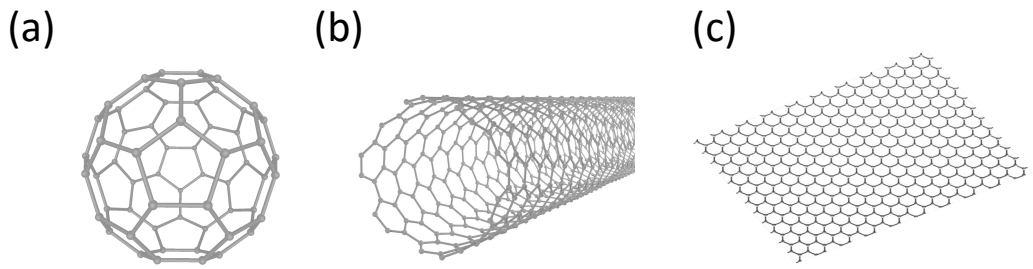

Figure 1.5: Structure of (a) fullerene, (b) carbon nanotube, and (c) graphene.

curvature, these σ-bonds have a few different bond lengths with characteristics between sp^3 and sp^2 (predominant) bonds [21]. The first fullerene discovered in 1985 is C_{60} as it is made of 60 carbon atoms forming 20 hexagons and 12 pentagons [22], for which the 1996 Nobel Prize in Chemistry was awarded. The name "fullerene" and its nickname "buckyball" are all derived from Richard Buckminster "Bucky" Fuller, an American architect and designer, whose design of a geodesic dome structure bears a strong resemblance to C_{60}. Apart from C_{60}, many other fullerenes, such as C_{70}, C_{76}, C_{62} and C_{84} were later discovered. The diameter of a fullerene molecule, depending on its composition, can normally vary from about 1 nm to 100 nm [23]. Since electron motion is confined in such small structures, fullerene is considered to be a zero-dimensional semiconductor and often regarded as a quantum dot. Fullerenes and modified fullerenes have been used extensively in optoelectronics [24], quantum computing [25] and biomedical applications [26].

Carbon nanotube Carbon nanotubes have cylindrical structures which are formed by hexagons of carbon atoms. They were discovered in 1991 [27] during an arc discharge experiment which used graphite electrodes intended to produce fullerenes. The walls of a carbon nanotube can be viewed as rolled up carbon layers in graphite, therefore are entirely composed of sp^2 bonds. Depending on the number of carbon layers involved, carbon nanotubes can be categorised as single-walled carbon nanotubes (SWCNTs) and

multi-walled carbon nanotubes (MWCNTs). While MWCNTs are normally metallic, SWCNTs, on the other hand, can be semiconducting or metallic depending on the angle by which the single graphite layer is rolled up. Most SWCNTs have a diameter around 0.7 to 2 nm, while that of MWCNTs can be as large as 100 nm [28]. Carbon nanotubes can also be pictured as stretched fullerene, since both ends of a carbon nanotube are usually capped by structures similar to fullerene hemispheres [29]. However, the length of a carbon nanotube can be centimetres long, with extremely large length-to-diameter ratios over 100,000,000:1 [30]. Since electrons can be delocalised along the tubes over a large distance but are confined around their small circumferences, carbon nanotubes are one-dimensional carbon allotropes. Because of their superior mechanical, thermal, electrical and optical properties, with current annual production exceeding several thousand tons, carbon nanotubes find themselves eminently useful for applications such as in energy generation and storage, structural and biomedical parts, water filtration, electronics and optoelectronics, coatings, etc [31].

Graphene A material made of single layer of sp^2-hybridised carbon atoms, densely packed in a two-dimensional honeycomb lattice with π-bonds on top and bottom of the layer, graphene was first isolated in 2004 [6], by Andre Geim and Konstantin Novoselov at the University of Manchester, for which they were awarded the 2010 Nobel Prize in Physics. The isolation technique used is commonly known as the Scotch tape method, which is essentially using two pieces of sticky tapes to repeatedly peel off graphite layers, since structurally graphene is simply a single carbon layer of graphite. A detailed description of this technique can be found in Section 3.1.1. The discovery of graphene has sparked intensive study of its exceptional optical, electronic, mechanical and thermal properties. Graphene, as a single atomic sheet, can only/already absorb about 2.3% of incident light in the visible range [32]. Graphene is a zero-bandgap semiconductor, with electrons propagating through the lattice with effectively zero mass [33]. Graphene is

light and flexible, being the thinnest and yet the strongest material known to mankind, with intrinsic tensile strength 200 times higher than that of steel [9]. Graphene's thermal conductivity at room temperature [7] is more than 10 times higher than that of copper or silver. The combination of these superior properties in such a large variety makes graphene a truly amazing 2D material. Re-examining the history of semiconductor industry and the slow development of fullerene- and carbon nanotube-based technologies, fully utilising graphene's capability in the next few years, particularly in fulfilling emerging needs for flexible electronics and portable energy conversion/storage devices, seems to be a challenging task, however, with much more effort being devoted to its fundamental research, industrial production, technology innovation, marketing and politics, goals may be reached sooner than people imagine.

The following schematic diagram (Figure 1.6) is to summarise the evolution between graphite, graphene, carbon nanotubes and fullerene, being 3D, 2D, 1D and 0D carbon allotropes, respectively.

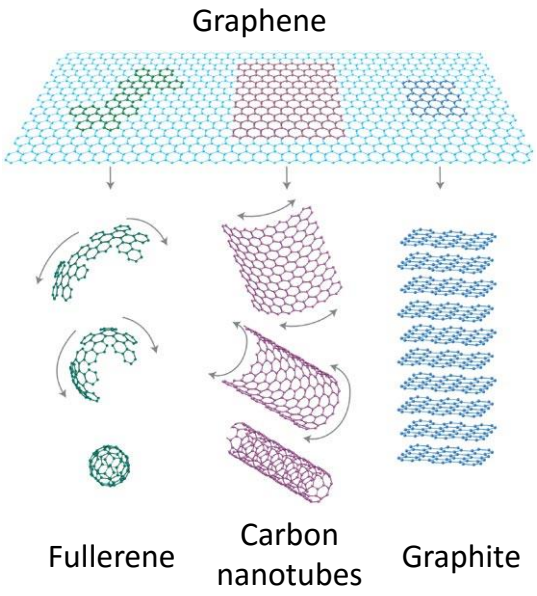

Figure 1.6: Evolution between the 3D graphite, the 2D graphene, the 1D carbon nanotubes and the 0D fullerene. Adapted from Ref. [8].

1.3 Graphene-related 2D systems

Despite that graphene possesses many exceptional properties, it is clear that it has its own limits rather than being an almighty material that can only come out in science fiction. Along with the research and development of graphene, more and more varieties of graphene-related 2D materials are being isolated and synthesised. Some of these 2D materials with their unique properties, may eventually replace graphene for certain applications, or be engineered to form hybrid nanostructures complementing graphene, to provide desired functionalities. This section introduces some of the graphene-related 2D systems that have been most extensively explored.

1.3.1 Multilayer graphene

Multilayer or few layer graphene generally refers to stacks of graphene of ten layers or less. They have distinctive electronic structures compared with single layer graphene and the 3D graphite [34], but due to their small number of layers, the 2D electron confinement is still present.

One of the most interesting systems in this category is bilayer graphene. While similar to single layer graphene in many ways, bilayer graphene is a semiconductor in which a band-gap can be opened and continuously tuned such as by doping [35] and applying electric fields perpendicular to its surface [36, 37]. Different stacking orientations of the two constituent layers can also result in different electronic structures in bilayer graphene [38], creating new possibilities for designing novel electronic devices. Those stacking orders are described in detail in Section 2.1.2.

For multilayer stacks with three or more graphene layers, the electronic structure can be effectively decomposed into subsystems using a basis containing that of single layer and bilayer graphene [34]. One of the main expectations utilising these materials is to

replace indium tin oxide (ITO) as transparent conductors in, for example, photovoltaics, displays and touch panels, with the advantages including being cost-effective and flexible.

1.3.2 2D materials beyond graphene

Apart from graphene and its multilayer which are all made of carbon, the number of reported other 2D materials has been rapidly increasing over the last few years. Some of these materials can be directly exfoliated from their bulk crystals following similar techniques used in the isolation of graphene, and some of them can be synthesised via other bottom-up deposition methods [12]. Characterisation techniques of these materials, as described in Chapter 3, are also to a large extent identical to what applies to graphene.

One class of these materials are 2D allotropes of other elements. Silicene [39], germanene [40] and stanene [41] made of silicon, germanium and tin atoms, respectively, with honeycomb lattice structures similar to that of graphene have been theoretically explored, but their free-standing forms are yet to be synthesised. Phosphorene is a 2D allotrope of phosphorus, a single layer of black phosphorus. It is much less air stable than graphene, but can be exfoliated using the Scotch tape method in a controlled environment. Phosphorene has attracted much attention recently since being successfully isolated in 2014 [42–44]. Different from graphene, it possesses a non-zero band gap and still has relatively high electron mobility, potentially more suitable than graphene for making transistors.

Another class of 2D materials are compounds. Single layer hexagonal boron nitride (h-BN) [45] made of alternating nitrogen and boron atoms, is a good insulator. Transition metal di-chalcogenides (TMDs) [46], with the typical composition MX_2, where M is a transition metal element (e.g. Mo, W) and X is a chalcogen element (e.g. S, Se and Te), often have direct band-gaps and strong spin-orbit coupling, making them poten-

tially useful in optoelectronics and spintronics. Other 2D compounds, such as indium selenide, bismuth selenide and bismuth telluride, also exhibit extraordinary properties significantly different from their bulk materials which can be semiconductors, superconductors and topological insulators [12].

1.3.3 Heterostructures of 2D materials

When it comes down to designing new devices for novel applications using 2D materials, elaborately tailored heterostructures are often required. These heterostructures in general can be categorised into two types, vertical and lateral heterostructures [12, 47, 48], as shown in Figure 1.7. Vertical heterostructures can be realised by mechanically stacking different 2D materials in a controllable fashion on demand. They can offer new prospectives in tunnelling devices as well as encapsulating, gating and electronically modifying certain active layers from which main functionalities are expected. Lateral heterostructures are typically formed by sequential growth of different 2D materials. Common 2D heterostructures which have been obtained experimentally are graphene/h-BN [49, 50] vertical structures, $MoS_2/MoSe_2$, MoS_2/WS_2, WS_2/WSe_2 lateral heterojunctions [48, 51]. In addition to experimental advances in fabricating these heterostructures, development of new simulation models of electronic interactions in such systems is equally important [12], in furtherance of fundamentally understanding and predicting their electron transport and optical properties.

1.4 Graphene-related RTD: an overview

This section overviews recent progress in graphene-related research and technological development. Over the past 12 years, since graphene was discovered in 2004, the number of published research papers and patents have shown nearly exponential increases world-

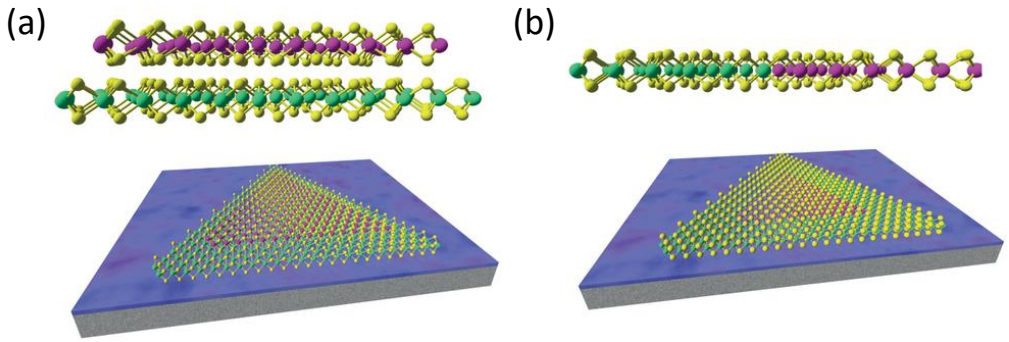

Figure 1.7: Structure of (a) vertical and (b) lateral heterojunctions formed by TMDs. Green, pink and yellow spheres, for example, can represent Mo, W and S atoms, respectively. Adapted from Ref. [48].

wide (see Figure 1.8) with more than 10,000 publications of both papers and patents expected in 2016 alone. Behind these figures are a global gold rush in science and technologies towards disruptive applications potentially promised by novel properties of graphene and related 2D materials.

An analysis reveals that China has become a dominant force by owning about 44% of the world's graphene publications [53] and 47% of the patents [52]. This achievement has been enabled by its policies on the new materials industry. In 2013, the China Innovation Alliance of the Graphene Industry was established, with the support of several major bodies of the Chinese government and international collaborations with universities and entrepreneurs. Five industrial parks focusing on industrialisation of graphene have since been set up in order to accelerate this process. Following closely behind are the US and South Korea. Samsung (Korea) stands out by being the top patent applicant in the world with over 400 patent families. IBM (USA) has also been active in this field, holding over 200 patents [52].

European countries, on the other hand, have been significantly less dominant in terms of the total amount of patent and paper publications [52, 53], despite the fact that graphene was first isolated and with its fundamental properties discovered in the

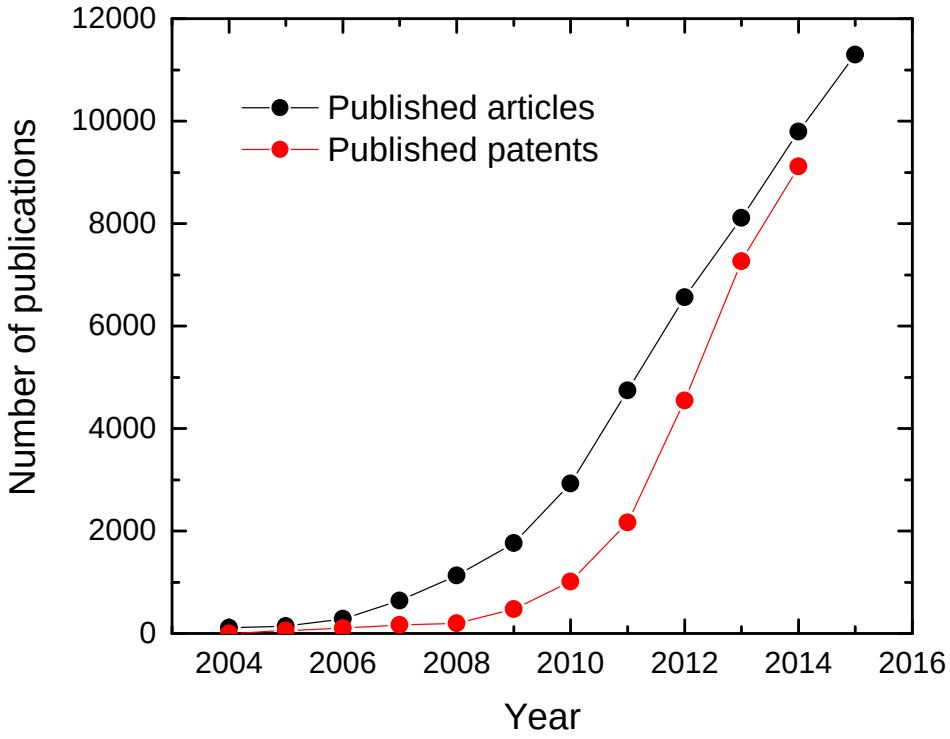

Figure 1.8: Number of annually published research articles (red) and patents (black) in the world from 2004 to 2015. The black data set is obtained from Web of Science by counting the number of SCI articles that contains "graphene" in title. The red data set is taken from Ref. [52].

UK. However, research quality in the EU, accessed by the mean number of citations per research paper, is much superior than that of China. The University of Manchester (UK) has the highest score of about 260 compared to only 25 for the Chinese Academy of Science [53]. From another perspective, when the number of publications is normalised taking into account of national populations, UK then has a significant graphene-related RTD output effectively equivalent to the US and almost twice higher than China. In the meantime, the RTD in Europe is certainly having a boost by Europe's biggest ever research initiative, the Graphene Flagship, with a budget of 1 billion euros by the European Commission to fund over 10 years of graphene-related research commenced in 2013. The current projects of the Graphene Flagship contain four science divisions and 20 work packages in total, with missions including but not limited to fundamental re-

search, scalable synthesis, electronics, spintronics, photonics, optoelectronics, sensors, biomedical technologies, energy generation and storage, as well as coating and composites [54].

Even though huge effort and vast resources have been invested into this field, the current global market size of graphene-related products is rather small. It is estimated to be worth only 1.5 million US dollars in 2015 but is expected to reach 310.4 million in 2020 and 2.1 billion by 2025 [55]. As the global industry chain has not fully taken shape, the research and development of graphene and related 2D systems is still at an early ramp-up phase, within which every step taken forward could be extremely critical.

Bibliography

[1] M. Riordan, L. Hoddeson, and C. Herring, Rev. Mod. Phys. **71**, S336 (1999).

[2] W. F. Brinkman, D. E. Haggan, and W. W. Troutman, IEEE J. Solid-St. Circ. **32**, 1858 (1997).

[3] G. E. Moore, IEEE J. Solid-St. Circ. Newsl. **20**, 33 (2006).

[4] G. E. Moore, IEEE J. Solid-St. Circ. Newsl. **20**, 36 (2006).

[5] I. Ferain, C. A. Colinge, and J.-P. Colinge, Nature **479**, 310 (2011).

[6] K. S. Novoselov, A. K. Geim, S. V. Morozov, D. Jiang, Y. Zhang, S. V. Dubonos, I. V. Grigorieva, and A. A. Firsov, Science **306**, 666 (2004).

[7] A. A. Balandin, S. Ghosh, W. Bao, I. Calizo, D. Teweldebrhan, F. Miao, and C. N. Lau, Nano Lett. **8**, 902 (2008).

[8] A. K. Geim and K. S. Novoselov, Nat. Mater. **6**, 183 (2007).

[9] C. Lee, X. Wei, J. W. Kysar, and J. Hone, Science **321**, 385 (2008).

[10] K. S. Novoselov, V. I. Fal'ko, L. Colombo, P. R. Gellert, M. G. Schwab, and K. Kim, Nature **490**, 192 (2012).

[11] R. Mas-Balleste, C. Gomez-Navarro, J. Gomez-Herrero, and F. Zamora, Nanoscale **3**, 20 (2011).

[12] A. C. Ferrari, F. Bonaccorso, V. Fal'ko, K. S. Novoselov, S. Roche, P. Bøggild, S. Borini, F. H. Koppens, V. Palermo, N. Pugno, *et al.*, Nanoscale **7**, 4598 (2015).

[13] S. Z. Butler, S. M. Hollen, L. Cao, Y. Cui, J. A. Gupta, H. R. Gutiérrez, T. F. Heinz, S. S. Hong, J. Huang, A. F. Ismach, *et al.*, ACS Nano **7**, 2898 (2013).

[14] A. Husen and K. S. Siddiqi, J. Nanobiotechnology **12**, 1 (2014).

[15] H. Oberhummer, H. Krauss, K. Grün, T. Rauscher, H. Abele, P. Mohr, and G. Staudt, Z. Phys. A **349**, 241 (1994).

[16] M. I. Katsnelson, Mater. Today **10**, 20 (2007).

[17] H. O. Pierson, *Handbook of carbon, graphite, diamonds and fullerenes: processing, properties and applications* (William Andrew, 2012).

[18] J. Walker, Rep. Prog. Phys. **42**, 1605 (1979).

[19] B. B. Pate, Surf. Sci. **165**, 83 (1986).

[20] J. Robertson and E. P. O'Reilly, Phys. Rev. B **35**, 2946 (1987).

[21] R. C. Haddon, R. E. Palmer, H. W. Kroto, and P. A. Sermon, Phil. Trans. R. Soc. Lond. A **343**, 53 (1993).

[22] H. W. Kroto, J. R. Heath, S. C. O'Brien, R. F. Curl, and R. E. Smalley, Nature **318**, 162 (1985).

[23] A. Šiber, Eur. Phys. J. B **53**, 395 (2006).

[24] D. M. Guldi and N. Martin, *Fullerenes: from synthesis to optoelectronic properties*, Vol. 4 (Springer Science & Business Media, 2013).

[25] T. D. Ladd, F. Jelezko, R. Laflamme, Y. Nakamura, C. Monroe, and J. L. O'Brien, Nature **464**, 45 (2010).

[26] S. Bosi, T. D. Ros, G. Spalluto, and M. Prato, Eur. J. Med. Chem. **38**, 913 (2003).

[27] S. Iijima, Nature **354**, 56 (1991).

[28] H. Nagai, Y. Okazaki, S. H. Chew, N. Misawa, Y. Yamashita, S. Akatsuka, T. Ishihara, K. Yamashita, Y. Yoshikawa, H. Yasui, L. Jianga, H. Ohara, T. Takahashi, G. Ichihara, K. Kostarelos, Y. Miyata, H. Shinohara, and S. Toyokuni, Proc. Natl. Acad. Sci. **108**, E1330 (2011).

[29] S. Niyogi, M. A. Hamon, H. Hu, B. Zhao, P. Bhowmik, R. Sen, M. E. Itkis, and R. C. Haddon, Acc. Chem. Res. **35**, 1105 (2002).

[30] X. Wang, Q. Li, J. Xie, Z. Jin, J. Wang, Y. Li, K. Jiang, and S. Fan, Nano Lett. **9**, 3137 (2009).

[31] M. F. L. De Volder, S. H. Tawfick, R. H. Baughman, and A. J. Hart, Science **339**, 535 (2013).

[32] R. R. Nair, P. Blake, A. N. Grigorenko, K. S. Novoselov, T. J. Booth, T. Stauber, N. M. R. Peres, and A. K. Geim, Science **320**, 1308 (2008).

[33] K. S. Novoselov, A. K. Geim, S. V. Morozov, D. Jiang, M. I. Katsnelson, I. V. Grigorieva, S. V. Dubonos, and A. A. Firsov, Nature **438**, 197 (2005).

[34] M. Koshino and T. Ando, Solid State Commun. **149**, 1123 (2009).

[35] T. Ohta, A. Bostwick, T. Seyller, K. Horn, and E. Rotenberg, Science **313**, 951 (2006).

[36] E. V. Castro, K. S. Novoselov, S. V. Morozov, N. M. R. Peres, J. M. B. Lopes dos Santos, J. Nilsson, F. Guinea, A. K. Geim, and A. H. Castro Neto, Phys. Rev. Lett. **99**, 216802 (2007).

[37] J. B. Oostinga, H. B. Heersche, X. Liu, A. F. Morpurgo, and L. M. K. Vandersypen, Nat. Mater. **7**, 151 (2008).

[38] J. M. B. Lopes dos Santos, N. M. R. Peres, and A. H. Castro Neto, Phys. Rev. Lett. **99**, 256802 (2007).

[39] P. Vogt, P. De Padova, C. Quaresima, J. Avila, E. Frantzeskakis, M. C. Asensio, A. Resta, B. Ealet, and G. Le Lay, Phys. Rev. Lett. **108**, 155501 (2012).

[40] M. E. Dávila, L. Xian, S. Cahangirov, A. Rubio, and G. Le Lay, New J. Phys. **16**, 095002 (2014).

[41] P. Tang, P. Chen, W. Cao, H. Huang, S. Cahangirov, L. Xian, Y. Xu, S.-C. Zhang, W. Duan, and A. Rubio, Phys. Rev. B **90**, 121408 (2014).

[42] H. Liu, A. T. Neal, Z. Zhu, Z. Luo, X. Xu, D. Tománek, and P. D. Ye, ACS Nano **8**, 4033 (2014).

[43] S. P. Koenig, R. A. Doganov, H. Schmidt, A. H. Castro Neto, and B. Özyilmaz, Appl. Phys. Lett. **104**, 103106 (2014).

[44] L. Li, Y. Yu, G. J. Ye, Q. Ge, X. Ou, H. Wu, D. Feng, X. H. Chen, and Y. Zhang, Nat. Nanotechnol. **9**, 372 (2014).

[45] D. Pacilé, J. C. Meyer, Ç. Ö. Girit, and A. Zettl, Appl. Phys. Lett. **92**, 133107 (2008).

[46] Q. H. Wang, K. Kalantar-Zadeh, A. Kis, J. N. Coleman, and M. S. Strano, Nat. Nanotechnol. **7**, 699 (2012).

[47] A. Pant, Z. Mutlu, D. Wickramaratne, H. Cai, R. K. Lake, C. Ozkan, and S. Tongay, Nanoscale **8**, 3870 (2016).

[48] G. S. Duesberg, Nat. Mater. **13**, 1075 (2014).

[49] L. Ci, L. Song, C. Jin, D. Jariwala, D. Wu, Y. Li, A. Srivastava, Z. F. Wang, K. Storr, L. Balicas, F. Liu, and P. M. Ajayan, Nat. Mater. **9**, 430 (2010).

[50] C. R. Dean, A. F. Young, I. Meric, C. Lee, L. Wang, S. Sorgenfrei, K. Watanabe, T. Taniguchi, P. Kim, K. L. Shepard, and J. Hone, Nat. Nanotechnol. **5**, 722 (2010).

[51] X. Duan, C. Wang, J. C. Shaw, R. Cheng, Y. Chen, H. Li, X. Wu, Y. Tang, Q. Zhang, A. Pan, J. Jiang, R. Yu, Y. Huang, and X. Duan, Nat. Nanotechnol. **9**, 1024 (2014).

[52] UK Intellectual Property Office Informatics Team, *Graphene: the worldwide patent landscape in 2015*, Tech. Rep. Intellectual property research: Patents (Intellectual Property Office, UK, 2015).

[53] P. Shapira, A. Gök, and F. S. Yazdi, *Graphene Research and Enterprise: Mapping Innovation and Business Growth in a Strategic Emerging Technology*, Tech. Rep. Nesta Working Paper No. 15/14 (Manchester Institute of Innovation Research and Manchester Business School, University of Manchester, UK, 2015).

[54] Work Package Dissemination, *Graphene Flagship Annual Report 2015*, Tech. Rep. (Graphene Flagship, 2015).

[55] A. McWilliams, *Graphene: Technologies, Applications and Markets*, Tech. Rep. AVM075D (BCC Research, 2016).

2

Graphene and Its Bilayer: Theoretical Background

This chapter aims to establish a basic theoretical framework which is essential in order to interpret the results present in Chapter 4, 5 and 6 of this thesis. It starts with the crystal structures of graphene and bilayer graphene in real and reciprocal space, followed by the introduction of their band structures calculated using the tight binding approach in the simplest manner. Transport phenomena in these two systems arising from the application of magnetic fields are introduced in the second part of this chapter.

Contents

2.1 Lattice in real and reciprocal space

2.1.1 Graphene

Graphene, as introduced in Chapter 1, has a honeycomb crystal structure, as shown in Figure 2.1a. The hexagonal lattice can be decomposed into conventional unit cells (shaded rhombus) with primitive lattice vectors,

$$\vec{a}_1 = (\frac{\sqrt{3}a_0}{2}, \frac{a_0}{2}) = \frac{a}{2}(3, \sqrt{3}), \quad \vec{a}_2 = (\frac{\sqrt{3}a_0}{2}, -\frac{a_0}{2}) = \frac{a}{2}(3, -\sqrt{3}), \tag{2.1}$$

where $a_0 = |\vec{a}_1| = |\vec{a}_2|$ is the lattice constant and $a = a_0/\sqrt{3} \approx 1.42$ Å is the nearest-neighbour distance between the sublattice sites A and B. The nearest-neighbour vectors

from one A site to the three surrounding B sites are,

$$\vec{n}_1 = \frac{a}{2}(-1, \sqrt{3}), \quad \vec{n}_2 = \frac{a}{2}(-1, -\sqrt{3}), \quad \vec{n}_3 = \frac{a}{2}(2, 0). \tag{2.2}$$

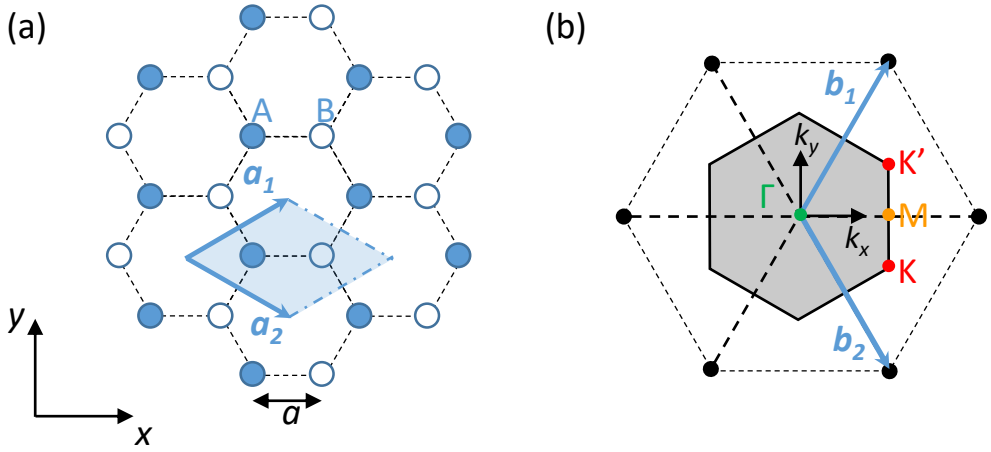

Figure 2.1: (a) The honeycomb lattice of graphene in real space. A conventional unit cell is shaded with lattice vectors $\vec{a}_1$ and $\vec{a}_2$ shown. The A and B sublattice sites are also labelled. (b) The reciprocal lattice of graphene with the first Brillouin zone shaded. High symmetry points are highlighted with different colours.

The reciprocal lattice of graphene, defined by $e^{i\vec{k}\cdot\vec{r}} = 1$, where $\vec{k}$ is a reciprocal-space lattice vector and $\vec{r}$ is a real-space lattice vector, also has a hexagonal structure with the lattice vectors,

$$\vec{b}_1 = \frac{2\pi}{3a}(1, \sqrt{3}), \quad \vec{b}_2 = \frac{2\pi}{3a}(1, -\sqrt{3}). \tag{2.3}$$

The shaded area in Figure 2.1b represents the first Brillouin zone. Four high symmetry points are also labelled, with Γ and M indicating the centre and the middle point of an edge, respectively, and K, K' showing the two non-equivalent corners. As will be shown later in this chapter, the dispersion relation in the vicinity of K and K' points, with wave vectors,

$$\vec{K} = \frac{2\pi}{3a}(1, \frac{\sqrt{3}}{3}), \quad \vec{K}' = \frac{2\pi}{3a}(1, -\frac{\sqrt{3}}{3}), \tag{2.4}$$

possesses the most unique features which are responsible for many special electronic

properties of graphene.

2.1.2 Graphene bilayer

Bilayer graphene is formed by stacking two layers of graphene. It can exist in three types of structures: AA-stacked, AB-stacked, and twisted bilayer, depending on the orientations of the two consisting layers (Figure 2.2). The AA-stacked bilayer is the simplest form in which the sublattice sites A1 and B1 originated from the first layer is directly below the A2 and B2 sites of the second layer, respectively. In the AB-stacked bilayer, all the A sites of the first layer are directly below the B sites of the second layer (hence AB-stacking), while the other half of the carbon atoms are located below or above the centres of the hexagons. This structure can be viewed as a modification of the AA-stacked structure by rotating the second layer by a 60° angle relative to the first layer. AB-stacking is also known as Bernal stacking. The third type of bilayer structure is the twisted bilayer, where a relatively small rotation angle exists between the two layers, creating a superimposed pattern (superlattice) known as the Moiré pattern [1, 2].

Among all these three types, AB-stacked bilayer graphene is the most stable form, hence the most commonly seen stacking type in natural graphite and synthesised bilayer graphene [2, 3]. In the following content of this thesis, bilayer graphene will simply refer to the AB-stacked bilayer unless otherwise stated. Bilayer graphene has a interlayer spacing of approximately 3.4 Å [3, 4]. As shown in Figure 2.2b, identical to single layer graphene, it has primitive lattice vectors given by Equation 2.1 in real space and has a reciprocal lattice structure shown in Figure 2.1 with lattice vectors given by Equation 2.3. However, different from single layer graphene, each unit cell in bilayer graphene contains four atoms, A1, B1, A2, and B2.

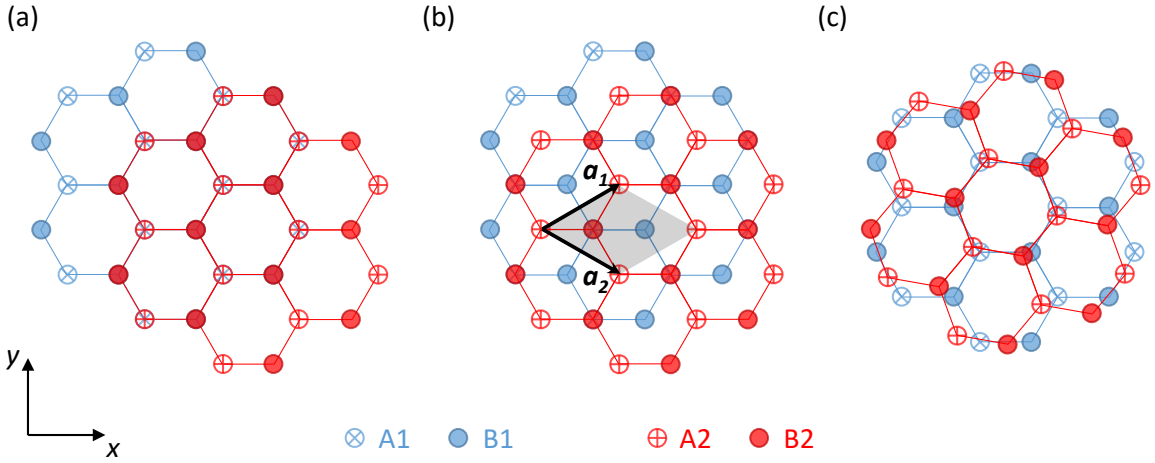

Figure 2.2: Top view of (a) AA-stacked, (b) AB-stacked and (c) twisted bilayer graphene. The first (bottom) layer and its sublattice sites A1 and B1 are marked in blue. The second (top) layer and its sublattice sites A2 and B2 are marked in red.

2.2 Tight binding approach

The band structure of monolayer graphene was first calculated by Philip Wallace in 1947 [5] using the tight binding approximation in order to determine the band structure of graphite. In its simplest form, considering only the π states from the nearest neighbours of the sub-lattices A and B, with a hopping parameter γ_0, the tight binding Hamiltonian is given by,

$$\hat{H}_m(\vec{k}) = \begin{pmatrix} 0 & \gamma_0 S_m(\vec{k}) \\ \gamma_0 S_m^*(\vec{k}) & 0 \end{pmatrix}, \tag{2.5}$$

where $\vec{k} = (k_x, k_y)$ is the wave vector and

$$S_m(\vec{k}) = \sum_{\vec{n}} e^{i\vec{k}\cdot\vec{n}} = 2\exp\left(\frac{-ik_x a}{2}\right)\cos\left(\frac{\sqrt{3}}{2}k_y a\right) + \exp\left(ik_x a\right). \tag{2.6}$$

We therefore have the energy,

$$E_m(\vec{k}) = \pm\gamma_0|S_m(\vec{k})| = \pm\gamma_0\sqrt{3 + f(\vec{k})}, \tag{2.7}$$

where

$$f(\vec{k}) = 2\cos\left(\sqrt{3}k_y a\right) + 4\cos\left(\frac{\sqrt{3}}{2}k_y a\right)\cos\left(\frac{3}{2}k_x a\right). \tag{2.8}$$

The value of γ_0 can be derived from first principles calculations [6, 7] and has been experimentally determined to be 3.38 eV [8].

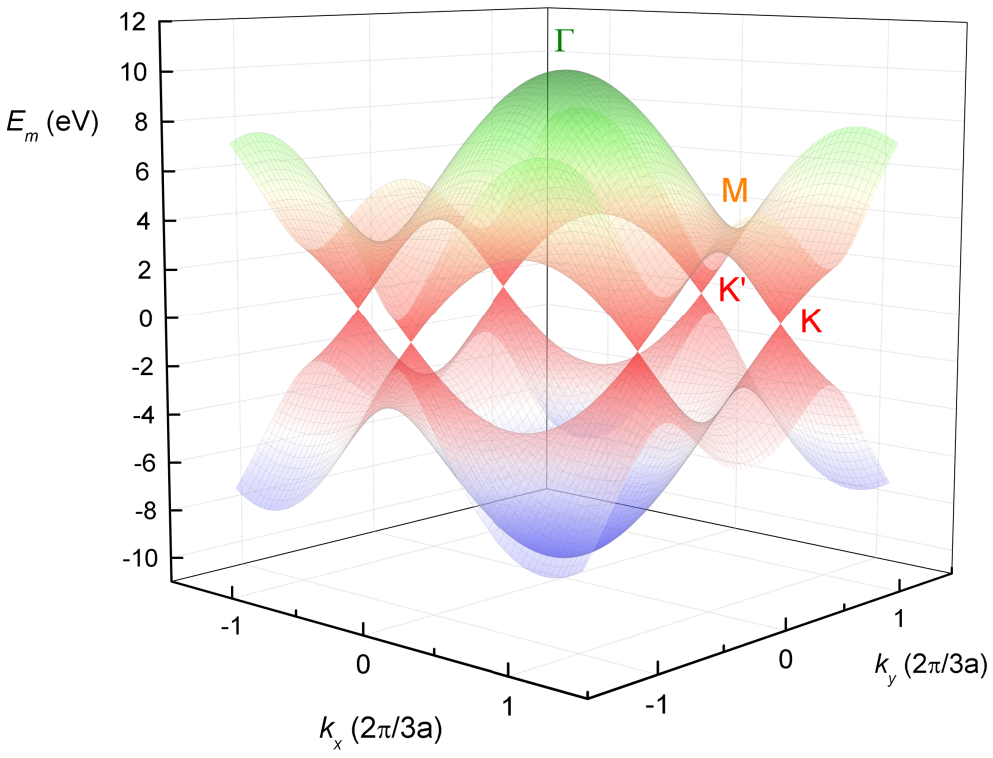

Figure 2.3: Band structure of graphene calculated by the nearest-neighbour tight binding approximation. Valleys of the conduction band touch the valence band at K and K' points. High symmetry points are colour-matched with those in Figure 2.1b.

Figure 2.3 shows the band structure of single layer graphene using Equation 2.7 and 2.8. One can immediately see that the conduction band touches the valence band at six corners (K and K' points) of the first Brillouin zone. It is also observed that the band structure calculated this way is symmetrical relative to zero energy. This is because that in the above calculation, only the nearest-hopping is accounted for. The electron-hole

symmetry will be broken if hopping processes between atoms more distant than nearest neighbours, or the overlap integrals are taken into account. For example, by including the next-nearest-neighbour hopping γ_0', Equation 2.7 will be modified into,

$$E_m(\vec{k}) = \pm\gamma_0|S_m(\vec{k})| + \gamma_0' f(\vec{k}) = \pm\gamma_0\sqrt{3 + f(\vec{k})} + \gamma_0' f(\vec{k}). \tag{2.9}$$

This will effectively shift the conical plane from $E_m = 0$ to $E_m = -3\gamma_0'$ with the conduction band being stretched and the valence band being compressed in energy. However, the dispersion at the bottom of the valleys, with respect to K and K' points, will be preserved.

In bilayer graphene, additional hopping processes between the sublattice sites of each layer should be considered in order to calculate its band structure, as shown in Figure 2.4.

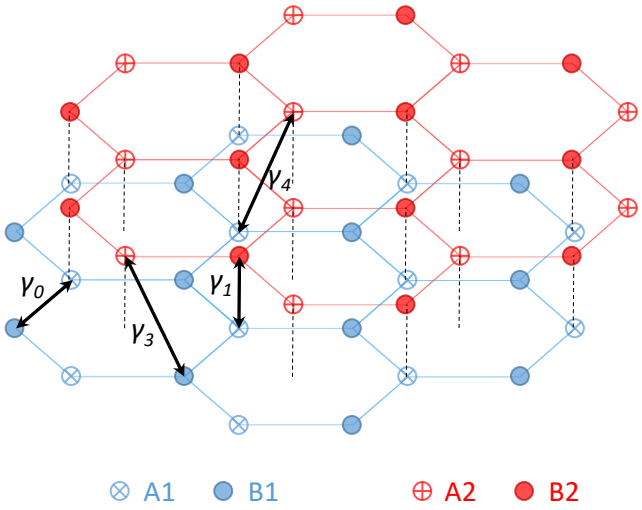

Figure 2.4: Hopping parameters in AB-stacked bilayer graphene.

Among these processes, γ_0 and γ_1 are the most dominant. $\gamma_0 \approx 3.38$ eV, the same as in single layer graphene while $\gamma_1 \approx 0.4$ eV [9], almost an order of magnitude smaller than γ_0. In the simplest form, only including γ_0 and γ_1, the Hamiltonian can be expressed

as,

$$\hat{H}_b(\vec{k}) = \begin{pmatrix} 0 & \gamma_0 S_b(\vec{k}) & 0 & \gamma_1 \\ \gamma_0 S_b^*(\vec{k}) & 0 & 0 & 0 \\ 0 & 0 & 0 & \gamma_0 S_b^*(\vec{k}) \\ \gamma_1 & 0 & \gamma_0 S_b(\vec{k}) & 0 \end{pmatrix}, \tag{2.10}$$

where $S_b(\vec{k}) = S_m(\vec{k})$ as given by Equation 2.6. The eigenvalues are therefore,

$$E_b(\vec{k}) = \pm\frac{1}{2}\gamma_1 \pm \sqrt{\frac{1}{4}\gamma_1^2 + \gamma_0^2\left(3 + f(\vec{k})\right)}, \tag{2.11}$$

where the two $\pm$ signs are independent and $f(\vec{k})$ is given by Equation 2.8. As shown in Figure 2.5, similar to monolayer graphene, bilayer graphene is also a gapless semiconductor with one pair of bands intersect at K and K' points where $E = 0$. However, in bilayer graphene, another pair of bands exist and are separated by a relatively large gap $2\gamma_1 \approx 0.8$ eV. Without further modification to the above calculation, these two pairs of bands are also symmetric about the $E = 0$ plane.

2.3 Low-energy electronic structure

In both monolayer and bilayer graphene, intrinsically, the Fermi level lies exactly at the plane consisting of K and K' points, since the number of carbon atoms in one unit cell of bilayer graphene is also doubled in addition to the doubling of the number of bands compared to monolayer graphene. Therefore, the low-energy physics in both systems is solely related to the Hamiltonian and dispersion relation of the two touching bands around K and K' points. As will be shown in this section, both systems exhibit unique low-energy electronic structures distinguishable from any other known materials and also between themselves, providing the most important fundamental support to their transport properties and potential applications.

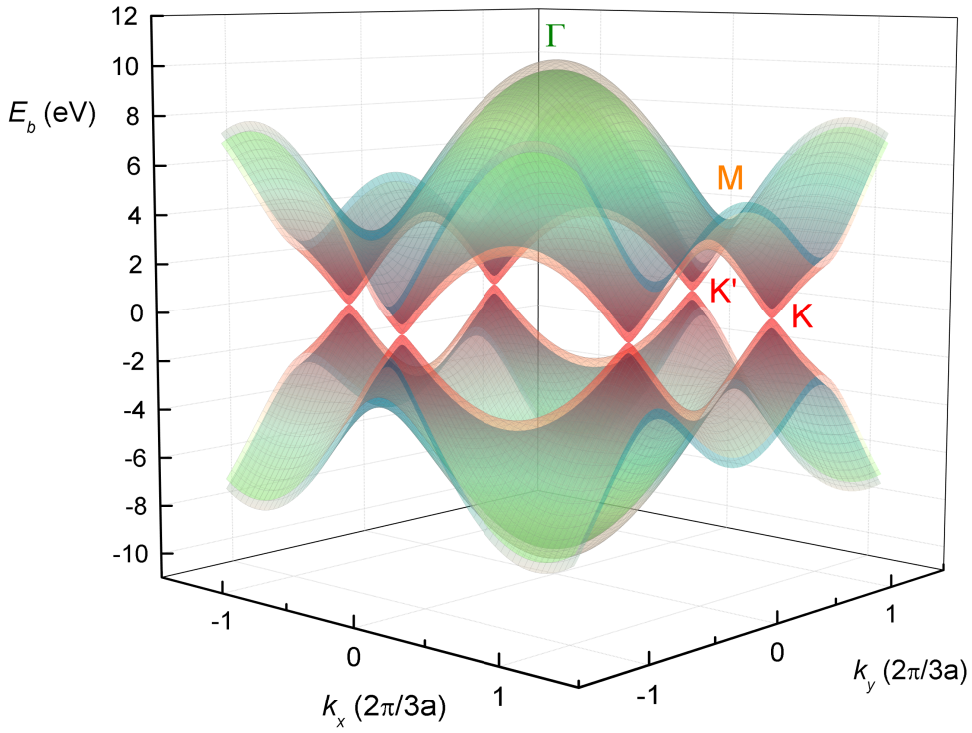

Figure 2.5: Band structure of AB-stacked bilayer graphene using Equation 2.11 with $\gamma_0 = 3.38$ eV and $\gamma_1 = 0.4$ eV.

2.3.1 Massless Dirac fermions in graphene

In the vicinity of the K (or K') points, the wave vector can be replaced by, $\vec{k} = \vec{K}$ (or $\vec{K'}$) $+ \vec{q}$, where $|\vec{q}| \ll |\vec{K}|$ (or $|\vec{K'}|$). The Hamiltonian given by Equation 2.5 for monolayer graphene can be therefore transformed into,

$$\hat{H}_m^K(\vec{k}) = \hbar v_F \begin{pmatrix} 0 & q_x - iq_y \\ q_x + iq_y & 0 \end{pmatrix}, \tag{2.12}$$

where

$$v_F = \frac{3\gamma_0 a}{2\hbar}. \tag{2.13}$$

As a result, the eigenvalues are,

$$E_m(\vec{q}) = \pm\hbar v_F|\vec{q}|. \tag{2.14}$$

These results show that the low-energy dispersion relation around the K and K' points are linear (Figure 2.6), similar to Einstein's relativistic dispersion with zero rest mass. The above Hamiltonian, clearly different from a conventional non-relativistic Hamiltonian described by the Schrödinger equation, mimics the form of a 2D Dirac Hamiltonian for massless fermions, with an effective speed of light $v_F \approx 1.1 \times 10^6$ m/s [10, 11]. Consequently, the quasiparticles in graphene are called massless Dirac fermions; the K and K' points are called Dirac points; and the valleys around these Dirac points are called Dirac cones. The density of states (DOS) in close proximity to the Dirac points can be easily calculated as,

$$G_m(E) = g_s g_v \frac{E}{2\pi\hbar^2 v_F^2}, \tag{2.15}$$

where $g_s = g_v = 2$ representing spin ($\uparrow$ and $\downarrow$) and valley (K and K') degeneracies. This indicates that, in an ideal and intrinsic graphene sample, no states exist at the Fermi level. In reality, however, it is not true due to the effects of disorder present in the system, as will be discussed later in Chapter 4.

2.3.2 Massive Dirac fermions in AB-stacked graphene bilayer

Similarly, in AB-stacked bilayer graphene, by expanding the Hamiltonian given by Equation 2.10 near the K and K' points and neglecting the high-energy bands that are relatively far away, an effective Hamiltonian can be reconstructed as [9, 11, 12],

$$\hat{H}_b^K(\vec{k}) = -\frac{\hbar}{2m^*}\begin{pmatrix} 0 & (q_x - iq_y)^2 \\ (q_x + iq_y)^2 & 0 \end{pmatrix}, \tag{2.16}$$

where

$$m^* = \frac{\gamma_1}{2v_F^2}. \tag{2.17}$$

The eigenvalues are,

$$E_b(\vec{q}) = \pm\frac{\hbar^2|\vec{q}|^2}{2m^*}. \tag{2.18}$$

The quasiparticles described by the above Hamiltonian are so unique that no analogies to the existing quantum theory can be found. This new type of Hamiltonian differs from both the non-relativistic and the relativistic cases, as it contains both the off-diagonal structure which is Dirac-like and the Schrödinger-like first term with an effective mass m^* [11]. As a result, quasiparticles in bilayer graphene are usually referred to as massive Dirac fermions. Compared with the linear low-energy dispersion relation of monolayer graphene, bilayer graphene exhibits a parabolic behaviour as given by Equation 2.18, similar to conventional semiconductors. The density of states in the vicinity of the K and K' points is therefore a constant,

$$G_b(E) = g_s g_v \frac{m^*}{2\pi\hbar^2}, \tag{2.19}$$

where $g_s = g_v = 2$.

Figure 2.6 shows the low-energy band structure (Equations 2.14, 2.18) and the corresponding density of states (Equations 2.15, 2.19) in both graphene and its bilayer for comparison.

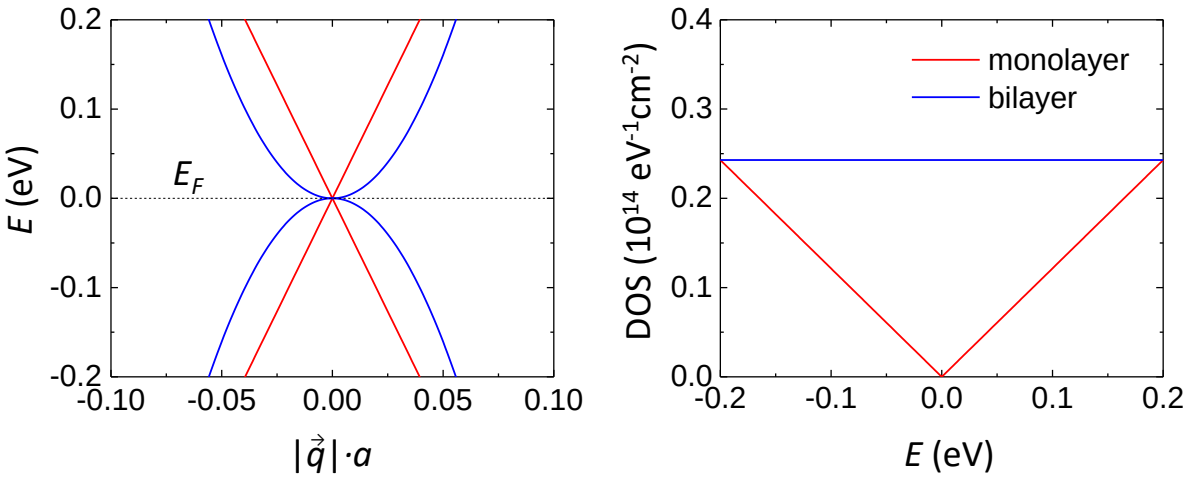

Figure 2.6: Low-energy dispersion and density of states of monolayer (red) and bilayer (blue) graphene calculated using Equations 2.14, 2.15, 2.18 and 2.19 with $\gamma_0 = 3.38$ eV and $\gamma_1 = 0.4$ eV.

2.4 Transport in low magnetic fields

2.4.1 Classical Hall effect

Discovered by Edwin Hall in 1879 [13], the classical Hall effect describes a voltage difference across a conductor perpendicular to the direction of an electric current and a low magnetic field applied perpendicular to the current.

For a 2D specimen, a typical set-up measuring the Hall effect using a so-called Hall bar geometry is shown in Figure 2.7; the applied magnetic field $\vec{B} = (0, 0, B_z)$ is in the z direction, and the applied current is in the x direction. The resulting electric field $\vec{E} = (E_x, E_y, 0)$ is within the x-y plane because of the nature of a 2D material and the Lorentz force. Assuming the 2D specimen is isotropic and contains a single type of charge carriers with the effective mass m^* and the charge q, we can write,

$$m^* \left(\frac{\mathrm{d}\vec{v}}{\mathrm{d}t} + \frac{\vec{v}}{\tau} \right) = q\vec{E} + q\vec{v} \times \vec{B}, \tag{2.20}$$

where τ is the relaxation time. Splitting this into x and y components gives

$$m^* \left(\frac{\mathrm{d}v_x}{\mathrm{d}t} + \frac{v_x}{\tau} \right) = qE_x + qv_y B_z, \tag{2.21}$$

and

$$m^* \left(\frac{\mathrm{d}v_y}{\mathrm{d}t} + \frac{v_y}{\tau} \right) = qE_y - qv_x B_z. \tag{2.22}$$

In a steady state, $\frac{\mathrm{d}\vec{v}}{\mathrm{d}t} = (0,0,0)$ and the 2D current density $\vec{j} = nq\vec{v} = (j_x, 0, 0)$, the Hall voltage ($V_H$) and the Hall coefficient (R_H) are therefore

$$V_H \equiv V_y = \frac{I_x B_z}{nq}, \tag{2.23}$$

and

$$R_H \equiv \frac{E_y}{j_x B} = \frac{1}{nq}, \tag{2.24}$$

where n is the 2D carrier density and $q = -e$ (or $+e$) for electrons (or holes).

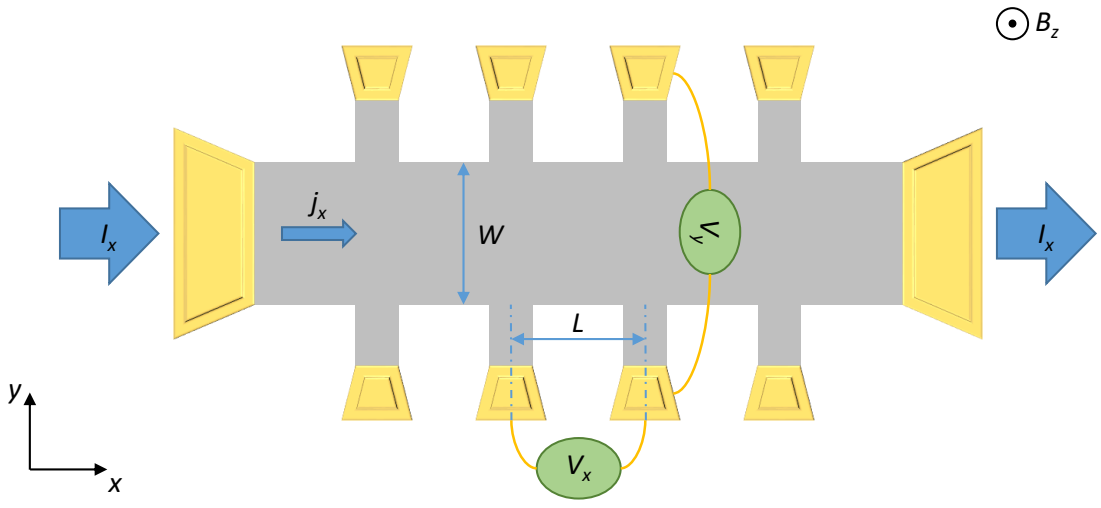

Figure 2.7: Geometry of a 10-leg Hall bar with the current and the magnetic field directions indicated. Voltage measurements are made both parallel and perpendicular to the current direction. The gold areas represent the metal contacts. Dimensions of the effective area are also labelled.

The conductivity σ and resistivity ρ of a 2D isotropic material in magnetic fields can be represented in tensor forms, an analogy to those of an anisotropic material at zero-field, i.e., $\vec{j} = \hat{\sigma}\vec{E}$ and $\vec{E} = \hat{\rho}\vec{j}$, where

$$\hat{\sigma} = \begin{pmatrix} \sigma_{xx} & -\sigma_{xy} \\ \sigma_{xy} & \sigma_{xx} \end{pmatrix}, \quad \hat{\rho} = \begin{pmatrix} \rho_{xx} & -\rho_{xy} \\ \rho_{xy} & \rho_{xx} \end{pmatrix}, \tag{2.25}$$

and

$$\sigma_{xx} = \frac{\rho_{xx}}{\rho_{xx}^2 + \rho_{xy}^2}, \quad \sigma_{xy} = \frac{\rho_{xy}}{\rho_{xx}^2 + \rho_{xy}^2}. \tag{2.26}$$

The Hall resistivity is given by

$$\rho_{xy} \equiv \frac{E_y}{j_x} = \frac{V_y}{I_x} = \frac{B_z}{nq}, \tag{2.27}$$

and the longitudinal resistivity is given by

$$\rho_{xx} \equiv \frac{E_x}{j_x} = \frac{W}{L}\frac{V_x}{I_x} = \frac{1}{nq\mu}, \tag{2.28}$$

where W is the width of the Hall bar and L is the length of segment of the Hall bar, across which V_y and V_x are measured, respectively, as shown in Figure 2.7. $\mu = q\tau/m^*$ is the mobility of the charge carriers.

It is often the case that there are more than one type of charge carriers. Similarly, the multi-carrier Hall effect can be analysed by solving a set of Equations 2.20 for each carrier type with its individual m_i^*, τ_i, q_i and $\vec{v}_i$, using equilibrium conditions $\frac{\mathrm{d}\vec{v}_i}{\mathrm{d}t} = (0, 0, 0)$ and $\sum \vec{j}_i = (j_x, 0, 0)$.

Measurements of the classical Hall effect are extremely powerful to determine the characteristics of charge carriers present in the system including their charges, densities, and mobilities. The fact that such measurements require only a small magnetic field (often below 0.5 T) makes them even more popular. From another point of view, using

known materials, sensors can be made for detecting and measuring magnetic fields.

2.4.2 Weak localisation

Another transport phenomenon at low magnetic fields is the weak localisation (WL) effect. In a disordered system, the motion of charge carriers is diffusive rather than ballistic due to random scattering events. Such diffusive motion is essentially a random walk, which can maintain phase coherence below a maximum length controlled by the dephasing rate, τ_ϕ^{-1}, due to inelastic scattering [14]. The conductivity of the system can be viewed to be proportional to the probability that a charge carrier can propagate through the material.

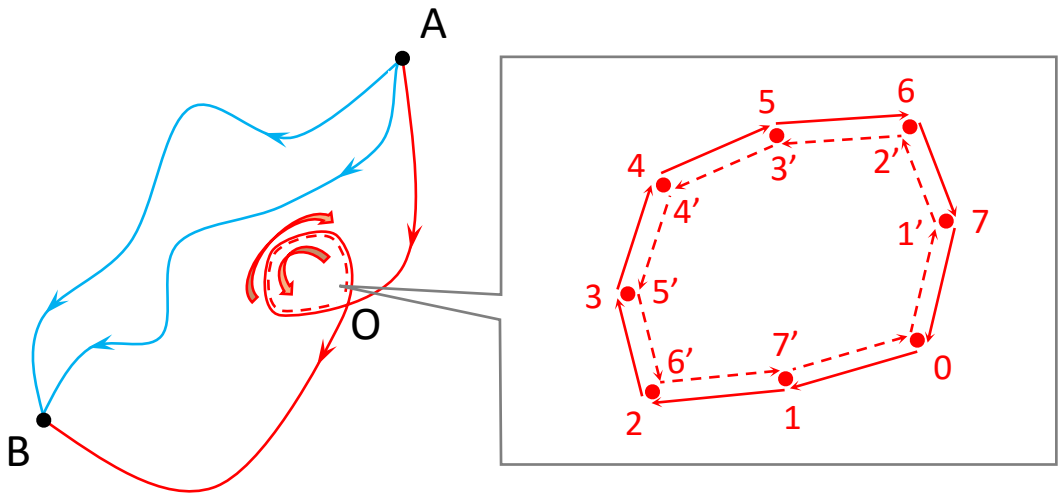

Figure 2.8: Illustration of normal (blue) and self-intersecting (red) scattering paths. In a self-intersecting scattering path, the constructive interference of the two partial waves travelling in opposite directions gives rise to the weak localisation effect.

In quantum mechanics, the total probability is the mod-square of the sum of probability amplitudes of all the connecting trajectories, rather than the sum of probabilities in classical physics. As shown in Figure 2.8, the probability for an electron to get from

A to B is

$$P_{AB} = |\sum_i A_i|^2 = \sum_i |A_i|^2 + \Re e\left(\sum_{i,j} A_i A_j^*\right), \tag{2.29}$$

where $A_{i(j)}$ is the probability amplitude of each trajectory. The latter term represents the effect of quantum interference. For ordinary trajectories such as those shown in blue, the phase picked up by travelling through the material is randomised. The interference term is therefore vanished due to disorder averaging. However, for self-intersecting trajectories in which an electron can be scattered back to the origin O forming a closed loop, partial waves can propagate along the time-reversed loop in opposite directions (i.e. clockwise following 0-1-...-7-0 and anticlockwise following 0-1'-...-7'-0) with equal probability amplitudes $A_{CW} = A_{CCW}$ [15]. Therefore, they will always be in phase and interfere constructively surviving disorder averaging. As a result, the probability for such loops is increased to twice as large as the classical contributions. This means charge carriers will have a higher tendency to localise in these loops and the net conductivity will therefore be slightly suppressed. The corresponding correction to the transport properties is known as the weak localisation correction. In low-dimensional systems, the weak localisation effect is more pronounced, as there is a higher chance to find self-intersecting trajectories compared with 3D systems.

The magnitude of weak localisation is a function of temperature. Increasing the temperature has the effect of increasing the de-phasing rate τ_ϕ^{-1} [16], such that the total number of phase coherent loops is decreased, hence weakens the weak localisation effect. In a magnetic field, an extra phase difference $\frac{2e\hbar}{\Phi}$ is added to the two partial waves around a loop containing the magnetic flux Φ [15]. By averaging over different loops of various sizes, the interference term can be dismissed, and weak localisation is again destroyed. Therefore, at a given temperature, the magnitude of weak localisation can be determined by the difference between the resistivity at zero and a small magnetic field. As will be shown in Chapter 6, this method can be used to characterise the energy

loss rate of hot electrons in monolayer and bilayer graphene.

2.5 Transport in high magnetic fields

2.5.1 Landau level spectrum

Semi-classically, in a static and uniform magnetic field, due to the Lorentz force, the motion of charge carriers in a solid is a circular motion in closed orbits perpendicular to the magnetic field with constant energy. This motion is known as the cyclotron motion. The corresponding angular frequency ω_c (cyclotron frequency) is

$$\omega_c = \frac{qB}{m_c}, \tag{2.30}$$

where

$$m_c = \frac{\hbar^2}{2\pi}\frac{\partial A_k}{\partial E}, \tag{2.31}$$

is the cyclotron mass and A_k is the area in k-space of the closed orbit. It is easy to see that for a free-electron system $m_c = m_e$, and for an isotropic semiconductor with a parabolic dispersion $m_c = m^*$ where $m^* = \hbar^2 \left(\frac{\mathrm{d}^2 E}{\mathrm{d}k^2}\right)^{-1}$ is the effective mass.

Quantum mechanically, considering a conventional 2D system in the x-y plane with a simple parabolic dispersion, the Hamiltonian in the absence of a magnetic field is given by

$$\hat{H} = \frac{\hat{p}^2}{2m^*}. \tag{2.32}$$

In a magnetic field parallel to the z axis $\vec{B} = (0, 0, B_z)$, the momentum operator $\hat{p}$ is replaced by $\hat{p} + e\hat{A}$, where $\hat{A}$ is a vector potential generating $\vec{B}$ via $\vec{B} = \nabla \times \hat{A}$. To give the correct $\vec{B}$, one particular choice for $\hat{A}$ is the Landau gauge, $\hat{A} = (0, B_z x, 0)$. The

eigenvalues can therefore be easily obtained as

$$E_N = (N + \frac{1}{2})\frac{\hbar eB}{m^*} = (N + \frac{1}{2})\hbar\omega_c, \tag{2.33}$$

where $N = 0, 1, 2, 3....$ Therefore, the energy of the cyclotron motion is quantised. These quantised energy levels are known as Landau levels and N is the Landau level index. For non-relativistic fermions whose Hamiltonian follows Equation 2.32 (such as in GaAs/AlGaAs heterostructures, Figure 2.9 [blue]), the Landau levels are equally spaced with a spacing of $\hbar$ times the semiclassical cyclotron frequency ω_c, which is linearly dependent on B.

In monolayer graphene, however, charge carriers are massless Dirac fermions whose Hamiltonian is given by 2.12, which dramatically changes the Landau quantisation (Figure 2.9 [red]). The Landau level spectrum in monolayer graphene is given by

$$E_N = v_F\sqrt{2\hbar eBN} = \sqrt{N}\hbar\omega_c', \quad (N = 0, 1, 2, 3...) \tag{2.34}$$

where

$$\omega_c' = v_F\sqrt{\frac{2eB}{\hbar}}, \tag{2.35}$$

is defined as the cyclotron frequency for massless Dirac fermions [17, 18]. Several important features of these Landau levels, in contrast to the conventional case, can already be seen. First of all, the energy of each level no longer increases linearly with B. Instead, a $B^{\frac{1}{2}}$ dependence is observed. Secondly, these Landau levels are un-evenly distributed, with the energy difference between the Nth and the $(N+1)$th levels scaling with $\sqrt{N+1} - \sqrt{N}$. Therefore, the largest energy separation exists between the 0th level and the 1st level. Last but not least, the 0th Landau level always has zero energy independent of magnetic fields, with its states shared equally by electrons and holes. All of these features are consequences of the unique nature of massless Dirac fermions

in monolayer graphene [18].

In bilayer graphene (Figure 2.9 [green]), the situation is different from both of the previous cases. For massive Dirac fermions described by the Hamiltonian in Equation 2.16, the Landau level spectrum is

$$E_N = \sqrt{N(N-1)}\hbar\omega_c'', \quad (N = 0, 1, 2, 3...) \tag{2.36}$$

where

$$\omega_c'' = \frac{eB}{m^*}, \tag{2.37}$$

is the cyclotron frequency for bilayer graphene with the effective mass m^* given by Equation 2.17. Similar to its Hamiltonian, which has both Schödinger-like and Dirac-like features as discussed in Section 2.3.2, the Landau level spectrum in bilayer graphene again shows mixed characteristics. The energy of each level scales up linearly with magnetic field, like that of conventional semiconductors but with a much smaller effective mass [19]. At the same time, the Landau level separations are not equal, like those of monolayer graphene but with a different scaling factor $\sqrt{(N+1)N} - \sqrt{N(N-1)}$. In bilayer graphene, both the 0th and the 1st Landau levels have zero energy, another unique feature for massive Dirac fermions.

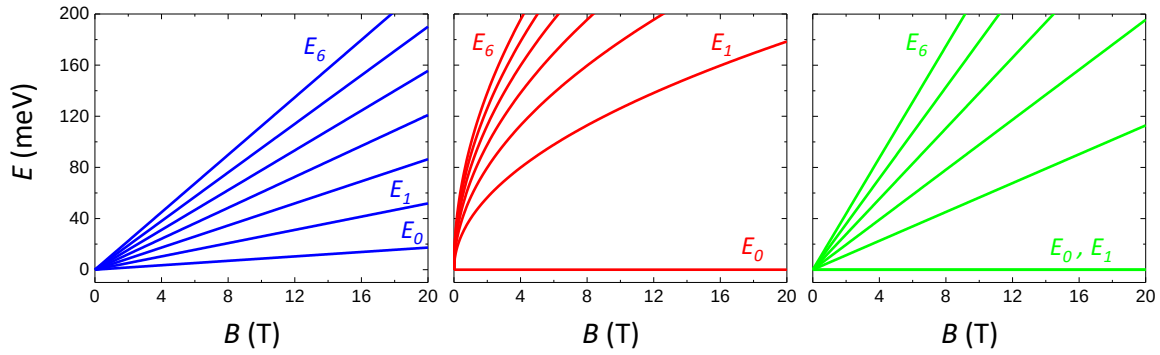

Figure 2.9: Landau level spectra of GaAs/AlGaAs (blue), monolayer graphene (red) and bilayer graphene (green). Only the first seven levels (from E_0 to E_6) are shown.

In all cases, the maximum number of available states N_{LL} in one Landau level can be determined by counting the total number of possible centres of the cyclotron orbits under the condition that the centres should be within the sample. This gives

$$N_{LL} = \frac{eBA}{h} = \frac{\Phi}{\Phi_0}, \tag{2.38}$$

where Φ is the total magnetic flux through the sample and $\Phi_0 = h/e$ is the magnetic flux quantum. Thus, combining spin and valley degeneracies, each Landau level will contain an equal number of states per unit area, $g_s g_v \frac{eB}{h} = g_s g_v B/\Phi_0$. In sufficiently high magnetic fields, both the spin and valley degeneracies can be lifted [20]. As a result, the Landau levels will split into two or four sub-levels.

Often, a dimensionless quantity known as the filling factor, ν, is used to describe the occupancy of Landau levels by electrons or holes, defined as

$$\nu = n_{e(h)} / \left(\frac{eB}{h}\right), \tag{2.39}$$

where $n_{e(h)}$ is the electron (hole) density. For example, we can calculate the filling factor that corresponds to fully occupied Landau levels up to the Nth by electrons, assuming the spin and valley degeneracies have not been lifted:

(1) In GaAs/AlGaAs, whose Landau level spectrum is given by the conventional case (i.e. Equation 2.33), $\nu = 2(N + 1)$. The factor 2 comes from the spin degeneracy, and there is no valley degeneracy in this system.

(2) In monolayer graphene, $\nu = 4(N + \frac{1}{2})$. The factor 4 corresponds to $g_s = g_v = 2$. The $\frac{1}{2}$ represents only half of the states in the $N = 0$ Landau level are electron-like, since $E_0 = 0$.

(3) In bilayer graphene, $\nu = 4N$, since $g_s = g_v = 2$. Please note that in this expression, "fully occupied" requires that N starts from 1 rather than 0, since both

the 0th and the 1st Landau levels in bilayer graphene have zero energy and therefore degenerate. Each of these two levels also contains an equal amount of electron-like and hole-like states.

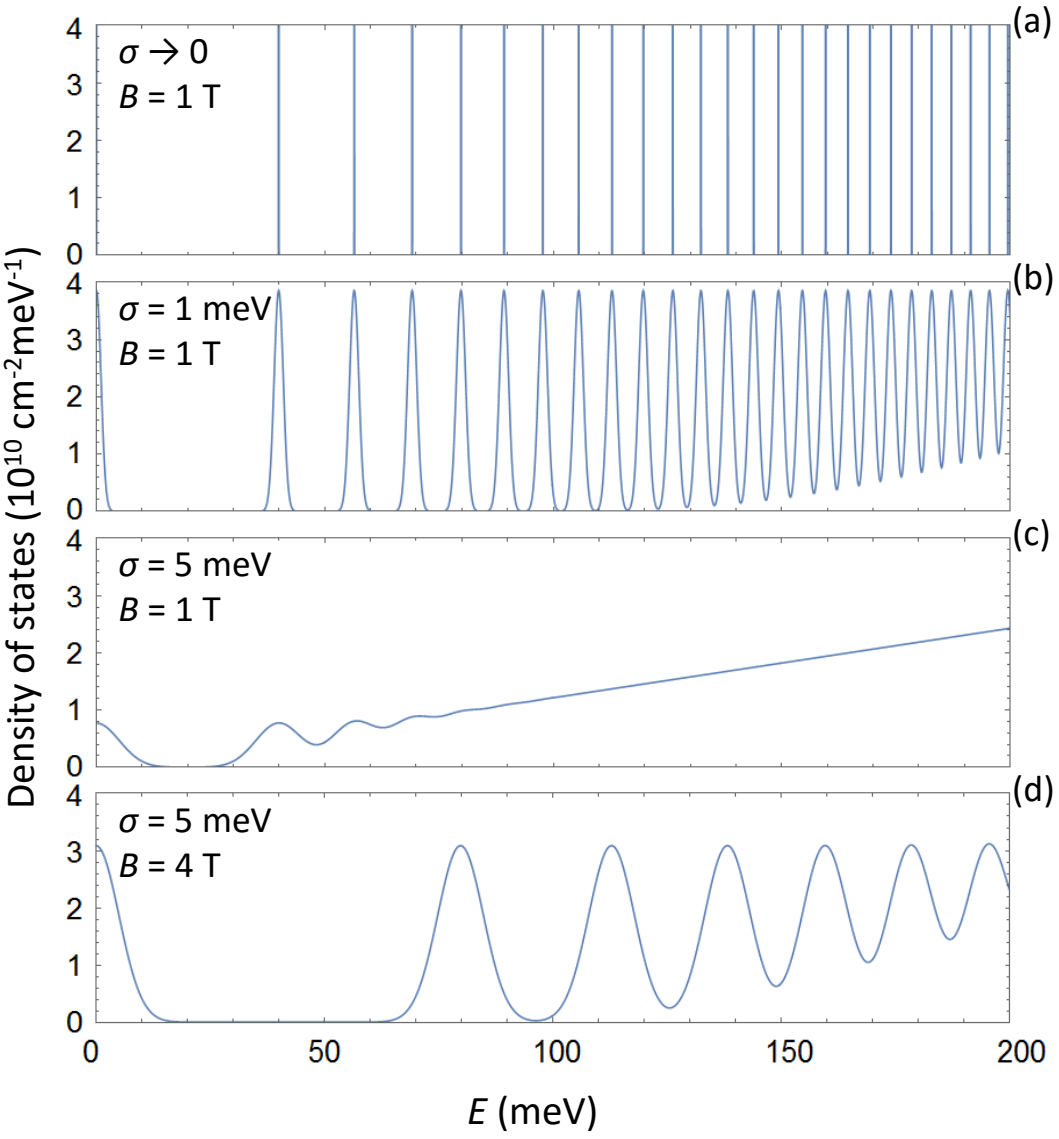

Figure 2.10: The effects of Landau level broadening and magnetic fields on the density of states in monolayer graphene. σ is the Gaussian width of the broadening.

In an ideal sample, the Landau levels are perfectly sharp whose densities of states are a series of δ-functions. In a real sample, however, the Landau levels are broadened due to scatterings of charge carriers by defects and impurities in the system or interfaces.

Assuming a typical scattering time τ, according to the uncertainty principle, the levels will be broadened by $\delta E \sim \frac{\hbar}{2\tau}$. Therefore, the effects of magnetic fields will only become obvious when the Landau level separation exceeds the broadening. Figure 2.10 simulates the densities of states of a series of Landau levels in graphene assuming the broadening is Gaussian-like with a standard deviation σ. At 1 T without broadening (Figure 2.10a), $\sigma \to 0$, and a series of δ-functions are observed. When a small broadening $\sigma = 1$ meV is introduced (Figure 2.10b), the majority of the Landau levels are still well separated. When a large broadening is present in the system, such as in Figure 2.10c where σ has been increased to 5 meV, individual Landau levels are hardly seen except the first few. The density of states mainly shows a linear increase with E, restored to the case at zero magnetic field shown in Figure 2.6. In order to observe the effects of Landau quantisation for this relatively large broadening, one can increase the magnetic field, such that the energy separation between adjacent Landau levels becomes larger, as illustrated in Figure 2.10d, where B has been increased to 4 T.

2.5.2 Shubnikov-de Haas oscillations

Figure 2.10 shows that the formation of Landau levels can be viewed as a modulation on the density of states. Therefore, in a 2D system with fixed number of electrons, continuously increasing the magnetic field will cause a gradual decrease of the Fermi level relative to the Landau level which E_F is passing through, since the density of states of each Landau level is proportional to B. As a result, the density of states at the Fermi level will oscillate as a function of magnetic field when E_F passes through different Landau levels. Correspondingly, in the regime where the magnetic field is not strong enough to completely separate the Landau levels, the magneto-resistance or conductance will also show smooth oscillations, known as the Shubnikov-de Haas (SdH) oscillations (Figure 2.11). From Equation 2.39, it can be easily deduced that the SdH oscillations

have a fixed period when plotted against $1/B$. This periodicity and the positions of the peaks can sometimes be used to distinguish different materials (such as monolayer or bilayer graphene) or to estimate the carrier density of a given system.

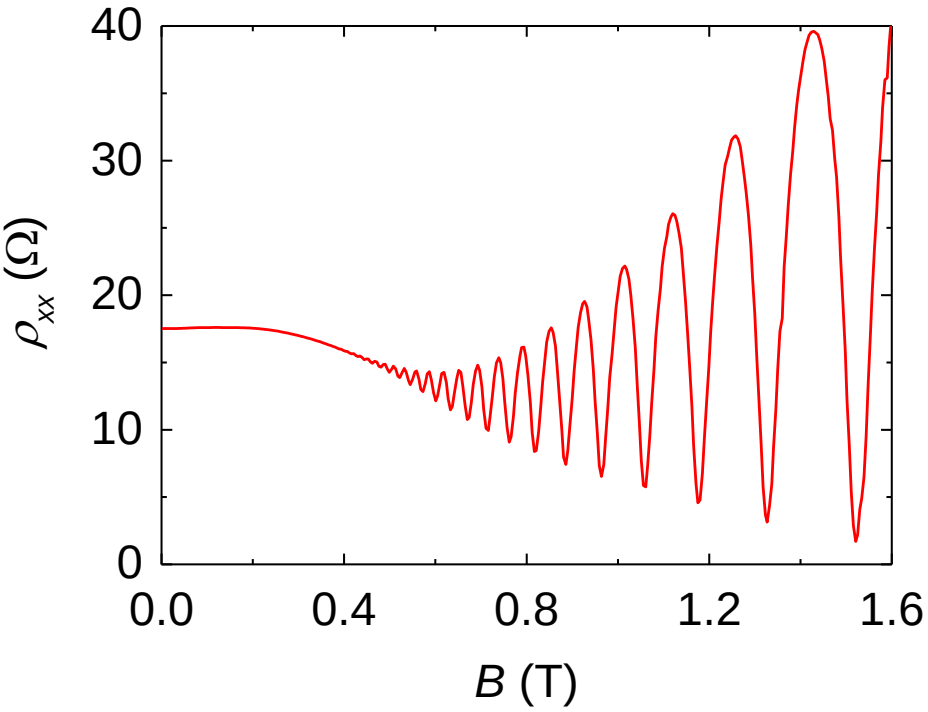

Figure 2.11: An example of the SdH oscillations of the two-dimensional electron gas in a GaAs/AlGaAs heterojunction measured at 1.4 K. The sample is provided by the National Physical Laboratory (UK).

The SdH oscillations reduce in amplitude as the temperature is increased, since higher temperatures cause further smear-out of the Fermi-Dirac distribution, so that the modulation of the density of states becomes less significant. Therefore, a thermal energy (k_BT) smaller than the Landau level separation is always required to observe clear oscillations. The temperature dependence of the oscillation amplitude, when the oscillations are relatively small, can be estimated [17] to be proportional to $\frac{\chi}{\sinh\chi}$ with

$$\chi = \frac{2\pi^2 m_c k_B T_e}{\hbar e B}, \tag{2.40}$$

where m_c is the cyclotron mass defined by Equation 2.31 and T_e is the electron temper-

ature. This is a general expression for any dispersion relation. For parabolic dispersions such as in many conventional semiconductors as well as in bilayer graphene, $m_c = m^*$, the effective mass. For monolayer graphene, even though charge carriers behave as if they have zero rest mass, they do have a finite cyclotron mass $m_c = \frac{E_F}{v_F^2} = \frac{\hbar}{v_F}\sqrt{\pi n}$, where n is the carrier density [17, 18]. Therefore, measurements of the SdH oscillations are often used to determine the cyclotron mass or the effective mass of the system. In addition, as will be shown in Chapter 6, they can also help determine the carrier temperature and eventually the energy loss rate of hot carriers in the system.

At a fixed temperature, as the magnetic field increases, the amplitude of the SdH oscillations also increases. This is because both the Landau level separation and the density of states in each level increase with the magnetic field, thus the disorder broadening will be effectively weaker (see the comparison of Figure 2.10c with Figure 2.10d).

Further increasing the magnetic field will dramatically change the smooth oscillations, and the 2D system will enter the quantum Hall regime. The SdH oscillations can often be viewed as a precursor to the quantum Hall effect, which will be discussed in the next subsection.

2.5.3 Integer quantum Hall effect

When measured at very high magnetic fields, at low temperatures and in high-quality 2D samples, the classical Hall effect and the SdH oscillations develop into unusual behaviours. In contrast to the linear Hall resistance as a function of magnetic field (Equation 2.27) and the smooth oscillations in the longitudinal resistance, a series of plateaux in the Hall resistance accompanied by zero-resistance minima in the longitudinal resistance can be observed, as shown in Figure 2.12. More strikingly, the Hall resistance at these plateaux is found to be quantised as $\rho_{xy} = \frac{1}{j}\frac{h}{e^2}$, where j is an integer, such that it is only determined by the fundamental constants h and e. Discovered by Klaus von

Klitzing in 1980 [21], this effect is called the (integer) quantum Hall effect (QHE) and the value $\frac{h}{e^2}$ is also known as the von Klitzing constant. Experimentally, the quantised Hall resistance is robust and can be measured with remarkable accuracy, it has therefore enabled a definition of a new electrical resistance standard [22].

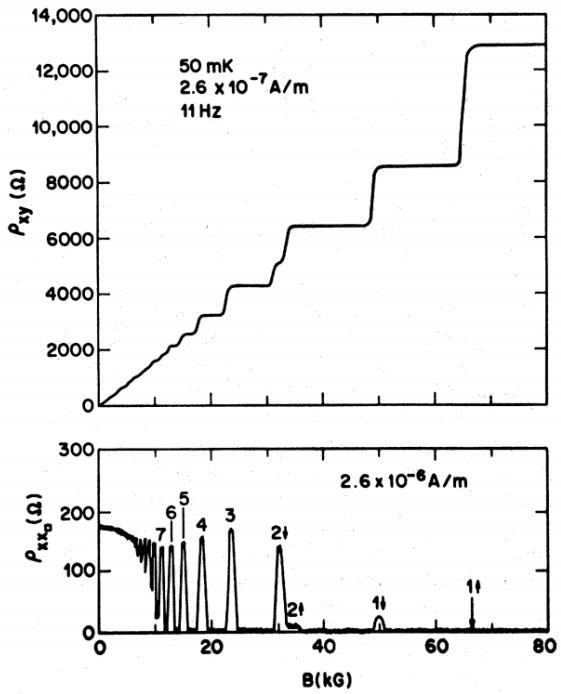

Figure 2.12: Quantum Hall effect in GaAs/AlGaAs. Adapted from Ref. [23].

Based on the classical Hall effect, if we consider the case in which the Fermi level of a sample with a fixed carrier density is at exactly the mid-point between two adjacent Landau levels at certain magnetic fields, Equation 2.27 gives a sequence of Hall resistivities consistent with the QHE,

$$\rho_{xy} = \frac{h}{\nu e^2}, \tag{2.41}$$

where ν is an integer filling factor given by Equation 2.39. Since no allowed state exists at the Fermi level, one may think that the longitudinal conductivity σ_{xx} goes to zero as in an insulator. However, the tensorial nature represented by Equation 2.26 also requires

$\rho_{xx} = \sigma_{xx} = 0$. In fact, this rather unexpected result is simply due to the absence of scattering, and also the way ρ_{xx} and σ_{xx} are defined and measured. Nevertheless, another problem of the above classical derivation is that it only predicts the correct quantum Hall resistance at exactly integer filling factors, i.e. only at specific points during a magnetic field sweep. Instead, the quantum Hall plateaux and the zero-resistance states extend over a finite range of magnetic field. To solve this mystery and better understand the conduction process in QHE, we must consider a real sample which contains disorder in the system and has a finite size.

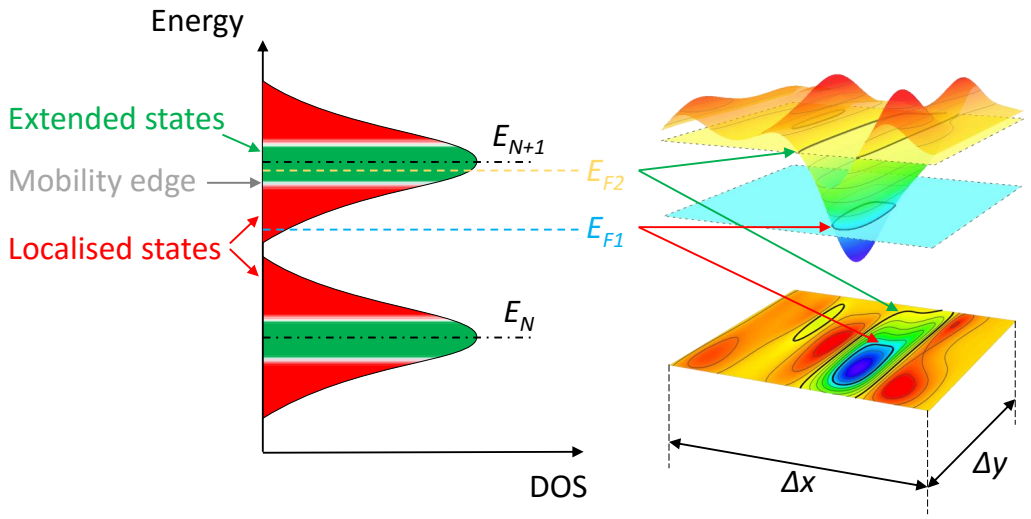

Figure 2.13: Energy spectrum and topology of disordered Landau levels.

As discussed before (Figure 2.10), Landau levels are broadened in the presence of disorder. This broadening can be pictured as spatial variations of local potentials with their mean value at the centre of the Landau level, and with the upper (lower) tail represented by hills (puddles), as shown by the potential topography of a small region ($\Delta x \times \Delta y$) of the sample in Figure 2.13. When the Fermi level is in a tail (e.g. E_{F1} in the figure), the corresponding equipotential lines form closed loops which are spatially separated. At low temperatures, the electron wavefunction is localised inside these loops and the states associated are known as the localised states. When the Fermi level enters

the central region of a Landau level (such as E_{F2}), the loops of equipotential lines are opened and extended across the whole region. These states around the centres of Landau levels are called the extended states. Theoretical studies have shown that a mobility edge exists between the tail and the centre of a Landau level separating localised states from extended states [24, 25]. The existence of localised and extended states in broadened Landau levels [26] can be used to explain the observed finite width of the quantised ρ_{xy} and the zero ρ_{xx}. In a larger landscape across the whole sample, when the Fermi scans through the localised states from a Landau level to the next, electrons are localised in isolated small regions and do not contribute to conduction. Therefore, ρ_{xy} and ρ_{xx} remain unchanged. When E_F is in the extended states close to the centres of Landau levels, electrons are allowed to move through the sample resulting non-zero ρ_{xx}.

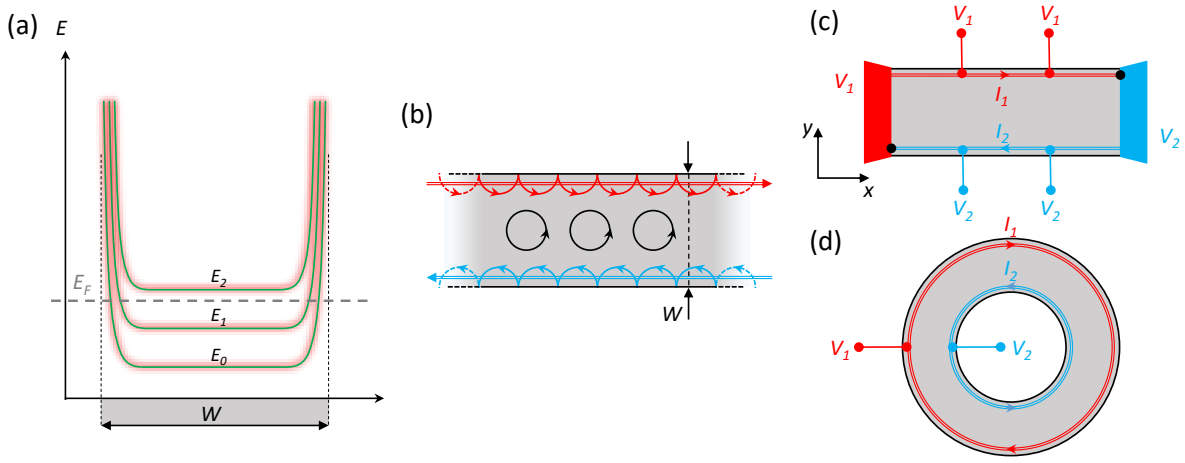

Figure 2.14: (a) Landau levels in a sample with a finite width. (b) Formation of chiral edges states and "skipping orbits". (c),(b) Measurements of the QHE in a Hall bar and a Corbino disk geometry.

To answer the remaining question of why an electrical current can still be applied to the sample at quantum Hall states where the Fermi level is in the localised states, the finite size of a sample must be taken into account. Instead of periodic boundary conditions, a finite sample width requires that the energy spectrum becomes extremely steep at the edges, as shown in Figure 2.14, such that electrons can be confined within

the sample. When the Fermi level is between the Landau levels E_2 and E_1 (Figure 2.14a), two edge states exist on each side of the sample [27]. These two edge states belong to the two Landau levels below E_F and are extended along the perimeter of the sample forming edge channels [28]. Inside these channels, since the Landau levels are only partially filled, the electron gas is compressible and extra electrons can be easily pumped into the system from metal contacts, allowing current flow along the edges. More importantly, these one-dimensional current-carrying edge channels are chiral with perfect transmission [29], meaning all electrons move in the same direction in all the edge channels on one edge of the sample and all electrons on the other edge of the sample move in the opposite direction, without backscattering. This is illustrated in Figure 2.14b, and can be easily understood from a simple-minded classical perspective. In a perpendicular magnetic field, the cyclotron trajectories far away from the edges are circular orbits localised in the middle region of the sample due to disorder. The electrons within a cyclotron radius close to the edges, however, are reflected by the sample boundaries before completing a full circle, thus forming "skipping orbits" [27]. As shown in Figure 2.14b, the upper edge can only support the right-moving states (red) and the lower edge has only the left-moving ones, so the edge states are chiral. Electrons on either edge can not reverse their moving directions, therefore, they do not suffer from backscattering, as if they are free electrons moving along equipotential lines whose potentials coincide with those of the electron pumps (i.e. contacts).

Based on the Landauer formalism [30], treating every chiral edge state as a perfect current transport channel, the QHE has been very successfully described [22, 27, 29]. For a Hall bar geometry shown in Figure 2.14c, the edge current is given as a function of the electrochemical potential of the injecting contact,

$$I_1 = \nu G_0 V_1, \qquad I_2 = \nu G_0 V_2, \tag{2.42}$$

where $G_0 = \frac{e^2}{h}$ is the conductance quantum, and ν is the integer filling factor equal to the number of channels. A small net current I_x in the x direction requires $I_x = I_1 - I_2 = \frac{\nu e^2}{h}(V_1 - V_2)$. Since the both edges are equipotential lines, $V_x = 0$ and therefore $\rho_{xx} = \frac{W}{L}\frac{V_x}{I_x} = 0$. The current in the y direction is prohibited due to the large spacial separation of the red and blue channels, and the Hall voltage $V_y = V_1 - V_2$. Thus the quantised $\rho_{xy} = \frac{V_y}{I_x} = \frac{h}{\nu e^2}$. This model also predicts that dissipation can only occur at the points where there is a voltage drop, i.e. at the points where the incoming currents meet the contacts (black dots in Figure 2.14c), as is exactly observed in the experiment [31]. For a Corbino geometry, we define the x direction to be the radial direction, and the y direction to be along the circumference. If a small potential difference $V_x = V_1 - V_2$ is applied, edge currents will flow clockwise and counter-clockwise at the outer and inner edge, respectively, followed by the same relations given by Equation 2.42. Similarly, no current can flow between the two edges, so $I_x = 0$ and the longitudinal conductivity $\sigma_{xx} = 0$. The Hall current $I_y = I_1 - I_2$, and the Hall conductivity $\sigma_{xy} = \frac{I_y}{V_x} = \frac{\nu e^2}{h}$.

The QHE can often be alternatively measured by sweeping the Fermi level at fixed magnetic fields, such as by applying and changing a gate voltage. Figure 2.15 shows the QHE in monolayer and bilayer graphene, with quantised Hall conductivities at filling factors $4(N + \frac{1}{2})$ and $4(N + 1)$, respectively, where $N = 0, 1, 2, 3....$ Compared with GaAs/AlGaAs in which QH plateaux are at $\nu = 2(N+1)$ neglecting the spin degeneracy, the anomalous filling factors in monolayer and bilayer graphene are direct consequences of the unique Landau level spectra of the two systems containing massless and massive Dirac fermions as discussed in Section 2.5.1.

Quantum Hall states are always better defined at lower temperatures, smaller applied currents and higher magnetic fields. This is because at increased temperatures, currents and/or lowered magnetic fields, the probability of thermal excitation between localised and extended states increases, causing dissipation and gradual increase in the longitudinal resistivity. Moreover, it has been long known that upon increasing the cur-

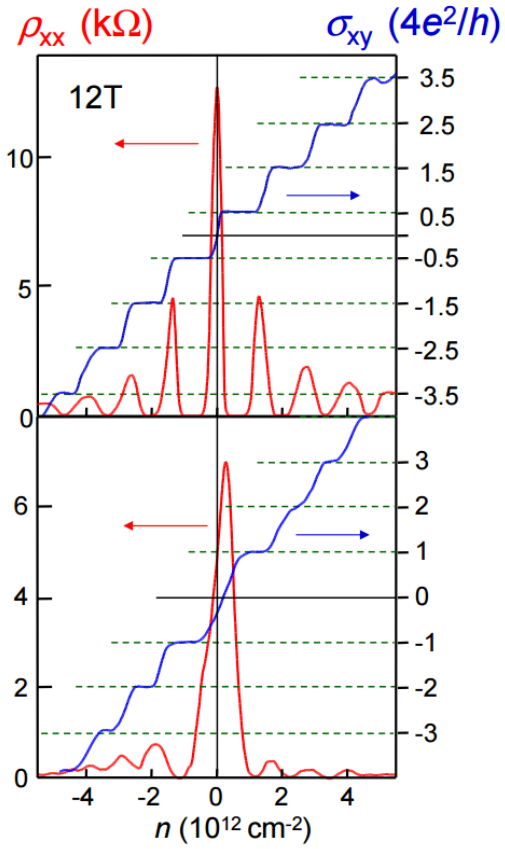

Figure 2.15: Quantum Hall effect in monolayer graphene (top) and AB-stacked bilayer graphene (bottom). Adapted from Ref. [17].

rent (or Hall field) beyond a critical value, an abrupt increase in the ρ_{xx} and derivation in the quantised ρ_{xy} [32, 33] can be observed. This observation is known as the breakdown of the QHE. While much theoretical and experimental effort has been made on this phenomenon over the past three decades, its exact nature remains unclear [22, 27, 29, 34–39]. Among them, two theories based on the bootstrap-type electron heating (BSEH) by Komiyama and Kawaguchi [38], and the quasielastic inter-Landau level scattering (QILLS) by Eaves [37, 39] have been particularly successful in explaining some observations, especially in predicting the observed $B^{3/2}$ dependence of the critical field. Nonetheless, a unified description of the quantum Hall breakdown is still missing, as it seems to depend on microscopic details of the 2DEG [22].

Understanding the quantum Hall breakdown is crucial not only for the complete understanding of the QHE but also for defining the international standard for resistance based on accurate measurements of the von Klitzing constant. Practically, one must consider the ease of using low temperatures and high magnetic fields. At the same time, the applied current must be large enough to achieve the desired signal-to-noise ratio. The emergence of graphene and related 2D materials has offered a new playground to test and develop theories of the quantum Hall breakdown, as well as new possibilities in the quantum Hall metrology. It has been demonstrated that the hot carrier relaxation time in monolayer graphene can be an order of magnitude lower than that in GaAs [40, 41]. Together with a much larger cyclotron gap (see Figure 2.9 for comparison), monolayer graphene can support a quantum Hall breakdown current density as large as 43 Am^{-1}, more than 30 times larger than previously observed in other materials [42]. In addition to the large breakdown current density, due to a magnetic field dependent charge transfer mechanism, the $\nu = 2$ quantum Hall state in epitaxial graphene becomes extremely wide [43], enabling quantum Hall measurements with an accuracy of three parts per billion at 300 mK [44], as well as in a cryogen-free table-top system operating at 3.8 K and below 5 T with metrological accuracy [45]. In Chapter 5, this charge transfer mechanism and its impact on the quantum Hall breakdown is discussed. In Chapter 6, hot carrier relaxation in bilayer graphene is investigated, and its significance on the quantum Hall metrology is addressed by comparing with monolayer graphene and conventional 2D systems.

Bibliography

[1] R. Bistritzer and A. H. MacDonald, Phys. Rev. B **84**, 035440 (2011).

[2] J. M. B. Lopes dos Santos, N. M. R. Peres, and A. H. Castro Neto, Phys. Rev. Lett. **99**, 256802 (2007).

[3] A. V. Rozhkov, A. O. Sboychakov, A. L. Rakhmanov, and F. Nori, Phys. Rep. **648**, 1 (2016).

[4] E. V. Castro, K. S. Novoselov, S. V. Morozov, N. M. R. Peres, J. M. B. Lopes dos Santos, J. Nilsson, F. Guinea, A. K. Geim, and A. H. Castro Neto, Phys. Rev. Lett. **99**, 216802 (2007).

[5] P. R. Wallace, Phys. Rev. **71**, 622 (1947).

[6] S. Reich, J. Maultzsch, C. Thomsen, and P. Ordejón, Phys. Rev. B **66**, 035412 (2002).

[7] R. Saito, M. Fujita, G. Dresselhaus, and M. S. Dresselhaus, Appl. Phys. Lett. **60**, 2204 (1992).

[8] R. S. Deacon, K.-C. Chuang, R. J. Nicholas, K. S. Novoselov, and A. K. Geim, Phys. Rev. B **76**, 081406 (2007).

[9] E. McCann and M. Koshino, Rep. Prog. Phys. **76**, 056503 (2013).

[10] A. H. Castro Neto, F. Guinea, N. M. R. Peres, K. S. Novoselov, and A. K. Geim, Rev. Mod. Phys. **81**, 109 (2009).

[11] A. K. Geim and K. S. Novoselov, Nat. Mater. **6**, 183 (2007).

[12] E. McCann and V. I. Fal'ko, Phys. Rev. Lett. **96**, 086805 (2006).

[13] E. H. Hall, Am. J. Math. **2**, 287 (1879).

[14] E. McCann, K. Kechedzhi, V. I. Fal'ko, H. Suzuura, T. Ando, and B. L. Altshuler, Phys. Rev. Lett. **97**, 146805 (2006).

[15] G. Bergmann, Phys. Rep. **107**, 1 (1984).

[16] D.-K. Ki, D. Jeong, J.-H. Choi, H.-J. Lee, and K.-S. Park, Phys. Rev. B **78**, 125409 (2008).

[17] M. I. Katsnelson, Mater. Today **10**, 20 (2007).

[18] K. S. Novoselov, A. K. Geim, S. V. Morozov, D. Jiang, M. I. Katsnelson, I. V. Grigorieva, S. V. Dubonos, and A. A. Firsov, Nature **438**, 197 (2005).

[19] K. Zou, X. Hong, and J. Zhu, Phys. Rev. B **84**, 085408 (2011).

[20] Y. Zhang, Z. Jiang, J. P. Small, M. S. Purewal, Y.-W. Tan, M. Fazlollahi, J. D. Chudow, J. A. Jaszczak, H. L. Stormer, and P. Kim, Phys. Rev. Lett. **96**, 136806 (2006).

[21] K. von Klitzing, G. Dorda, and M. Pepper, Phys. Rev. Lett. **45**, 494 (1980).

[22] B. Jeckelmann and B. Jeanneret, Rep. Prog. Phys. **64**, 1603 (2001).

[23] M. A. Paalanen, D. C. Tsui, and A. C. Gossard, Phys. Rev. B **25**, 5566 (1982).

[24] T. Ando, J. Phys. Soc. Jpn. **52**, 1740 (1983).

[25] A. MacKinnon, L. Schweitzer, and B. Kramer, Surf. Sci. **142**, 189 (1984).

[26] K. von Klitzing, Rev. Mod. Phys. **58**, 519 (1986).

[27] R. J. Haug, Semicond. Sci. Technol. **8**, 131 (1993).

[28] D. B. Chklovskii, B. I. Shklovskii, and L. I. Glazman, Phys. Rev. B **46**, 4026 (1992).

[29] M. Büttiker, Phys. Rev. B **38**, 9375 (1988).

[30] R. Landauer, Philos. Mag. **21**, 863 (1970).

[31] U. Klass, W. Dietsche, K. von Klitzing, and K. Ploog, Surf. Sci. **263**, 97 (1992).

[32] M. E. Cage, R. F. Dziuba, B. F. Field, E. R. Williams, S. M. Girvin, A. C. Gossard, D. C. Tsui, and R. J. Wagner, Phys. Rev. Lett. **51**, 1374 (1983).

[33] G. Ebert, K. von Klitzing, K. Ploog, and G. Weinmann, J. Phys. C: Solid State Phys. **16**, 5441 (1983).

[34] G. Nachtwei, Physica E: Low Dimens. Syst. Nanostruct. **4**, 79 (1999).

[35] P. Streda and K. von Klitzing, J. Phys. C: Solid State Phys. **17**, L483 (1984).

[36] S. Komiyama, T. Takamasu, S. Hiyamizu, and S. Sasa, Solid State Commun. **54**, 479 (1985).

[37] L. Eaves and F. W. Sheard, Semicond. Sci. Technol. **1**, 346 (1986).

[38] S. Komiyama and Y. Kawaguchi, Phys. Rev. B **61**, 2014 (2000).

[39] L. Eaves, Physica B Condens. Matter **298**, 1 (2001).

[40] A. M. R. Baker, J. A. Alexander-Webber, T. Altebaeumer, and R. J. Nicholas, Phys. Rev. B **85**, 115403 (2012).

[41] A. M. R. Baker, J. A. Alexander-Webber, T. Altebaeumer, S. D. McMullan, T. J. B. M. Janssen, A. Tzalenchuk, S. Lara-Avila, S. Kubatkin, R. Yakimova, C.-T. Lin, L.-J. Li, and R. J. Nicholas, Phys. Rev. B **87**, 045414 (2013).

[42] J. A. Alexander-Webber, A. M. R. Baker, T. J. B. M. Janssen, A. Tzalenchuk, S. Lara-Avila, S. Kubatkin, R. Yakimova, B. A. Piot, D. K. Maude, and R. J. Nicholas, Phys. Rev. Lett. **111**, 096601 (2013).

[43] T. J. B. M. Janssen, A. Tzalenchuk, R. Yakimova, S. Kubatkin, S. Lara-Avila, S. Kopylov, and V. I. Fal'ko, Phys. Rev. B **83**, 233402 (2011).

[44] A. Tzalenchuk, S. Lara-Avila, A. Kalaboukhov, S. Paolillo, M. Syväjärvi, R. Yakimova, O. Kazakova, T. J. B. M. Janssen, V. Fal'ko, and S. Kubatkin, Nat. Nanotechnol. **5**, 186 (2010).

[45] T. J. B. M. Janssen, S. Rozhko, I. Antonov, A. Tzalenchuk, J. M. Williams, Z. Melhem, H. He, S. Lara-Avila, S. Kubatkin, and R. Yakimova, 2D Mater. **2**, 035015 (2015).

3

Experimental Methods

This chapter begins with an introduction to common synthesis methods of graphene and related 2D materials. Identification and initial characterisation techniques of as-grown/pre-processed samples are then described before the details of device fabrication are given. Finally, the set-up for magnetotransport measurements is illustrated.

Contents

3.1 Synthesis of graphene and related 2D materials

Graphene and related 2D materials can be produced physically and chemically in a variety of ways, which are generally categorised into top-down and bottom-up approaches. Depending on the exact nature of the physical or chemical processes involved, the same material synthesised from different methods can exhibit various characteristics, thus may be suitable for different applications and researches.

3.1.1 Mechanical exfoliation

Mechanical exfoliation refers to a top-down method to isolate single or few layers of 2D materials by breaking van der Waals' forces in their layered bulk crystals. Graphene, as an example, was first isolated by mechanical exfoliation from natural graphite and highly-oriented pyrolytic graphite (HOPG) [1]. This process involves repeated peeling of the bulk material using an adhesive tape, such as the Scotch tape, hence the Scotch-tape method.

In more detail, a piece of graphite with a clean surface (Figure 3.1a) is firmly pressed on to the tape. By carefully peeling off the tape and removing the bulk piece, thin and shiny layers of graphite are left on the tape (Figure 3.1b). The next step is repeatedly folding and unfolding the tape, such that the graphite layers are gradually thinned down. Fresh pieces of tape can sometimes be used to continue this process by transferring some graphite flakes from the previous piece of tape, if the original graphite flakes are too thick. Eventually, the flakes on the tape is no longer shiny but are semi-transparent and evenly distributed on the tape (Figure 3.1c). At this point, the tape is gently pressed onto a piece of pre-cleaned substrate, such as Si/SiO_2, and is then removed. The substrate is now left with ultra-thin graphite flakes, among which single or few layer graphene can often be found.

Even though this method is borne by the name of Scotch tape, the Scotch tape is in fact not particularly suitable for mechanical exfoliation because it is too sticky and soft, leaving the exfoliated graphene flakes with a lot of tape residues and cracks/wrinkles. Instead, less sticky and more rigid types of tape are normally used, such as a blue transparent Nitto tape, which is also widely used in the semiconductor manufacturing process. Mechanically exfoliated graphene flakes can easily get microns large. With careful optimisations of the process, such as controlling the peeling speed and the force applied, as well as pre-treatments of the substrate (ultrasonic cleaning, baking, plasma

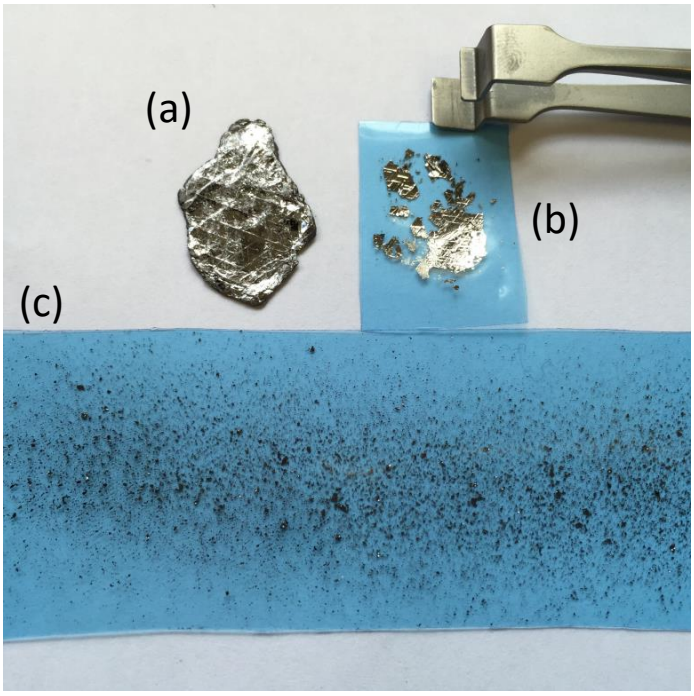

Figure 3.1: Graphene isolation by mechanical exfoliation of natural graphite.

etching, etc), sub-millimetre sized single layer flakes can be achieved [2].

The main advantage of mechanically exfoliated graphene and other 2D materials is that they are normally single crystals with very few defects, thus preserving the high quality of the bulk materials. The most significant factors that affect their quality are from the interactions between the exfoliated flakes and the substrate. Graphene on Si/SiO_2 substrates suffers from limited mobilities due to scattering from charged impurities in the substrate [3], while graphene devices on/encapsulated in hexagonal boron nitride [4–6] or suspended above the substrate [7, 8] show substantial improvement in quality. Mechanical exfoliated graphene is generally suitable for fundamental research and prototyping due to the simplicity and effectiveness of this method. However, it is unlikely that this method would have an industrial scale-up towards commercialisation of relevant applications due to the randomness in finding the required number of layers and the lack of controllability in the exfoliation process.

3.1.2 Chemical vapour deposition

Graphene and many other 2D materials can also be synthesised by chemical vapour deposition (CVD) on catalytic metals. While many different routes exist in the CVD growth specific to different materials, the choice of metal substrates and the expected crystalline forms, a typical growth of graphene follows pre-treatment of the metal substrate at elevated temperature ($\sim$ 1000 °C) in a hydrogen environment, graphene nucleation by passing through carbon-containing precursor (such as methane or hexane), and a subsequent cooling process [9]. The as-grown material is on a metal substrate and can be directly characterised by scanning electron microscopy or (angle-resolved) photo-emission spectroscopy. It can be then transferred onto arbitrary substrates by dry or wet transfer techniques [10], after which devices can be fabricated. Examples of the catalytic metals used include Ni [11], Pd [12], Pt [13], Ir [14], and Cu [15].

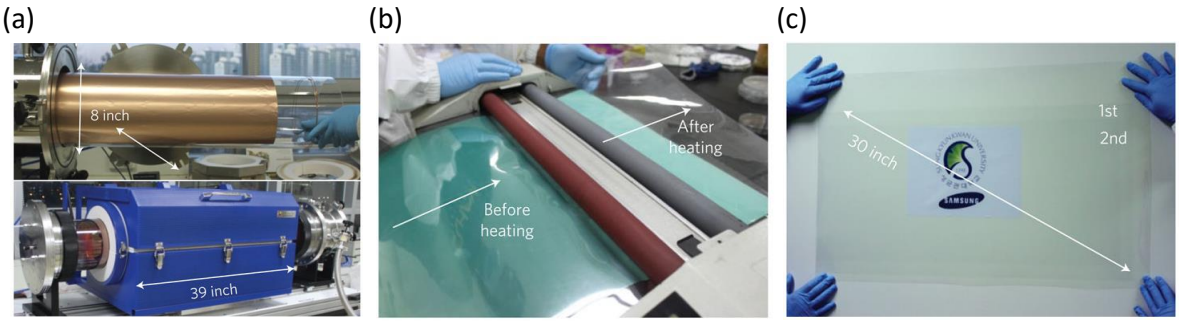

Figure 3.2: Roll-to-roll production of 30-inch graphene by CVD. Adapted from Ref. [16] (a) Copper foil wrapping around a 7.5-inch quartz tube to be inserted into an 8-inch quartz reactor. The lower image shows the stage in which the copper foil reacts with CH_4 and H_2 gases at high temperatures. (b) Roll-to-roll transfer of graphene films from a thermal release tape to a PET film at 120 °C. (c) A transparent ultralarge-area graphene film transferred on a 35-inch PET sheet.

CVD is a reproducible bottom-up method [15] and can be easily scaled up. It is demonstrated that 30-inch graphene films can be grown on Cu and transferred onto a flexible substrate by a roll-to-roll process (Figure 3.2 [16]), with sheet resistance as low as 125 $\Omega\square^{-1}$ and 97.4% optical transmittance, very promising to replace ITO as

transparent and flexible electrodes. The CVD method also shows a great advantage in fabricating heterostructures based on 2D materials, especially TMDs [17–20]. However, the CVD method is rather cost-ineffective since the metal substrate, which is often expensive, needs to be removed eventually. Moreover, CVD grown 2D materials are often polycrystalline with a significant amount of atomic defects. The involvement of the transfer process may also result in cracks and ripples in the sample [21]. Consequently, the quality is generally lower than that of the exfoliated materials concerning the high doping level and the reduced carrier mobility.

3.1.3 Epitaxial growth of graphene on SiC

Another bottom-up method to grow high quality graphene is by sublimating Si atoms on either the silicon or the carbon face of SiC, forming a carbon rich surface from which an epitaxial graphene layer is nucleated. This process can be done by annealing commercial SiC substrates at high temperatures ($>$ 1000 °C) in ultra-high vacuum or an argon atmosphere [22, 23]. Epitaxial graphene grown on the silicon face has a slow growth rate, and contains predominantly uniform monolayer over large areas [24–26]. The multilayers regions are also usually Bernal stacked [23]. On the carbon face, graphene can grow much faster, but it tends to become decoupled multilayer with a significant amount of rotational disorder and defects [23, 27, 28]. On both faces, a defective carbon-rich interfacial layer exists below the graphene, known as the buffer layer. The buffer layer is covalently bonded to the underlying SiC, leaving dangling bonds at the graphene/SiC interface (Figure 3.3) [29, 30]. Defects in the buffer layer create localised surface states widely distributed within the SiC bandgap, giving rise to a significant magnetic field dependent doping to the epitaxial graphene layer [26, 31]. Upon post-growth H_2 annealing, the dangling bonds can be saturated, minimising the effects of the buffer layer, thus reducing doping and improving carrier mobility [30, 32,

33].

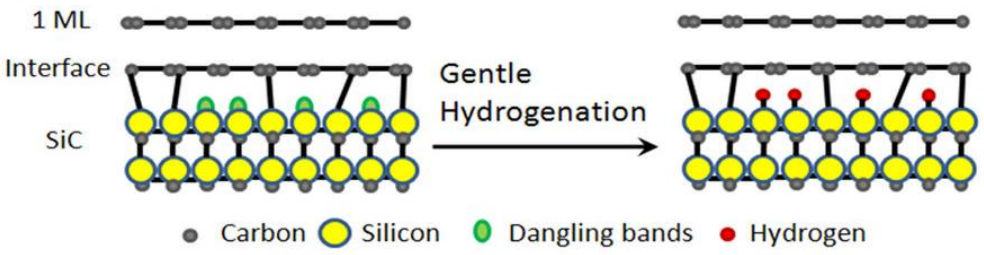

Figure 3.3: Schematic diagram of the epitaxial graphene/SiC interface. Dangling bonds exist due to the defective buffer layer, and can be eliminated by the hydrogenation process. Adapted from Ref. [30]

Using epitaxial graphene, high-frequency transistors that outperform state-of-the-art silicon transistors have been demonstrated [34]. An extremely accurate quantum Hall resistance standard based on epitaxial graphene has also been established [24]. Nevertheless, this synthesis method requires high temperature which is not directly compatible with the existing silicon technology, while the high cost of SiC wafers and the unfavourable formation of step-like terraces with multilayer inclusions on the edges further hinder its current commercialisation [21].

3.1.4 Other synthesis methods

In addition to the three major methods introduced above, a number of other techniques exist for synthesising 2D materials. When specific to graphene, these techniques may include reduction of graphene oxide [35, 36], unzipping carbon nanotubes [37, 38], and selective laser ablation [39]. Another interesting method to produce sub-micron-sized 2D materials is the liquid-phase exfoliation, by shearing off individual layers in solvents with matched surface energies [40]. The shear force can be supplied by ultrasonication, centrifugation or simply using a kitchen blender [40–42]. This method has been used to successfully produce mono- or few-layers of many 2D materials such as graphene, h-

BN, WS_2, MoS_2, $MoSe_2$, Bi_2Se_3, etc [40–44]. Since liquid-phase exfoliation is a scalable method for producing relatively large quantities of 2D materials, it has a huge potential to become an important technology in printed electronics, coatings, reinforced composite materials, and solution-processed solar cells [21, 40, 45].

3.2 Common identification techniques

In order to fabricate high quality devices suitable for magnetotransport measurements from the as-grown 2D materials, it is necessary to first identify and select the flake/area with the required number of layers while avoiding obvious defects such as dirts, cracks and wrinkles. This section illustrates some of the most commonly used non-destructive methods for flake identification.

3.2.1 Optical transmission and microscopy

Since it is shown that the opacity of each graphene layer under white light is exactly 2.3% up to at least five layers [46], it is therefore possible to distinguish single layer and multilayer graphene though white light absorption/transmission measurements. To minimise the measurement error, suspended graphene can be used (Figure 3.4). For detailed examination of graphene devices on transparent substrates (such as quartz, SiC), even though layer distinction is reduced due to the substrate, difference between monolayer and bilayer graphene can still be observed using a micro-transmission imaging technique [47].

Optical microscopy is an extremely fast and effective method to visualise large defects and determine the number of layers for 2D materials, especially for mechanically exfoliated samples. When on Si/SiO_2 substrates, thin flakes of 2D materials can be transparent enough to provide a modulation of the optical path, sufficient to change

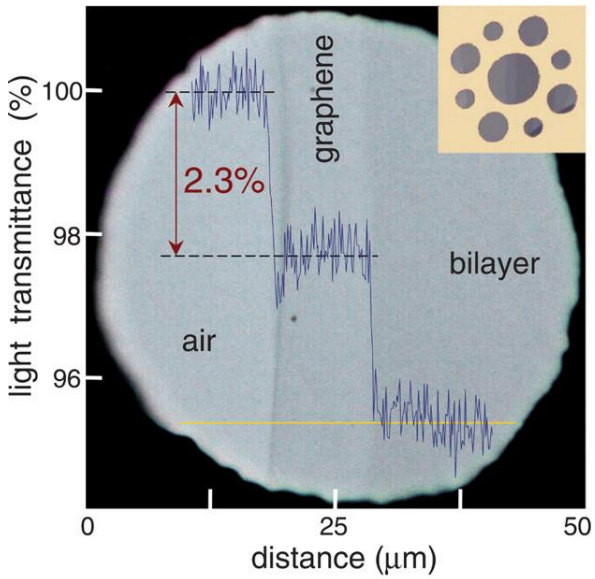

Figure 3.4: White light transmission measurements of suspended graphene. Adapted from Ref. [46]

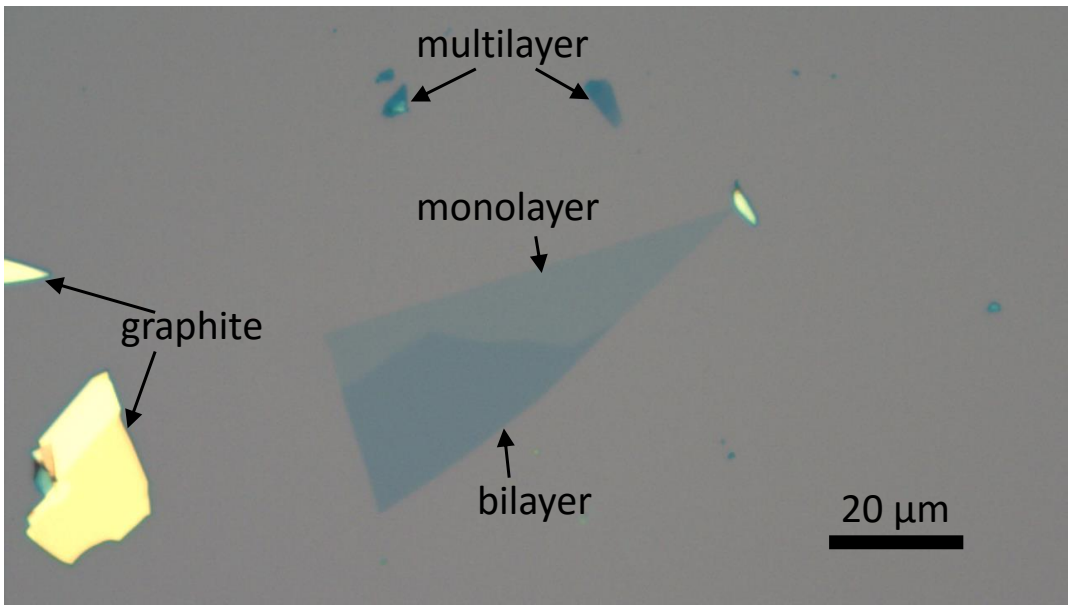

Figure 3.5: Graphene identification by optical microscopy. Flakes are produced using mechanical exfoliation on to a Si/SiO_2 (300 nm) substrate.

interference colours for the oxidised layer [48]. Therefore, one can accurately determine different numbers of layers using the colour and contrast spectra. The contrast of the interference colours will be maximised on substrates with $\sim$ 300 nm or $\sim$ 100 nm thick

SiO_2 layers and its visual detection can be made directly using an optical microscope under green or white light [49], as shown in Figure 3.5. It is noted, however, the visibility and colour spectra of graphene and other 2D materials can strongly vary from one to another and may also depend on the microscope used and the observer's experience.

In addition, it is demonstrated that, for epitaxial graphene on SiC, express optical analysis of sample morphology and layer identification can be made in transmission mode under the microscope, and the step-like terraces are also observed by differential interference contrast microscopy [50].

3.2.2 Scanning electron microscopy

Scanning electron microscopy (SEM) is a powerful and versatile tool to examine 2D materials due to their high magnification, high resolution, and ease of use. Strong contrast variations between areas with different numbers of layers can be easily observed [51]. However, it is nearly impossible to determine the exact number of layers without presumptions about the general spatial distribution of areas with different numbers of layers. More specifically, a monochromatic contrast spectrum is only well defined between layers that are sequentially grown. As shown in Figure 3.6, a full coverage of polycrystalline monolayer graphene with bilayer and trilayer regions forming a pyramid-like structure grown by CVD is observed. For exfoliated samples, each flake has a random number of layers which are often sharing the same edge, thus nearly indistinguishable by SEM. As a result, SEM is predominantly used to study CVD grown 2D materials, gaining information on layer formation, domain size and morphology, nucleation density, and sample coverage. To identify defects, on the other hand, SEM can then be employed for samples synthesised by any method.

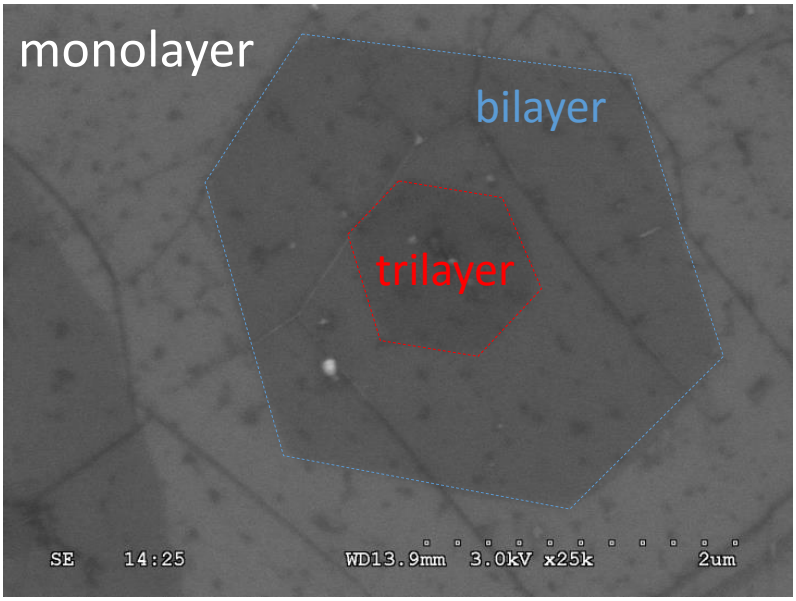

Figure 3.6: An SEM image of a CVD graphene sample on Si/SiO_2 transferred from copper foil. Polycrystalline monolayer graphene and its grain boundaries are easily seen in the background covering the whole region. Bilayer and trilayer graphene are sequentially grown around a nucleation point, forming a pyramid-like structure. This image is taken by a Hitachi S-4300 field emission SEM.

3.2.3 Atomic force microscopy

Atomic force microscopy (AFM) can be used to directly measure the thickness, shape and defect levels of deposited 2D materials. In practice, non-contact mode AFM is most often used since ideally the cantilever tip never touches the sample surface, preventing damage to the sample. In the non-contact mode, the cantilever tip is held about 5 to 10 nm above the sample during a scan. It is vibrated at a constant frequency slightly higher than its mechanical resonant frequency (typically 50 to 400 kHz) controlled by a feedback loop connected to a thin piezoelectric actuator, with an amplitude of a few tens of angstroms. As the tip is scanned across the sample surface, the vibration amplitude is modulated in response to the change in force gradients which vary with tip-to-sample spacing. The changes in vibration amplitude are detected by a deflection sensor which contains a laser, a mirror and a position-sensitive photodetector. An image showing the

topology of the sample surface is then plotted by mapping these changes.

In our laboratory, a Park Scientific Instrument AutoProbe M5 placed in an acoustic isolation enclosure is used to characterise flakes of 2D materials. It has maximum lateral and vertical scan ranges of 100 and 7.5 μm, with maximum lateral and vertical scanner resolutions of 0.25 and 0.025 Å, respectively. An example is shown in Figure 3.7, where topography and thickness of mechanically exfoliated few-layer indium selenide flakes is measured in the non-contact mode, using antimony doped Si tips (spring constant $k = 3$ N/m) with aluminium reflective coating on the backside.

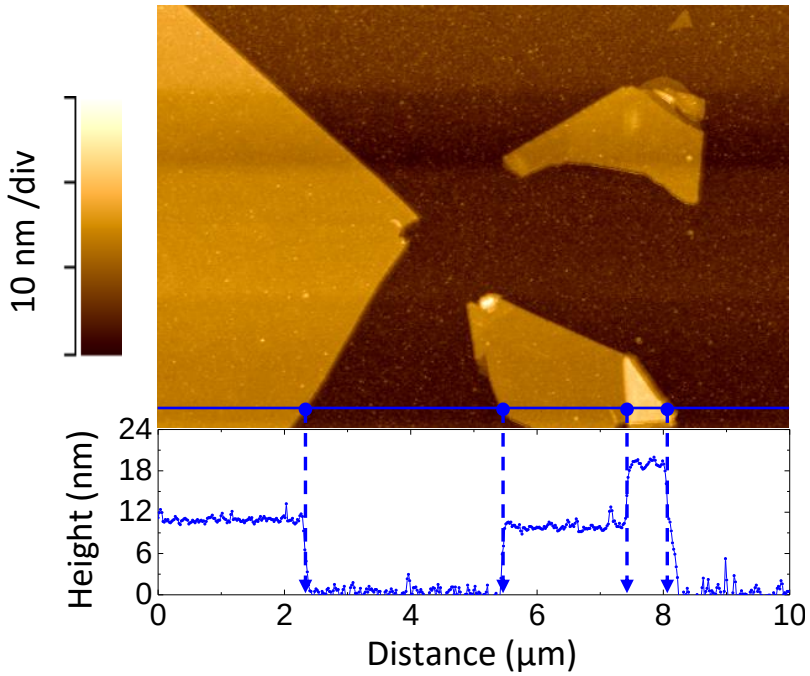

Figure 3.7: An AFM image and height profile (along the blue line) of mechanically exfoliated few-layer InSe on Si/SiO_2.

3.2.4 Raman spectroscopy

In addition to being a powerful tool to study electron-phonon interactions, Raman spectroscopy can be simply used to non-destructively determine the number of layers of 2D materials [52–55]. In the case of graphene, the Raman spectrum prominently

contains two modes/peaks, the G mode and the 2D mode. The G mode, at around 1580 cm^{-1}, originates from a first order Raman scattering process related to the double-degenerate TO and LO modes at the Γ point. The 2D mode, at around 2700 cm^{-1}, is a second order double resonant process between K and K' points connecting two TO phonons [52]. It is demonstrated that the intensity ratio of the 2D mode to the G mode (I_{2D}/I_G) is significantly dependent on the number of layers. In monolayer graphene $I_{2D}/I_G \approx 2-4$, while in AB-stacked bilayer graphene it decreases to about 1, and for more than three layers it is much smaller than 1 [56–58], as shown in Figure 3.8. Moreover, the 2D peak is much narrower and at a lower Raman shift in monolayer graphene than those in multilayer graphene.

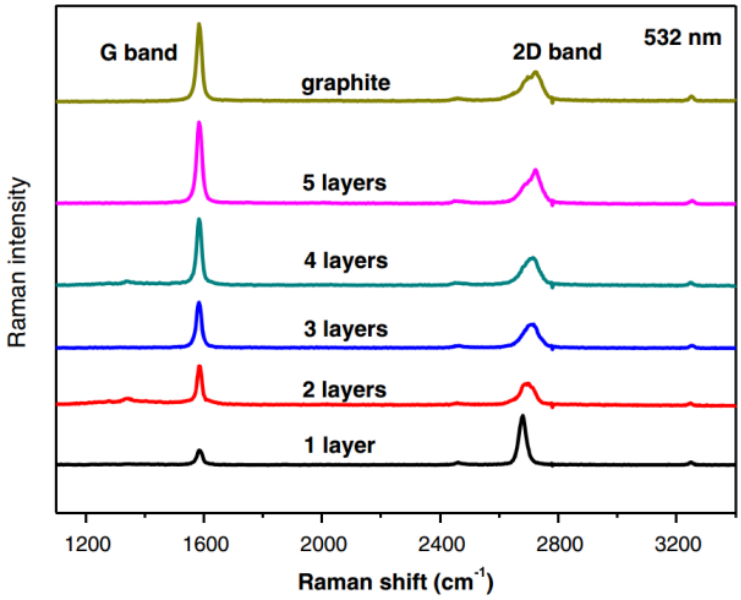

Figure 3.8: Raman spectra of graphene and its multilayer. Adapted from Ref. [58].

Sometimes the D mode, at around 1350 cm^{-1}, may appear. Similar to the 2D mode, it is a second-order process but is associated with a single phonon and a defect instead [52]. The D mode is forbidden in the absence of defects and disorder. Therefore, a sample with a more pronounced D peak tends to contain more defects.

3.3 Device fabrication

After material synthesis with necessary transfer processes, followed by flake identification as described in the previous two sections, we should now have suitable flakes on non-conductive substrates (such as SiC, Si/SiO_2) ready to be made into devices. To study magnetotransport properties of graphene and related 2D materials, simple field effect transistors and Hall bars are fabricated using electron beam lithography (EBL) or photolithography.

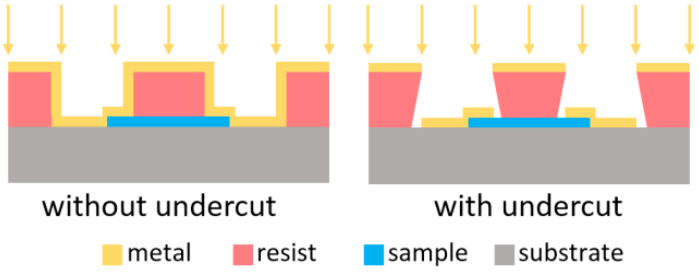

Figure 3.9: Cross-sections of lithographed devices during metal evaporation. Without an undercut profile, the top layer metal film is easily connected to the metal contacts and will be difficult to lift-off.

In these processes a chip covered by electron or ultraviolet (UV) light sensitive films ("resists") is selectively exposed by a focused electron beam or high power UV illumination. There are two types of resists: positive and negative. For positive resists, electron/UV exposure will change the chemical structure of the resists so that the exposed areas become more soluble and can be easily washed away in certain solvents ("developers"). For negative resists, just in the opposite way, the exposed areas become polymerised and difficult to dissolve in the developers, thus the unexposed areas will be washed away in the development process. After development, the chip contains open windows of bare underlying materials which can be removed by the etching process or be electrically contacted by evaporation of metals. Finally, after etching or metal evap-

oration, the remaining resist is dissolved in stronger solvents ("removers"), meanwhile, anything left on top of the resist is disconnected and removed from the sample (the "lift-off" process). An ideal exposure and development creates a small "undercut" profile (Figure 3.9), which is required for a clean and easy lift-off, such that the evaporated metal film on top of the resist is separated from the metal contacts that go through the open windows and land directly onto the flakes. Typical technical details of the EBL and photolithography processes involved to fabricate devices of 2D materials is given below.

3.3.1 Electron beam lithography

In an EBL process, selective exposure is achieved by programmed scanning of the focused electron beam in coordination with alignment marks. As shown in Figure 3.10, a full EBL design using AutoCAD normally consists of four exposure steps for alignment marks (white), bonding pads with outer contacts (red), inner contacts (blue) and the Hall bar (green), respectively.

The matrix of alignment marks, typically contains four large crosses at four corners of the sample chip, and tens or hundreds of small crosses in the central region, as shown in Figures 3.10a and b. To expose these marks, bilayer positive resists, 8% poly(methyl 2-methylpropenoate) (PMMA) with different molecular weights dissolved in anisole, are sequentially spin-coated onto the sample. The PMMA in the bottom layer has a molecular weight of 495k, and is spun at 1000 rpm for 60 seconds. The PMMA in the top layer has a molecular weight of 950k, and is spun at 5000 rpm for 60 seconds. Immediately after each spin-coating step, the chip is soft-baked on a hotplate at 180 °C for 90 seconds. The total thickness of bilayer film is approximately 1.5 μm. The chip is then exposed using a JEOL JBC-5500ZC EBL system, with a beam current of 10 nA and a dose $\sim$ 650 μC/cm^2. After exposure, the chip is developed in a mixture

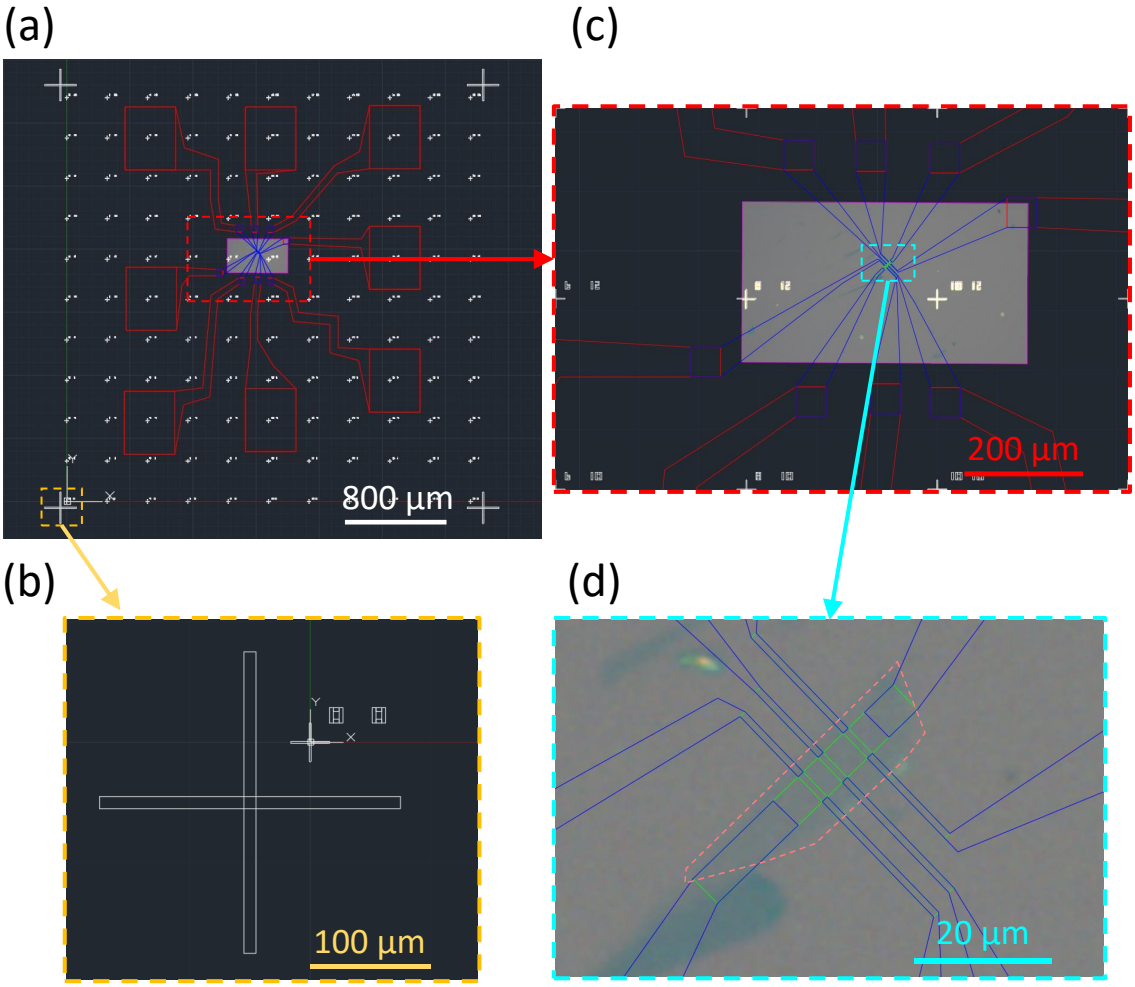

Figure 3.10: (a) A complete AutoCAD design to fabricate a graphene Hall bar device. It contains four sequential exposure steps corresponding to the white alignment marks, the red bonding pads and outer contacts, the blue inner contacts, and the green Hall bar. Depending on the size of the area to be exposed and the beam current used, the exposure time can vary from several minutes to several hours. (b) A magnified area showing the large and small alignment marks. (c) A magnified area showing the outer and inner contacts. They are added to the AutoCAD drawing by under-laying an actual image of the flake with the deposited alignment marks below the original design. (d) A magnified area showing the inner contacts to the Hall bar, which will be patterned within a monolayer graphene flake as enclosed by the pink dashed line.

of methyl-isobutyl-ketone (MIBK) and isopropanol (IPA) with a volume ratio of 1:3 for 90 seconds at room temperature, and then rinsed in pure IPA for 20 seconds. Since the bottom resist has a lower molecular weight, it is dissolved faster in the developer than the heavier top layer, thus creating the desired undercut profile. Metals can now be

evaporated onto the chip. For better adhesion of the metals, however, the chip is often etched using oxygen plasma for 30 to 40 seconds before evaporation to remove resist residues left on the exposed areas. 10 nm of Cr and 90 nm of Au are then thermally evaporated onto the chip. The purpose of evaporating a thin layer of Cr below Au is to further enhance the adhesion. After the evaporation, the lift-off process is performed by soaking the sample in warm *N*-methyl-2-pyrrolidone (NMP) or acetone for a few hours, followed by gentle agitation using plastic pipettes. When the remaining resist is fully dissolved and the top layer metal film is detached from the sample, the chip is rinsed in IPA and blow-dried.

We have now deposited Cr/Au alignment marks onto the chip. The next step is to take an image of the actual flake together with some of the alignment marks using either an optical microscope or an SEM. As shown in Figures 3.10a and c, this image is imported back into the original AutoCAD file and the actual alignment marks in the image are overlaid with the ones in the original design. This will help locate the sample flake within the alignment mark matrix, so that further designs (areas enclosed by red, blue and green solid lines in Figure 3.10) are drawn.

Next, a two-step contact deposition is made. The first step consists of the bonding pads and the outer contacts, which are relatively large metal strips approaching the sample flake (Figures 3.10a and c [red]). They are deposited following the exact same exposure, development, Cr/Au evaporation and lift-off procedures for the alignment marks. During the exposure, the large and small alignment marks are used for rough and fine locating of the designated area to be exposed. The second step consists of inner contacts which bridge the gap between the outer contacts and the flake (Figures 3.10a, c and d [blue]). The inner contacts are deposited similarly to the previous procedures with only three modifications: (1) since the features in the second step have much smaller sizes, a 1 nA current is used in the exposure to ensure the required resolution; (2) only pure Au of about 50 nm is evaporated as the inner contacts; (3) no plasma etching

is used in order to protect the flake. This two-step contacting method is employed to minimise the contact resistance to the flake and also provide good adhesion between the bonding pads and the substrate, since for electrically contacting 2D materials such as graphene, Cr/Au contacts directly onto flake normally have much higher contact resistance compared to Au only contacts, while pure Au does not stick well on the silicon substrate without a thin Cr adhesion layer. Alternatively, a one-step large-area contacting method can be used, essentially exposing the outer and inner contacts at the same time, however, this requires the deposition of Ti/Au using electron beam evaporation.

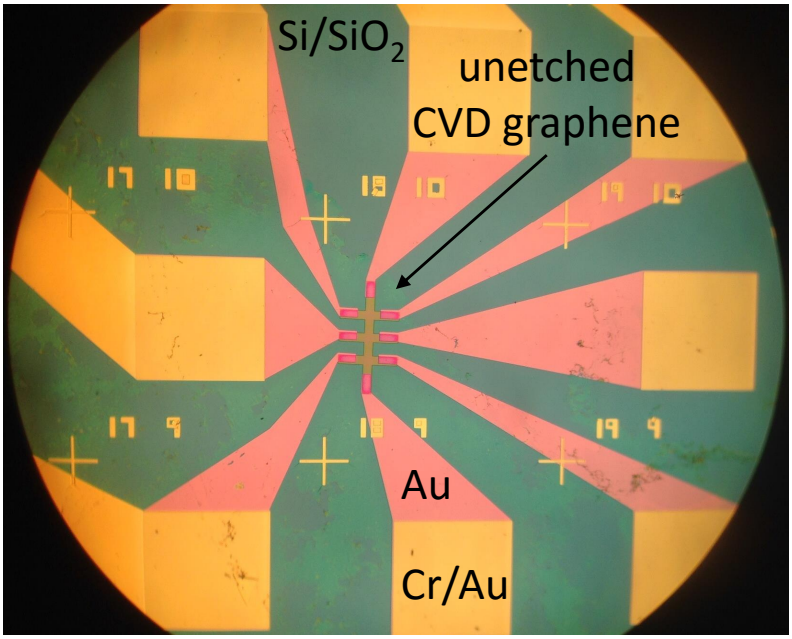

Figure 3.11: An 8-leg Hall bar of CVD graphene transferred onto a Si/SiO_2 (300 nm) substrate fabricated via EBL. This image shows the device before the final plasma etching step, with the developed negative resist on top of the Hall bar.

The final step is to define the geometry of the 8-leg Hall bar, as shown in Figure 3.10d (green). In contrast to the previous exposures, a negative resist, maN-2405, is usually used. It is spun onto the chip at 3000 rpm for 30 seconds and baked at 90 °C for 90 seconds. During the exposure, a beam current of 1 nA and a dose $\sim$ 300 $\mu C/cm^2$

are used and the area of the Hall bar enclosed by the green solid polygon lines in Figure 3.10d is exposed. After being developed in maD-533 for 65 seconds and rinsed in deionised (DI) water, the chip should now only have the Hall bar covered by the hardened negative resist with anywhere else exposed to air (see Figure 3.11). The Hall bar is then patterned by oxygen plasma etching for 30 to 50 seconds, after which the remaining resist can be removed by dissolving in acetone. With careful rinsing in IPA and drying using a nitrogen gun, the device fabrication is now finished.

3.3.2 Photolithography

Compared with EBL, photolithography has relatively lower resolution but a much faster and simpler fabrication process with the smallest feature size achievable below 1 micron using the contact method. The selective exposure is made directly though a photomask, which is normally a piece of chrome plated soda lime glass or synthetic quartz containing defined patterns. Accurate alignment between the chip and the mask is adjusted by a movable stage with a built-in microscope on the mask aligner.

To fabricate a device via photolithography, a positive photoresist MICROPOSIT S1813 is spin-coated onto the chips at 4500 rpm for 60 seconds. Three-minute soft baking at 115 °C is required to enhance adhesion of the resist. An exposure dose of 110 to 120 μC/cm^2 is used for this resist which has a thickness of 1.2 μm. In the experiment, the exposure dose is controlled from the mask aligner by adjusting the exposure time, which is normally set to be 6.5 ± 0.5 seconds for this resist. After exposure, hard baking is usually not necessary using this resist. The chip is then directly developed in 0.5% sodium hydroxide solution for 60 ± 5 seconds and rinsed in DI water for 20 seconds. Similar to the EBL process, the two-step contacting method can also be employed and a set of three photomasks (Figure 3.12) are used for exposing the bonding pads and outer contacts, the inner contacts, and the Hall bar, respectively. However, different from the

EBL process using bilayer resists, an undercut profile does not readily form with a single layer positive photoresist, thus often resulting in a difficult lift-off process with contacts shorting each other. To fix this issue, one can "pre-soak" the exposed positive resist film in an aromatic solvent, such as chlorobenzene, to modify the surface layer which develops much slower than the rest of the resist film closer to the substrate. Alternatively, an undercut can be created using a negative photoresist, along with another set of three photomasks by inverting the transparent/opaque patterns in the masks for positive resists (Figure 3.12), but the overall success rate is still lower than the method using bilayer resists in the EBL.

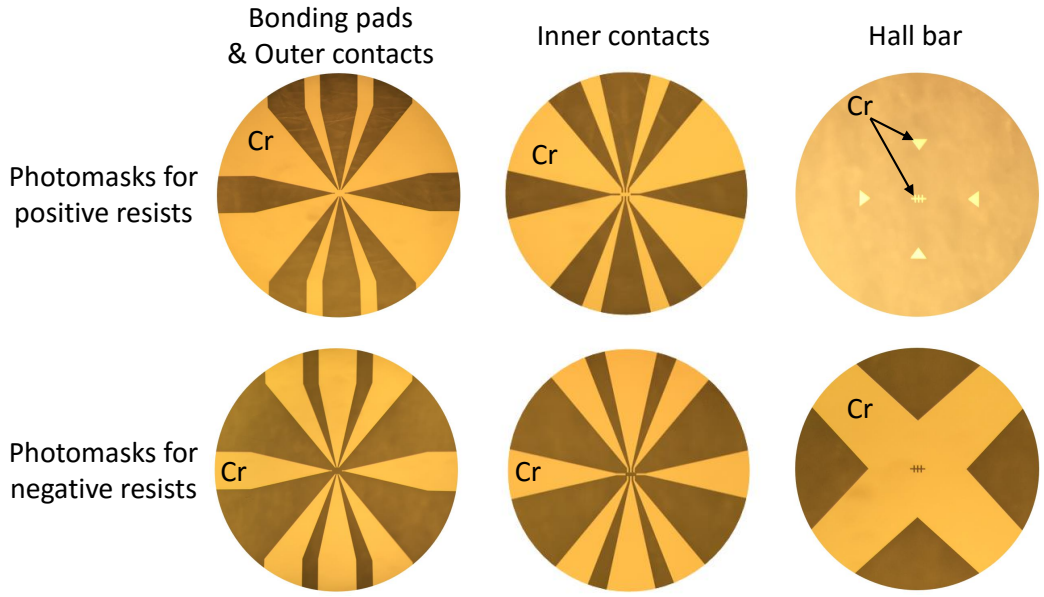

Figure 3.12: Images of two sets of photomasks for positive and negative resists. Each set contains three masks for exposing the bonding pads and the outer contacts, the inner contacts, and the Hall bar, respectively. The bright/yellow areas are coated with Cr, and the dark/grey areas are transparent.

3.4 Magnetotransport measurement techniques

3.4.1 Chip packaging, gating and wire bonding

Once a device is fabricated, it is mounted and electrically connected to a gold plated ceramic chip carrier for the ease of transport, protection and making external contacts. Depending on the size of the chips, either a smaller 16-lead chip carrier (for chip dimensions $< 4 \times 8$ mm^2) or a larger 44-leadless chip carrier (for chip dimensions $< 12 \times 12$ mm^2) can be used (Figures 3.13a and c).

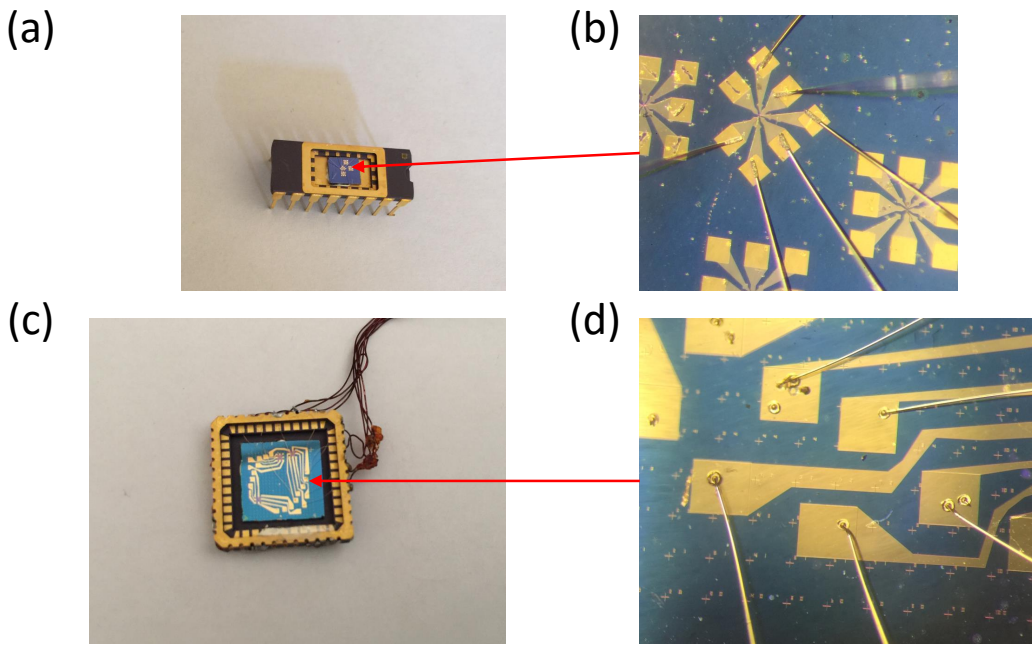

Figure 3.13: (a),(b) A 4×5 mm^2 chip mounted onto a 16-lead chip carrier. The contacts on this chip are wire bonded to the chip carrier by a wedge bonder using aluminium wires. (c),(d) A 10×10 mm^2 chip mounted onto a 44-leadless chip carrier with enamelled copper wires soldered onto the outside of the chip carrier. In this example, the contacts on this chip are wire bonded to the chip carrier by a ball bonder using gold wires.

For devices made from exfoliated or CVD materials which are on the substrate of heavily doped Si with 300 nm SiO_2, the carrier density of the flake can be tuned through

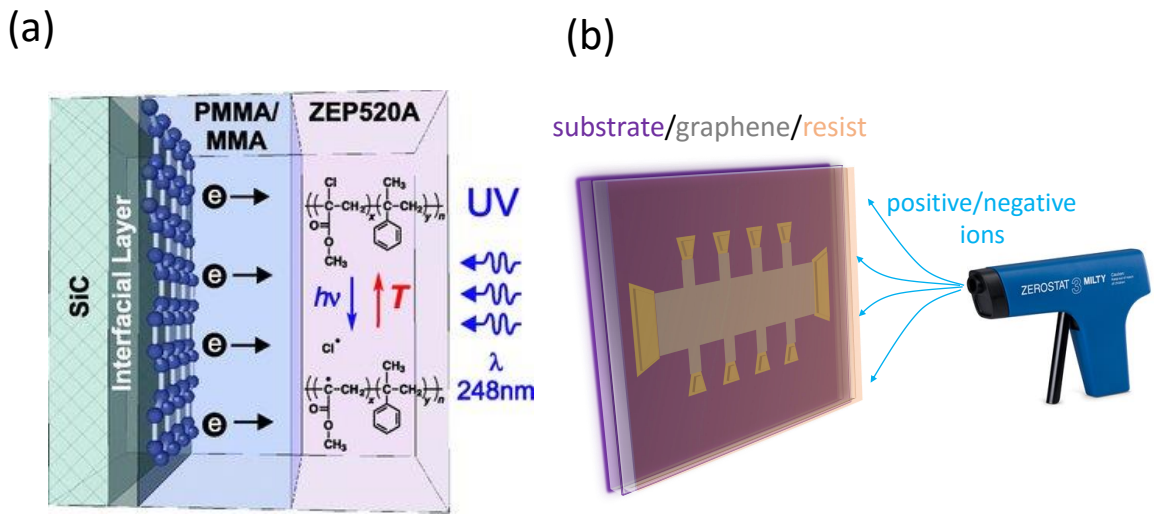

Figure 3.14: (a) Non-volatile dual polymer gating of epitaxial graphene by UV exposure. Adapted from Ref. [59]. (b) Electrostatic polymer gating by positive or negative ions produced by corona discharge using an anti-static gun.

a back gate in which the doped Si acts as the gate electrode and the thin SiO_2 is the gate dielectric. To contact the back gate, the bottom of the chip is usually scratched to expose the fresh/unoxidised doped silicon, and is mounted to the chip carrier using silver conductive paint, which is then connected to a gold terminal on the inner ring of the chip carrier to allow external contacting.

For devices such as epitaxial graphene on SiC, a top gate is usually constructed, in which case the chip can be simply stuck into the chip carrier using either the silver paint or a cryogenic-compatible non-conductive glue such as the GE varnish. The top gate can be constructed in two different methods. In the first method, two layers of polymer, PMMA/MMA and ZEP520A, are sequentially spin-coated onto the chip as shown in Figure 3.14a, and the carrier density of the flake is tuned by UV light exposure [59]. The PMMA/MMA is a dielectric spacer and ZEP520A forms a photoactive layer which provides electron acceptors upon UV illumination at room temperature, resulting

in significant reduction of the electron density. To restore the initial carrier density, the sample is simply annealed at 170 °C [59]. In the second method (Figure 3.14b), reversible tuning of the carrier density is achieved by depositing positive or negative ions generated by corona discharge from a piezo-activated antistatic gun onto a dielectric layer in ambient conditions [60]. The dielectric layer can simply be the developed resist left on the sample flake, after the flake has been etched into a Hall bar by oxygen plasma in the final step of the EBL or photolithography process (e.g. the brown Hall-bar shaped resist in Figure 3.11).

To make interconnections between each Cr/Au contact on the chip and each terminal on the chip carrier, standard wire bonding techniques are employed. Either a ball-bonder with gold bondwires or a wedge-bonder with aluminium/gold bondwires can be used, as shown in Figures 3.13b and d. For a device with a back gate, in order to protect the gate dielectric, minimum power and force is applied during the wire bonding process.

3.4.2 DC and AC electrical measurements

In a proper transport measurement, a four-terminal sensing technique is used whenever possible. In this technique, the current-carrying terminals (e.g. source and drain contacts) are separated from the voltage-sensing terminals in order to minimise the contact resistance. This is why for Hall measurements, Hall bars with at least six legs are preferred.

An accurate electrical measurement requires a high signal-to-noise ratio (S/N) which can be achieved by applying a large current. However, as discussed in Section 2.5.3 and in Chapter 5 and 6, a large current generates heat that can be more than enough to change the transport properties of the sample and even potentially damage the 2D material or the contacts. Therefore, in our measurements, a trade-off between using a high current and the risk of its side effects must be considered. For basic direct-current (DC)

characterisations of graphene devices, a suitable probe current is in the range of 50 nA to 1 μA, which is provided by a battery-powered constant current source. The advantage of using a battery-powered current source is that it provides an extremely stable output without the noise and interference commonly associated with the mains electricity, thus enhancing the S/N. The DC voltages are measured using digital multimeters (DMMs), where further filtering can be applied. Alternatively, a standard alternating-current (AC) lock-in technique can be used to provide a good S/N at low input levels. A sine-wave signal with low frequency and amplitude is injected into the source terminal of the device by a signal generator and the drain terminal is connected to the ground. The signal generator is synced with lock-in amplifiers from which the voltages are measured.

In the cases where current-dependent measurements are needed, a source-measure unit (SMU) is used to provide programmed source-drain current sweeps. The SMU also allows control of the carrier density of the sample by providing a constant or a varying potential difference between the gate and the drain electrodes.

3.4.3 High magnetic fields and low temperatures

Our primary magnetotransport measurement equipment is an Oxford Instruments superconducting magnet (Figure 3.15), which can provide a steady magnetic field up to 21 T. The magnet contains six superconducting coils immersed in a liquid helium reservoir, surrounded by a second jacket of liquid nitrogen. Operating the magnet at 4.2 K provides a maximum magnetic field of 19.0 T, beyond which a lambda point refrigerator can be used to cool the liquid helium down to 2.2 K and increase the magnetic field to 21.0 T. The inner most superconducting coil can be removed to increase the bore diameter from 40 mm to 110 mm, but with a reduced inductance hence reduced maximum fields of 16.0 T at 4.2 K and 17.6 T at 2.2 K. The magnet is powered by a bipolar 120 A - 20 V power supply, allowing a maximum energisation rate of 0.475 T/min from 0 to

19 T, and 0.228 T/min from 19 to 21 T.

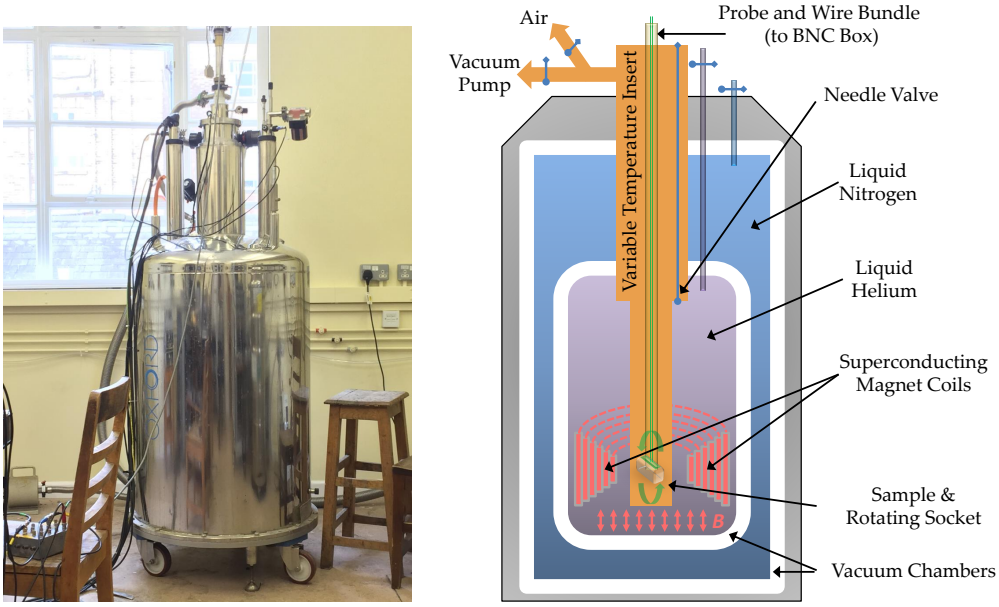

Figure 3.15: Photograph and schematic diagram of the 21 T superconducting magnet.

The temperature of the sample space can be adjusted continuously from 1.4 to 300 K using a helium-4 system and a variable temperature insert (VTI). The VTI is vacuum insulated and mounted in the liquid helium reservoir. Temperatures above 4.2 K are obtained by balancing a PID controlled heater inside the insert with the cooling power of flow of liquid helium drawn from the reservoir through a needle valve. Cooling the sample to below 4.2 K is achieved by reducing the vapour pressure of the liquid helium in the VTI by pumping the sample space using a high flow rotary pump.

The sample is mounted onto the bottom of a top loading probe (Figure 3.16a), where a 16-lead chip carrier can be directly plugged into a rotating socket (Figure 3.16d), allowing sample rotation relative to an axis perpendicular to the magnetic flux direction. For a large sample, in which rotation is prohibited in a narrow bore, a 44-leadless chip carrier is therefore fixed onto the end of the probe using GE varnish with the sample perpendicular to the probe axis, and plugged back into the socket (Figure

3.16e). The socket is connected to an I/O box with 24 Bayonet Neill-Concelman (BNC) connectors by a 24-wire bundle fed through the probe (Figure 3.16c). In this way, electrical measurements can be made simply via the BNC box.

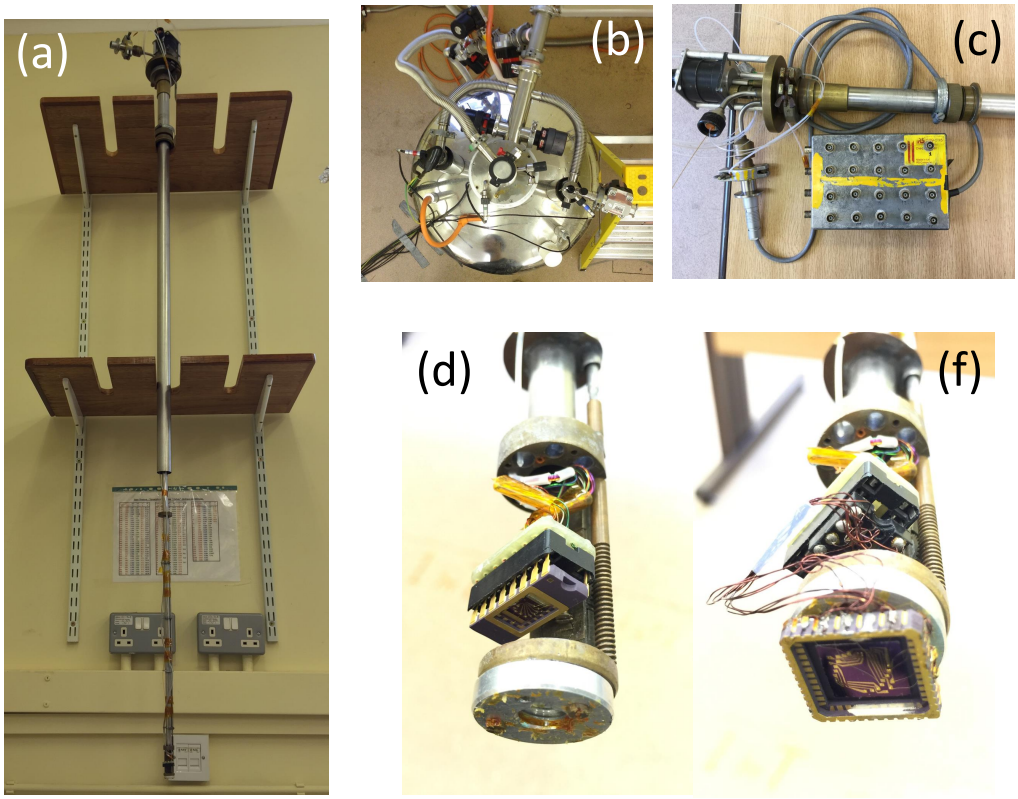

Figure 3.16: (a) Photograph of the top loading probe. (b) Top view of the magnet with the VTI. (c) A 24-terminal BNC box is connected to the sample via a wire bundle through the probe. (d) A 4×4 mm^2 chip on a 16-lead chip carrier plugged into a rotating socket at the bottom of the probe. (e) A 1×1 cm^2 chip on a 44-leadless chip carrier stuck onto the very end of the probe.

The probe is inserted into the VTI from the top of the magnet (Figure 3.16b) to the isocentre of the magnetic field in the lower part of the cryostat. Control of magnetic field sweeps and data collection are achieved through LabVIEW programmes. Heater control for the VTI is made from the front panel of a temperature controller.

Bibliography

[1] K. S. Novoselov, A. K. Geim, S. V. Morozov, D. Jiang, Y. Zhang, S. V. Dubonos, I. V. Grigorieva, and A. A. Firsov, Science **306**, 666 (2004).

[2] Y. Huang, E. Sutter, N. N. Shi, J. Zheng, T. Yang, D. Englund, H.-J. Gao, and P. Sutter, ACS Nano **9**, 10612 (2015).

[3] J.-H. Chen, C. Jang, S. Xiao, M. Ishigami, and M. S. Fuhrer, Nat. Nanotechnol. **3**, 206 (2008).

[4] C. R. Dean, A. F. Young, I. Meric, C. Lee, L. Wang, S. Sorgenfrei, K. Watanabe, T. Taniguchi, P. Kim, K. L. Shepard, and J. Hone, Nat. Nanotechnol. **5**, 722 (2010).

[5] L. Wang, I. Meric, P. Y. Huang, Q. Gao, Y. Gao, H. Tran, T. Taniguchi, K. Watanabe, L. M. Campos, D. A. Muller, J. Guo, P. Kim, J. Hone, K. L. Shepard, and C. R. Dean, Science **342**, 614 (2013).

[6] A. S. Mayorov, R. V. Gorbachev, S. V. Morozov, L. Britnell, R. Jalil, L. A. Ponomarenko, P. Blake, K. S. Novoselov, K. Watanabe, T. Taniguchi, and A. K. Geim, Nano Lett. **11**, 2396 (2011).

[7] K. I. Bolotin, K. J. Sikes, J. Hone, H. L. Stormer, and P. Kim, Phys. Rev. Lett. **101**, 096802 (2008).

[8] K. I. Bolotin, K. J. Sikes, Z. Jiang, M. Klima, G. Fudenberg, J. Hone, P. Kim, and H. L. Stormer, Solid State Commun. **146**, 351 (2008).

[9] J. H. Warner, F. Schäffel, A. Bachmatiuk, and M. H. Rümmeli, *Graphene: Fundamentals and emergent applications* (Elsevier, 2012).

[10] J. W. Suk, A. Kitt, C. W. Magnuson, Y. Hao, S. Ahmed, J. An, A. K. Swan, B. B. Goldberg, and R. S. Ruoff, ACS Nano **5**, 6916 (2011).

[11] K. S. Kim, Y. Zhao, H. Jang, S. Y. Lee, J. M. Kim, K. S. Kim, J.-H. Ahn, P. Kim, J.-Y. Choi, and B. H. Hong, Nature **457**, 706 (2009).

[12] S.-Y. Kwon, C. V. Ciobanu, V. Petrova, V. B. Shenoy, J. Bareño, V. Gambin, I. Petrov, and S. Kodambaka, Nano Lett. **9**, 3985 (2009).

[13] V. Babenko, A. T. Murdock, A. A. Koós, J. Britton, A. Crossley, P. Holdway, J. Moffat, J. Huang, J. A. Alexander-Webber, R. J. Nicholas, and N. Grobert, Nat. Commun. **6** (2015).

[14] J. Coraux, A. T. N'Diaye, C. Busse, and T. Michely, Nano Lett. **8**, 565 (2008).

[15] X. Li, W. Cai, J. An, S. Kim, J. Nah, D. Yang, R. Piner, A. Velamakanni, I. Jung, E. Tutuc, S. K. Banerjee, L. Colombo, and R. S. Ruoff, Science **324**, 1312 (2009).

[16] S. Bae, H. Kim, Y. Lee, X. Xu, J.-S. Park, Y. Zheng, J. Balakrishnan, T. Lei, H. R. Kim, Y. I. Song, Y.-J. Kim, K. S. Kim, B. Özyilmaz, J.-H. Ahn, B. H. Hong, and S. Iijima, Nat. Nanotechnol. **5**, 574 (2010).

[17] A. C. Ferrari, F. Bonaccorso, V. Fal'ko, K. S. Novoselov, S. Roche, P. Bøggild, S. Borini, F. H. Koppens, V. Palermo, N. Pugno, *et al.*, Nanoscale **7**, 4598 (2015).

[18] A. Pant, Z. Mutlu, D. Wickramaratne, H. Cai, R. K. Lake, C. Ozkan, and S. Tongay, Nanoscale **8**, 3870 (2016).

[19] G. S. Duesberg, Nat. Mater. **13**, 1075 (2014).

[20] X. Duan, C. Wang, J. C. Shaw, R. Cheng, Y. Chen, H. Li, X. Wu, Y. Tang, Q. Zhang, A. Pan, J. Jiang, R. Yu, Y. Huang, and X. Duan, Nat. Nanotechnol. **9**, 1024 (2014).

[21] K. S. Novoselov, V. I. Fal'ko, L. Colombo, P. R. Gellert, M. G. Schwab, and K. Kim, Nature **490**, 192 (2012).

[22] K. V. Emtsev, A. Bostwick, K. Horn, J. Jobst, G. L. Kellogg, L. Ley, J. L. McChesney, T. Ohta, S. A. Reshanov, J. Röhrl, E. Rotenberg, A. K. Schmid, D. Waldmann, H. B. Weber, and T. Seyller, Nat. Mater. **8**, 203 (2009).

[23] W. A. de Heer, C. Berger, M. Ruan, M. Sprinkle, X. Li, Y. Hu, B. Zhang, J. Hankinson, and E. Conrad, Proc. Nat. Acad. Sci. **108**, 16900 (2011).

[24] A. Tzalenchuk, S. Lara-Avila, A. Kalaboukhov, S. Paolillo, M. Syväjärvi, R. Yakimova, O. Kazakova, T. J. B. M. Janssen, V. Fal'ko, and S. Kubatkin, Nat. Nanotechnol. **5**, 186 (2010).

[25] T. Yager, A. Lartsev, R. Yakimova, S. Lara-Avila, and S. Kubatkin, Carbon **87**, 409 (2015).

[26] T. J. B. M. Janssen, A. Tzalenchuk, R. Yakimova, S. Kubatkin, S. Lara-Avila, S. Kopylov, and V. I. Fal'ko, Phys. Rev. B **83**, 233402 (2011).

[27] W. A. de Heer, C. Berger, X. Wu, P. N. First, E. H. Conrad, X. Li, T. Li, M. Sprinkle, J. Hass, M. L. Sadowski, M. Potemskib, and G. Martinezb, Solid State Commun. **143**, 92 (2007).

[28] J. Hass, F. Varchon, J. E. Millán-Otoya, M. Sprinkle, N. Sharma, W. A. de Heer, C. Berger, P. N. First, L. Magaud, and E. H. Conrad, Phys. Rev. Lett. **100**, 125504 (2008).

[29] J. Hass, J. E. Millán-Otoya, P. N. First, and E. H. Conrad, Phys. Rev. B **78**, 205424 (2008).

[30] E. Pallecchi, F. Lafont, V. Cavaliere, F. Schopfer, D. Mailly, W. Poirier, and A. Ouerghi, Sci. Rep. **4**, 4558 (2014).

[31] S. Kopylov, A. Tzalenchuk, S. Kubatkin, and V. I. Fal'ko, Appl. Phys. Lett. **97**, 112109 (2010).

[32] J. A. Robinson, M. Hollander, M. LaBella III, K. A. Trumbull, R. Cavalero, and D. W. Snyder, Nano Lett. **11**, 3875 (2011).

[33] F. Speck, J. Jobst, F. Fromm, M. Ostler, D. Waldmann, M. Hundhausen, H. B. Weber, and T. Seyller, Appl. Phys. Lett. **99**, 122106 (2011).

[34] Y.-M. Lin, C. Dimitrakopoulos, K. A. Jenkins, D. B. Farmer, H.-Y. Chiu, A. Grill, and P. Avouris, Science **327**, 662 (2010).

[35] Y. Zhu, S. Murali, W. Cai, X. Li, J. W. Suk, J. R. Potts, and R. S. Ruoff, Adv. Mater. **22**, 3906 (2010).

[36] S. Stankovich, D. A. Dikin, R. D. Piner, K. A. Kohlhaas, A. Kleinhammes, Y. Jia, Y. Wu, S. T. Nguyen, and R. S. Ruoff, Carbon **45**, 1558 (2007).

[37] D. V. Kosynkin, A. L. Higginbotham, A. Sinitskii, J. R. Lomeda, A. Dimiev, B. K. Price, and J. M. Tour, Nature **458**, 872 (2009).

[38] L. Jiao, L. Zhang, X. Wang, G. Diankov, and H. Dai, Nature **458**, 877 (2009).

[39] S. Dhar, A. R. Barman, G. X. Ni, X. Wang, X. F. Xu, Y. Zheng, S. Tripathy, Ariando, A. Rusydi, K. P. Loh, M. Rubhausen, A. H. Castro Neto, B. Özyilmaz, and T. Venkatesan, AIP Adv. **1** (2011).

[40] K. R. Paton, E. Varrla, C. Backes, R. J. Smith, U. Khan, A. O'Neill, C. Boland, M. Lotya, O. M. Istrate, P. King, *et al.*, Nat. Mater. **13**, 624 (2014).

[41] M. Yi and Z. Shen, Carbon **78**, 622 (2014).

[42] E. Varrla, K. R. Paton, C. Backes, A. Harvey, R. J. Smith, J. McCauley, and J. N. Coleman, Nanoscale **6**, 11810 (2014).

[43] J. Shen, Y. He, J. Wu, C. Gao, K. Keyshar, X. Zhang, Y. Yang, M. Ye, R. Vajtai, J. Lou, and P. M. Ajayan, Nano Lett. **15**, 5449 (2015).

[44] A. Jawaid, D. Nepal, K. Park, M. Jespersen, A. Qualley, P. Mirau, L. F. Drummy, and R. A. Vaia, Chem. Mater. **28**, 337 (2016).

[45] J. T.-W. Wang, J. M. Ball, E. M. Barea, A. Abate, J. A. Alexander-Webber, J. Huang, M. Saliba, I. Mora-Sero, J. Bisquert, H. J. Snaith, and R. J. Nicholas, Nano Lett. **14**, 724 (2014).

[46] R. R. Nair, P. Blake, A. N. Grigorenko, K. S. Novoselov, T. J. Booth, T. Stauber, N. M. R. Peres, and A. K. Geim, Science **320**, 1308 (2008).

[47] A. Tiberj, N. Camara, P. Godignon, and J. Camassel, Nanoscale Res. Lett. **6**, 1 (2011).

[48] S. Roddaro, P. Pingue, V. Piazza, V. Pellegrini, and F. Beltram, Nano Lett. **7**, 2707 (2007).

[49] P. Blake, E. W. Hill, A. H. Castro Neto, K. S. Novoselov, D. Jiang, R. Yang, T. J. Booth, and A. K. Geim, Appl. Phys. Lett. **91**, 063124 (2007).

[50] T. Yager, A. Lartsev, S. Mahashabde, S. Charpentier, D. Davidovikj, A. Danilov, R. Yakimova, V. Panchal, O. Kazakova, A. Tzalenchuk, S. Lara-Avila, and S. Kubatkin, Nano Lett. **13**, 4217 (2013).

[51] R. S. Weatherup, B. C. Bayer, R. Blume, C. Ducati, C. Baehtz, R. Schlögl, and S. Hofmann, Nano Lett. **11**, 4154 (2011).

[52] L. Malard, M. Pimenta, G. Dresselhaus, and M. Dresselhaus, Phys. Rep. **473**, 51 (2009).

[53] A. C. Ferrari, Solid State Commun. **143**, 47 (2007).

[54] H. Li, Q. Zhang, C. C. R. Yap, B. K. Tay, T. H. T. Edwin, A. Olivier, and D. Baillargeat, Adv. Funct. Mater. **22**, 1385 (2012).

[55] A. L. Elías, N. Perea-López, A. Castro-Beltrán, A. Berkdemir, R. Lv, S. Feng, A. D. Long, T. Hayashi, Y. A. Kim, M. Endo, H. R. Gutiérrez, N. R. Pradhan, L. Balicas, T. E. Mallouk, F. López-Urías, H. Terrones, and M. Terrones, ACS Nano **7**, 5235 (2013).

[56] Y. Wang, Z. Ni, T. Yu, Z. X. Shen, H. Wang, Y. Wu, W. Chen, and A. T. S. Wee, J. Phys. Chem. C **112**, 10637 (2008).

[57] A. C. Ferrari, J. C. Meyer, V. Scardaci, C. Casiraghi, M. Lazzeri, F. Mauri, S. Piscanec, D. Jiang, K. S. Novoselov, S. Roth, and A. K. Geim, Phys. Rev. Lett. **97**, 187401 (2006).

[58] Y. Liu, Z. Liu, W. S. Lew, and Q. J. Wang, Nanoscale Res. Lett. **8**, 1 (2013).

[59] S. Lara-Avila, K. Moth-Poulsen, R. Yakimova, T. Bjørnholm, V. Fal'ko, A. Tzalenchuk, and S. Kubatkin, Adv. Mater. **23**, 878 (2011).

[60] A. Lartsev, T. Yager, T. Bergsten, A. Tzalenchuk, T. J. B. M. Janssen, R. Yakimova, S. Lara-Avila, and S. Kubatkin, Appl. Phys. Lett. **105**, 063106 (2014).

4

Physics of a Disordered Dirac Point in Epitaxial Graphene from Temperature-dependent Magnetotransport Measurements

This chapter reports a study of disorder effects on epitaxial graphene in the vicinity of the Dirac point by magnetotransport. Hall effect measurements show that the carrier density increases quadratically with temperature, in good agreement with theoretical predictions which take into account intrinsic thermal excitation combined with electron-hole puddles induced by charged impurities. The disorder strengths are deduced in the range $10.2 - 31.2$ meV, depending on the sample treatment. The scattering mechanisms are investigated and the impurity densities are estimated to be $3.0 - 9.1 \times 10^{10}$ cm^{-2} for the samples measured. A scattering asymmetry for electrons and holes is observed and is consistent with theoretical calculations for graphene on SiC substrates. It is also shown that the minimum conductivity increases with increasing disorder strength, in good agreement with quantum-mechanical numerical calculations.

The work in this chapter has been published in *Phys. Rev. B* **92**, 075407 (2015).

Contents

4.1 Introduction

Many of the exceptional electronic properties of graphene arise from its linear dispersion relation [1, 2] as introduced in Chapter 2. However, when the Fermi energy approaches the Dirac point, its properties can be dominated by the effects of disorder, which can be both intrinsic (such as ripples, topological lattice defects) and extrinsic (including cracks/voids, adatoms, charged impurities, etc.), in general varying from sample to sample [3]. Of particular significance are the effects of disorder potentials on electrical transport properties [4] due to the lack of screening at very low carrier densities. Microscopically, the fluctuating electrostatic potential can break up the intrinsically homogeneous charge distribution into electron-hole puddles (Figure 4.1) [5–9]. This effect is recognised to mainly originate from unintendedly introduced charged impurities, whose type, spatial distribution and density also depend on the sample environment, device fabrication techniques, and particularly graphene synthesis and treatment processes.

Recently, epitaxial graphene on SiC (SiC/G) has been reported to have very high quantum Hall breakdown current density [10] which potentially allows a quantum electrical resistance standard operating at even higher temperatures or/and lower magnetic

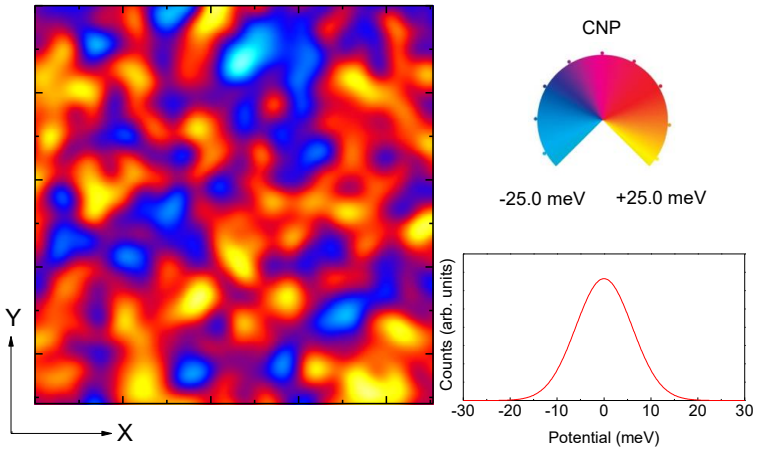

Figure 4.1: Spatially fluctuating electrostatic potentials with a Gaussian distribution showing the electron-hole puddles.

fields [11]. Low and well controlled carrier density is required to achieve high breakdown currents in these conditions, and understanding the disorder effects is therefore highly important. To date, there are very few experimental studies of disorder in epitaxial graphene grown on SiC, due to the intrinsically high level of doping from the substrate [12]. In this chapter, using extremely low carrier density epitaxial graphene, the role of disorder in governing the temperature dependent magnetotransport is described.

4.2 Methods and methodology

The samples used in this study were grown and fabricated by T. Yager, S. Lara-Avila, S. Kubatkin and R. Yakimova in Sweden, and provided to us by T. J. B. M. Janssen and A. Tzalenchuk from the National Physical Laboratory in the UK. The SiC/G samples were epitaxially grown on the Si-terminated face of 4H-SiC at $T = 2000$ °C and $P = 1$ atm Ar, as reported elsewhere [11, 13–15]. The as-grown samples have large uniform monolayer areas, where devices with an 8-leg Hall bar geometry of various sizes were fabricated using electron beam lithography followed by O_2 plasma etching and large-area

titanium-gold contacting. A non-volatile polymer gating technique was used to control the carrier density in epitaxial graphene by room-temperature UV illumination [16] or corona discharge [17] as introduced in Section 3.4.1. The polymer gates consist of bi-layer polymer coating on top of the graphene Hall bars, forming SiC/graphene/polymer heterostructures. The first layer is PMMA/MMA copolymer, followed by the second layer of UV sensitive polymer ZEP520A [16]. Both DC and AC magnetotransport measurements were carried out using an Oxford Instruments 21 T superconducting magnet with a variable temperature insert which allows temperature-dependent measurements from 1.4 up to 300 K.

Magnetotransport measurements were made on three SiC/G devices, which are denoted as CD1, CD2 and UV1. Two different techniques were used to reduce the relatively high initial electron density and tune the Fermi level to the vicinity of the Dirac point, where 4-probe resistance maxima were observed: CD1 and CD2 were treated with multiple negative ion projections onto the bilayer polymer gate, produced by corona discharge using a piezo-activated antistatic gun [17], resulting in extremely low final electron densities of 1.2 and 1.3 $\times$ 10^{10} cm^{-2}, respectively; UV1 was treated with deep UV illumination using a 248 nm mercury lamp [16] which eventually reduced the electron density to 8 $\times$ 10^{10} cm^{-2}. As will be shown below, these values should not be treated as the real electron densities, but merely are effective carrier densities, n_{eff}, calculated from the low-field Hall coefficients at 1.4 K assuming a homogeneous landscape with a single type of charge carriers. In the absence of disorder, these densities would correspond to an upper limit for the Fermi energy ($E_F = \hbar v_F \sqrt{\pi n_{eff}}$, where v_F is the Fermi velocity), which is between 12.7 meV and 32.9 meV, based on the assumption of a linear dispersion where the density of states vanishes at the Dirac point [18] (see Figure 2.6). In reality, due to the effects of disorder, a residual density of states and coexistence of electrons and holes [6] at $E_F \to 0$ are expected, thus, the determination of an extremely low Fermi energy from Hall effect measurements becomes non-trivial. The overall net charge den-

sity is much lower than n_{eff}, but differences in the mobilities of the two carrier types still create a finite Hall coefficient at the Dirac point which corresponds to the resistivity maximum studied here.

4.3 Results and discussions

4.3.1 Intrinsic excitation in the presence of electron-hole puddles

Figure 4.2 presents typical experimental results: the Hall resistance R_{xy} and the longitudinal resistance R_{xx} of sample CD2 as a function of magnetic field at temperatures from 1.4 to 300 K. In this study, all three devices show similar behaviour as shown in Figure 4.2. Due to the extremely low carrier densities of the samples, quantum Hall plateaux corresponding to the filling factor $\nu = 2$ can be observed already from about 0.6 T at 1.4 K. The Hall resistance becomes significantly non-linear when approaching the quantum Hall regime. Therefore, to extract the zero-field carrier densities of the measured devices, only Hall coefficients between -0.1 T and $+0.1$ T are used.

It has been theoretically studied and experimentally confirmed that, close to the Dirac point, as a consequence of disorder, the carrier density landscape is extremely inhomogeneous and electron-hole puddles are formed [4–9]. Classically, the low-field Hall coefficient in the presence of both electrons and holes is given by,

$$R_H \equiv \frac{E_y}{J_x B} = -\frac{1}{e}\frac{n_e\mu_e^2 - n_h\mu_h^2}{(n_e\mu_e + n_h\mu_h)^2}, \tag{4.1}$$

where n_e (n_h) and μ_e (μ_h) are the electron (hole) density and mobility, respectively. Similar two-carrier analyses are also found in the literature for this electron-hole coexistence regime in monolayer and bilayer graphene [19, 20]. The carrier density directly

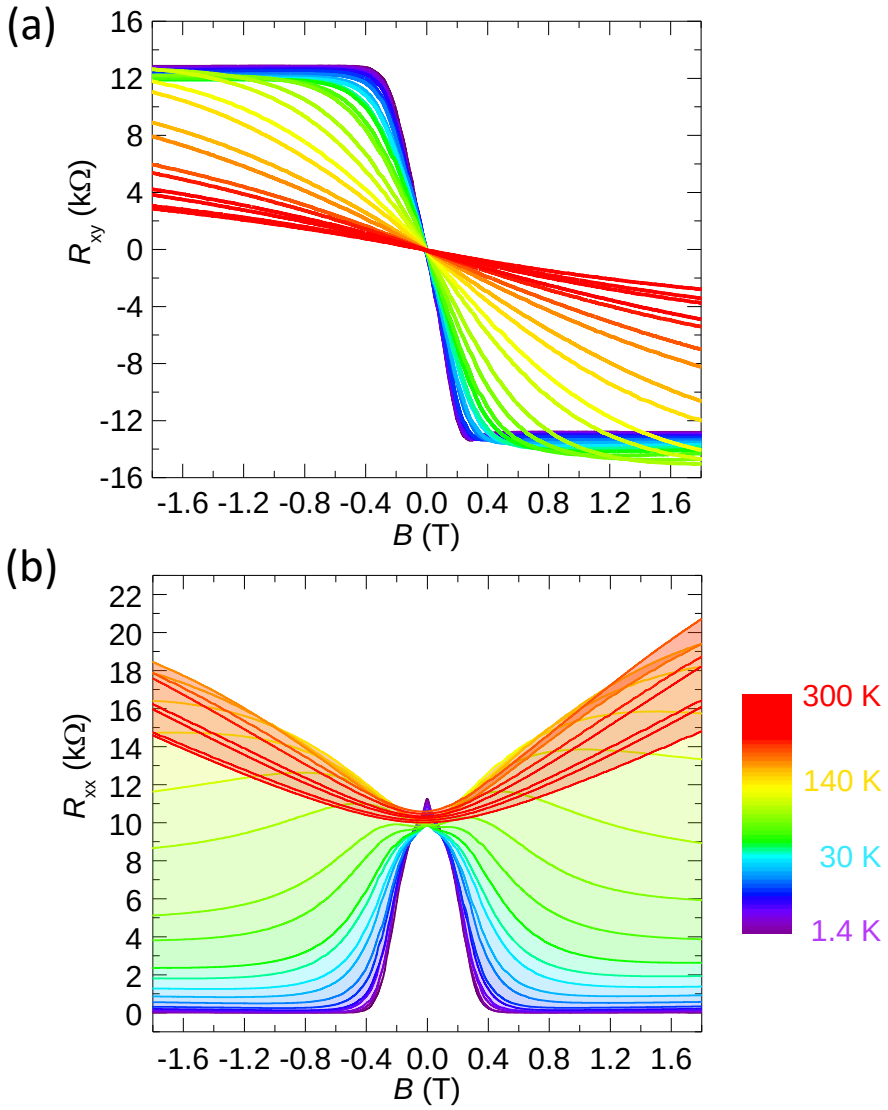

Figure 4.2: The Hall resistance R_{xy} and the longitudinal resistance R_{xx} as a function of magnetic field at temperatures from 1.4 to 300 K for sample CD2. This sample enters the quantum Hall regime already from about 0.6 T as observed from the quantised R_{xy} and the vanishing R_{xx} at low temperatures.

extracted from this two-carrier low-field Hall effect is therefore effectively,

$$n_{eff} = \frac{(n_e\mu_e + n_h\mu_h)^2}{n_e\mu_e^2 - n_h\mu_h^2}. \tag{4.2}$$

When the Fermi energy is zero, i.e. at charge neutrality point (CNP), $n_e = n_h > 0$.

Thus, $n_{eff} = \alpha n_e$, where $\alpha = \frac{\frac{\mu_e}{\mu_h}+1}{\frac{\mu_e}{\mu_h}-1}$. Notably, for electron-like behaviour ($R_H < 0$), $\alpha > 0$; for hole-like behaviour ($R_H > 0$), $\alpha < 0$.

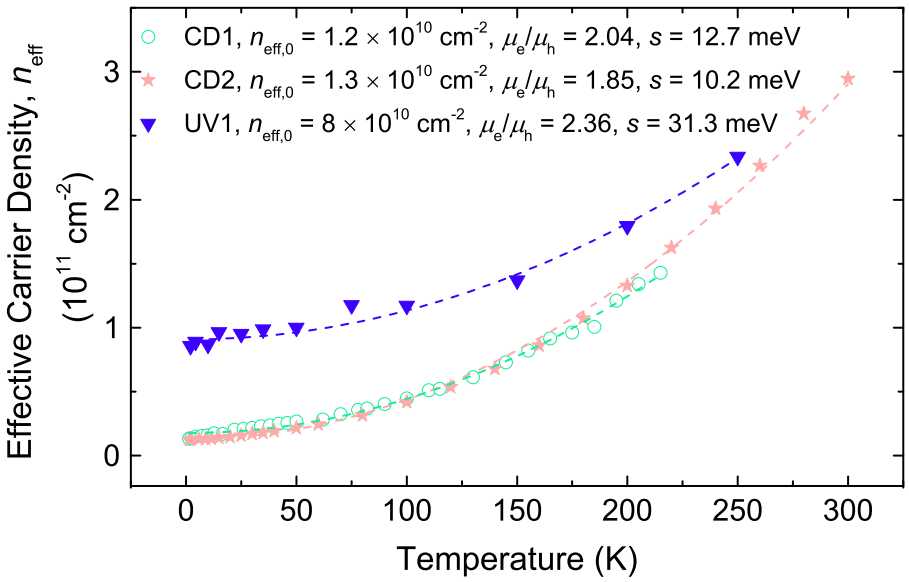

Figure 4.3: Temperature dependence of the effective carrier densities n_{eff} deduced using Equations 4.1 and 4.2 for sample CD1, CD2 and UV1. Quadratic increase with increasing temperature is observed, as well as non-vanishing carrier densities $n_{eff,0}$ at $T \to 0$ K. The experimental data is well fitted using Equations 4.4 and 4.5 as shown in the figure (dash lines), where the disorder strength s and the mobility ratio μ_e/μ_h are extracted from the fitting.

We now analyse the temperature dependence of the effective carrier density n_{eff} as shown in Figure 4.3 for the three devices. A quadratic increase of n_{eff} with increasing temperature can be clearly observed for all of the samples. Each sample also exhibits a distinct non-zero residual charge density at the low temperature limit even when $E_F \to 0$, indicating that the potential landscape of these devices is highly inhomogeneous. These features are clearly different from the Arrhenius behaviour of conventional semiconductors and intrinsic thermal activation in graphene when no disorder effects are accounted for (i.e., there is no residual carrier density). Accurate fitting can be made based on the theory [4] assuming that the electronic potential energy of disordered graphene follows Gaussian statistics, which give the probability of finding the

local potential within a range dV about V,

$$P(V)dV = \frac{1}{\sqrt{2\pi s^2}} e^{-\frac{V^2}{2s^2}} dV, \tag{4.3}$$

where s is a parameter used to characterise the strength of the potential fluctuations. As a consequence, the temperature-dependent charge density at CNP for both electrons and holes are [4],

$$n_e(T) = n_h(T) = \frac{g_s g_v}{2\pi(\hbar v_F)^2} \left[\frac{s^2}{4} + \frac{(\pi k_B T)^2}{12} \right], \tag{4.4}$$

where $g_s = g_v = 2$ are the spin and valley degeneracies, and $v_F \approx 10^6$ m/s is the Fermi velocity. The temperature dependence of the effective carrier density is therefore,

$$n_{eff}(T) = \alpha \cdot n_e(T), \tag{4.5}$$

where α is assumed to be constant over the temperature range under consideration. The predicted temperature dependence from Equations 4.4 and 4.5 fits the experimental data very well (Figure 4.3), giving potential fluctuation strengths s = 12.7, 10.2 and 31.3 meV, and pre-factors α which translate into mobility ratios of electrons to holes μ_e/μ_h = 2.04, 1.85 and 2.36, for the devices CD1, CD2 and UV1 respectively. Table 4.1 shows comparisons of the potential fluctuations due to electron-hole puddles, between the values deduced from our magnetotransport measurements and those found in the literature [5–9], where most of the characterisation methods are STM-based.

Table 4.1 also includes the disorder strength (15 ± 1 meV) from our analysis of the published data by Yager *et al.* [21] for SiC/G samples exposed to aqueous-ozone (AO) processing, which results in high mobility and extremely low p-type doping with an effective carrier density $n_{eff,0} = -4.0 \times 10^{10}$ cm^{-2} (negative sign for hole-like behaviour) from Hall measurements. It is found that the disorder strengths measured in our samples

Table 4.1: Energy fluctuations of electron-hole puddles in graphene. (Results of our analysis of magnetotransport data are highlighted in bold. KPM: Kelvin probe microscopy; SET: single-electron transistor; STM: scanning tunnelling microscopy; STS: scanning tunnelling spectroscopy; CVD: chemical vapour deposition.)

Synthesis (Treatment)	Disorder Strength (s)	Probing Method
Epitaxial on SiC (**CD1**)	**12.7 ± 0.6 meV**	**Magnetotransport**
Epitaxial on SiC (**CD2**)	**10.2 ± 0.4 meV**	**Magnetotransport**
Epitaxial on SiC (**UV1**)	**31.3 ± 2.0 meV**	**Magnetotransport**
Epitaxial on SiC (**AO**)	**15 ± 1 meV**	**Magnetotransport**
Epitaxial on SiC	12 meV	KPM [5]
Exfoliated on SiO_2/Si	50 meV	SET [6]
Exfoliated on SiO_2/Si	$\sim$ 20 meV	STM [7]
Exfoliated on h-BN	5.4 meV	STM [8]
CVD on Ir(111)	$\sim$ 30 meV	STM/STS [9]

are consistent with those reported previously for SiC/G, and are smaller than those of CVD and exfoliated samples on SiO_2, while they are slightly larger than that of exfoliated graphene on h-BN, which is an atomically smooth, dangling bonds free and lattice-matched substrate to support high quality graphene [22]. These comparisons suggest that SiC/G generally has very good quality and relatively small amounts of disorder, even though the actual characteristics are expected to vary from sample to sample and may also be sensitive to the sample treatment as seen from Table 4.1. At the same time, it is demonstrated that magnetotransport measurement is an additional effective method to investigate the disorder effects and characteristics in graphene.

4.3.2 Scattering mechanisms

To evaluate the scattering mechanisms in the SiC/G samples, we now turn to examine the temperature dependence of the longitudinal conductivity σ_{xx} and the electron mobility as shown in Figures 4.4 and 4.5.

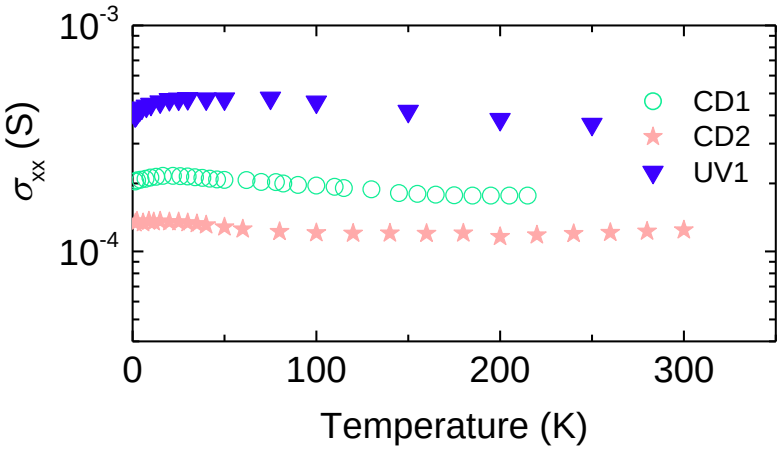

Figure 4.4: The longitudinal conductivity as a function of temperature, where weak non-monotonic dependences are shown.

Carrier mobilities of individual species are calculated classically based on,

$$\sigma_{xx} = e\left(n_e\mu_e + n_h\mu_h\right) = \frac{en_{eff}}{\alpha}\left(\mu_e + \mu_h\right), \tag{4.6}$$

via Equation 4.5 and the value $\frac{\mu_e}{\mu_h}$ deduced from α. It is observed that $\sigma_{xx}(T)$ remains slowly varying with weak non-monotonic fluctuations for a large range of temperatures. Similar behaviour has been reported for monolayer graphene samples when $E_F \approx 0$ [23, 24], and this is clearly different from thermally activated conductivity in conventional gapped semiconductors and from phonon-limited behaviour in graphene, which will result in a T^{-4} or T^{-1} dependence [25, 26] at low or high temperatures respectively due to intravalley acoustic phonon scattering. It should be pointed out that this temperature dependence of conductivity in our extremely low carrier density samples could be a combination of various contributions. It is believed that this weakly varying conductivity is mainly due to the temperature-dependent carrier density as described above and the $\mu(T)$ dependence as will be discussed below. At the lowest temperatures there are also temperature dependent weak localisation corrections, which can be seen from Figure 4.2b around $B = 0$ T but have been excluded in Figure 4.4.

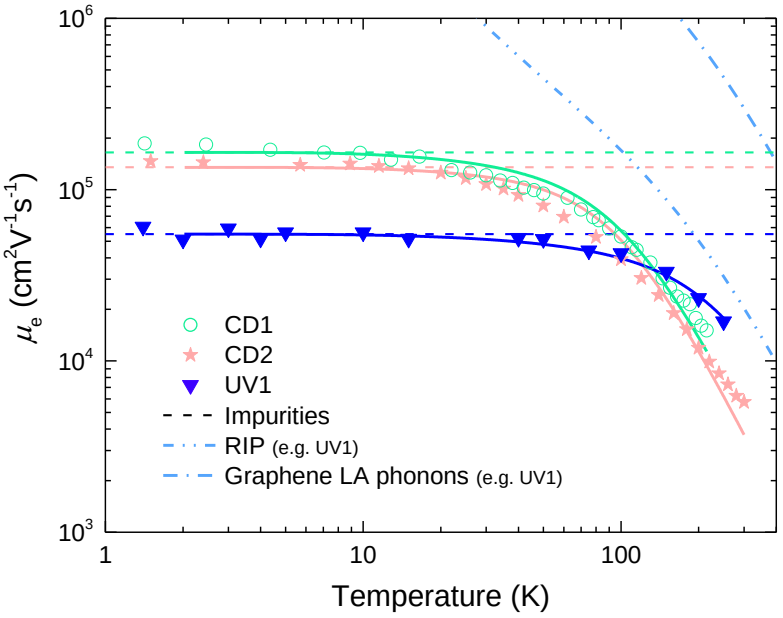

Figure 4.5: The temperature dependence of the electron mobility of our samples. Individual contributions due to impurity scattering (green/pink/blue dash lines) for all three samples, LA phonon scattering (blue dash-dot line), RIP scattering (blue dash-dot-dot line) for UV1 as an example are shown. The solid lines represent the overall $\mu_e(T)$ dependence by fitting the experimental data.

Figure 4.5 shows the electron mobility as a function of temperature, as well as the mobility limits as a result of various scattering mechanisms, including impurity scattering, scattering by longitudinal acoustic (LA) phonons in graphene, and also by remote interfacial phonons (RIP) at the SiC/graphene interface [27, 28]. In the case of charged impurities, carrier mobility is inversely proportional to the impurity density n_{imp} [18, 29],

$$\mu_{imp} \approx \frac{C_0}{n_{imp}}, \tag{4.7}$$

where C_0 is a constant. For LA phonon scattering [25],

$$\mu_{LA} = \frac{e\hbar\rho_s v_s^2 v_F^2}{\pi n_e D_A^2 k_B T}, \tag{4.8}$$

with $\rho_s = 7.6 \times 10^{-7}$ kg/m^2 the two-dimensional mass density, $v_s = 1.7 \times 10^4$ m/s the

sound velocity, and $D_A = 18$ eV the acoustic deformation potential. The RIP limited mobility is given by [27, 28],

$$\mu_{RIP} = \frac{1}{n_e e}\left\{\sum_i \left[\frac{C_i}{\exp\left(\frac{E_i}{k_B T}\right) - 1}\right]\right\}^{-1}, \tag{4.9}$$

where C_i and E_i are electron-phonon coupling constants and phonon energies of the phonon modes under consideration. To fit the data, three phonon modes were first considered: two out-of-plane acoustic phonon modes in epitaxial graphene ($E_1 = 70$ meV and $E_2 = 16$ meV) [27, 30] and a surface phonon mode of 4H-SiC ($E_3 = 117$ meV) [27, 28, 31]. However, due to their relatively large phonon energies, none of these can yield a reasonable fit, which can only be obtained (Figure 4.5 solid lines) when an additional low-energy phonon mode ($E_4 \approx 2$ meV) is introduced. This is consistent with the previously reported results [27, 28, 32, 33], and this low-frequency remote phonon mode has been recognised to originate from the interaction between graphene and the buffer layer, that they are oscillating out-of-phase parallel to each other.

It can be seen from Figure 4.5 that charged impurity scattering plays the most dominant role at low temperatures (< 100 K), while the high-temperature mobility is probably limited by RIP scattering, since LA phonons make only a small contribution to the overall mobility for temperatures below 400 K. Using $C_0 \approx 5 \times 10^{15}$ $V^{-1}s^{-1}$ [29], the densities of charged impurities for our SiC/G samples are estimated to be $3.0 - 9.1 \times 10^{10}$ cm^{-2}, which are $1 - 2$ orders of magnitude lower than that in typical exfoliated [34] and CVD grown [35, 36] graphene on SiO_2, but are comparable to that of h-BN supported graphene [37], consistent with its high charge carrier mobility. Even though the above analysis has been restricted to phonon and impurity scattering, other possible scattering mechanisms may exist, such as scattering due to ripples [38, 39] and very large defects [40]. Quantitative analysis of these mechanisms on our devices is rather difficult since systematic examination of the sample morphology is required and,

on the other hand, the corresponding theoretical pictures are rather complicated and still contentious [41].

So far we have been able to identify that charge carrier scattering at low temperatures in the SiC/G is mainly due to charged impurities, in the classical regime where quantum corrections are suppressed by magnetic fields. It is these impurities which provide the same origin for generating the electron-hole puddles at $E_F \to 0$. Furthermore, these impurities are most likely to be charged/Coulomb impurities rather than short-range impurities. The main evidence for this is the presence of unequal electron and hole mobilities, which is a consequence of the unbalanced scattering cross sections for charged scatterers in a system with 2D relativistic dispersion [29, 42]. This theory can be intuitively understood from the idea that in such system an attractive potential scatters a charge carrier more effectively than a repulsive potential [42]. As presented in Figure 4.3, similar μ_e/μ_h in the range of $1.85 - 2.36$ are obtained. According to the theory [42], assuming a single species of monovalent ($|Z| = 1$) impurities, the above mobility ratios can be translated into a dimensionless asymmetry factor $c = 0.30 - 0.39$, which is used to characterise the strength of this asymmetry effect (i.e. $c = 0$ for $\mu_e = \mu_h$ and $c \to 1$ for $\mu_{e(h)} \gg \mu_{h(e)}$). The nature of this asymmetry factor depends on the dielectric constant of the substrate: for SiO_2, $c|_{\epsilon_r=3.9} \approx 0.46$; for SiC, the same substrates as used in our devices, $c|_{\epsilon_r=10.0} \approx 0.32$, which is in very good agreement with our experimental results. Small variations around the predicted value are expected, since the actual electrostatic environment of each SiC/G sample could also be affected by the polymer top-gate dielectrics, meanwhile, the types and amounts of charged impurities present in the samples could be more complex.

4.3.3 Minimum conductivity of disordered graphene

Finally, the effects of disorder potential fluctuations on the low-temperature non-vanishing minimum conductivity (σ_{min}) at the Dirac point are investigated for graphene in the diffusive transport regime. This property has been extensively considered theoretically and the two main existing approaches lead to contradictory results [43]. The semiclassical Boltzmann transport theory predicts a decreasing σ_{min} with increasing disorder strength. With a self-consistent modification to the Boltzmann theory, a subsequent increase of the minimum conductivity for higher disorder strengths is predicted. On the other hand, the minimum conductivity treated quantum-mechanically [43–46] is increased for the entire disorder strength range for a non-interacting model using a Gaussian correlated disorder potential. Experimentally, very few studies can be found addressing this problem in the literature [29]. Shown in Figure 4.6 is the minimum conductivity (at $B = 0$) as a function of the disorder strength s obtained from our measurements when quantum corrections have been taken into account, as well as theoretical predictions including the numerical calculation via the quantum mechanical approach by Adam *et al.* [43], and results from the (self-consistent) Boltzmann theories, for $L = 50\xi$, where L is the sample length, ξ is the correlation length of the assumed random Gaussian potential $U(\boldsymbol{r})$ in the system and the dimensionless parameter $K_0 \propto \langle U(\boldsymbol{r})U(\boldsymbol{r}')\rangle$ is the disorder strength used in the theories.

The above experimental results show that the minimum conductivity increases with increasing s, roughly following a $\beta(s-\Delta)^{\frac{1}{2}}$ dependence locally in the $(0.5-2.5)\times\frac{4e^2}{h}$ range, highlighted by the green dash-dot line in the figure, where β and Δ are constants. This increase agrees qualitatively well with the theoretical predictions [43] from the quantum-mechanical approach, where we assume $s \propto \sqrt{K_0}$. However, our data do not agree with the results from the Boltzmann and the self-consistent Boltzmann theory as shown in the figure. In addition, it is noted that the minimum conductivity may have

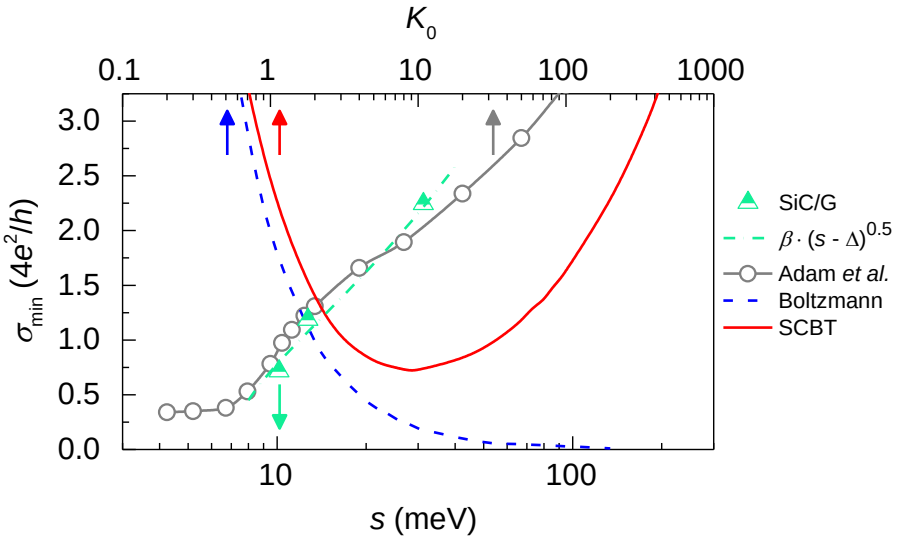

Figure 4.6: σ_{min} as a function of disorder strength. A $\beta(s-\Delta)^{\frac{1}{2}}$ dependence (green dash-dot line) is observed from our experimental data (green triangles). σ_{min} as a function of K_0 from numerical calculations by Adam *et al.* (grey circles and solid line), as well as predictions using the Boltzmann (blue dash line) and the self-consistent Boltzmann (red solid line) theories are also shown [43].

a complex dependence on the sample length and details of quantum interference effects [43, 47, 48], and also be a function of the charged impurity density n_{imp} indicated from previous experimental work by Chen *et al.* [29], whose results suggest that σ_{min} drops with increasing n_{imp} at low impurity densities and may saturate rapidly. To allow a more conclusive interpretation, however, more experimental data and systematic comparisons between well-controlled samples from different synthesis methods and a larger range of disorder potentials and impurity densities would be needed.

4.4 Summary

In summary, this chapter has presented temperature dependent magnetotransport measurements on epitaxial graphene. The disorder effects when the Fermi energy lies in the vicinity of the Dirac point are demonstrated, and the main origin of those effects

has been identified to be charged impurities. The disorder strength and the impurity densities of the samples measured have been estimated from experimental results. It is also shown that the minimum conductivity increases with increasing disorder strength, in good agreement with numerical quantum-mechanical calculations. Overall, the application of this method can, therefore, provide an alternative and effective route for quantitatively studying the disorder characteristics in graphene and possibly in other two-dimensional materials.

Bibliography

[1] P. R. Wallace, Phys. Rev. **71**, 622 (1947).

[2] K. S. Novoselov, A. K. Geim, S. V. Morozov, D. Jiang, M. I. Katsnelson, I. V. Grigorieva, S. V. Dubonos, and A. A. Firsov, Nature **438**, 197 (2005).

[3] A. H. Castro Neto, F. Guinea, N. M. R. Peres, K. S. Novoselov, and A. K. Geim, Rev. Mod. Phys. **81**, 109 (2009).

[4] Q. Li, E. H. Hwang, and S. Das Sarma, Phys. Rev. B **84**, 115442 (2011).

[5] A. E. Curtin, M. S. Fuhrer, J. L. Tedesco, R. L. Myers-Ward, C. R. Eddy Jr., and D. K. Gaskill, Appl. Phys. Lett. **98**, 243111 (2011).

[6] J. Martin, N. Akerman, G. Ulbricht, T. Lohmann, J. H. Smet, K. Von Klitzing, and A. Yacoby, Nat. Phys. **4**, 144 (2008).

[7] Y. Zhang, V. W. Brar, C. Girit, A. Zettl, and M. F. Crommie, Nat. Phys. **5**, 722 (2009).

[8] J. Xue, J. Sanchez-Yamagishi, D. Bulmash, P. Jacquod, A. Deshpande, K. Watanabe, T. Taniguchi, P. Jarillo-Herrero, and B. J. LeRoy, Nat. Mater. **10**, 282 (2011).

[9] S. C. Martin, S. Samaddar, B. Sacépé, A. Kimouche, J. Coraux, F. Fuchs, B. Grévin, H. Courtois, and C. B. Winkelmann, Phys. Rev. B **91**, 041406 (2015).

[10] J. A. Alexander-Webber, A. M. R. Baker, T. J. B. M. Janssen, A. Tzalenchuk, S. Lara-Avila, S. Kubatkin, R. Yakimova, B. A. Piot, D. K. Maude, and R. J. Nicholas, Phys. Rev. Lett. **111**, 096601 (2013).

[11] A. Tzalenchuk, S. Lara-Avila, A. Kalaboukhov, S. Paolillo, M. Syväjärvi, R. Yakimova, O. Kazakova, T. J. B. M. Janssen, V. Fal'ko, and S. Kubatkin, Nat. Nanotechnol. **5**, 186 (2010).

[12] C. Riedl, C. Coletti, and U. Starke, J. Phys. D: Appl. Phys. **43**, 374009 (2010).

[13] T. Yager, A. Lartsev, S. Mahashabde, S. Charpentier, D. Davidovikj, A. Danilov, R. Yakimova, V. Panchal, O. Kazakova, A. Tzalenchuk, S. Lara-Avila, and S. Kubatkin, Nano Lett. **13**, 4217 (2013).

[14] T. J. B. M. Janssen, A. Tzalenchuk, R. Yakimova, S. Kubatkin, S. Lara-Avila, S. Kopylov, and V. I. Fal'ko, Phys. Rev. B **83**, 233402 (2011).

[15] T. Yager, A. Lartsev, R. Yakimova, S. Lara-Avila, and S. Kubatkin, Carbon **87**, 409 (2015).

[16] S. Lara-Avila, K. Moth-Poulsen, R. Yakimova, T. Bjørnholm, V. Fal'ko, A. Tzalenchuk, and S. Kubatkin, Adv. Mater. **23**, 878 (2011).

[17] A. Lartsev, T. Yager, T. Bergsten, A. Tzalenchuk, T. J. B. M. Janssen, R. Yakimova, S. Lara-Avila, and S. Kubatkin, Appl. Phys. Lett. **105**, 063106 (2014).

[18] E. H. Hwang, S. Adam, and S. Das Sarma, Phys. Rev. Lett. **98**, 186806 (2007).

[19] S. Wiedmann, H. J. van Elferen, E. V. Kurganova, M. I. Katsnelson, A. J. M. Giesbers, A. Veligura, B. J. van Wees, R. V. Gorbachev, K. S. Novoselov, J. C. Maan, and U. Zeitler, Phys. Rev. B **84**, 115314 (2011).

[20] E. V. Kurganova, S. Wiedmann, A. J. M. Giesbers, R. V. Gorbachev, K. S. Novoselov, M. I. Katsnelson, T. Tudorovskiy, J. C. Maan, and U. Zeitler, Phys. Rev. B **87**, 085447 (2013).

[21] T. Yager, M. J. Webb, H. Grennberg, R. Yakimova, S. Lara-Avila, and S. Kubatkin, Appl. Phys. Lett. **106**, 063503 (2015).

[22] C. R. Dean, A. F. Young, I. Meric, C. Lee, L. Wang, S. Sorgenfrei, K. Watanabe, T. Taniguchi, P. Kim, K. L. Shepard, and J. Hone, Nat. Nanotechnol. **5**, 722 (2010).

[23] K. I. Bolotin, K. J. Sikes, J. Hone, H. L. Stormer, and P. Kim, Phys. Rev. Lett. **101**, 096802 (2008).

[24] S. V. Morozov, K. S. Novoselov, M. I. Katsnelson, F. Schedin, D. C. Elias, J. A. Jaszczak, and A. K. Geim, Phys. Rev. Lett. **100**, 016602 (2008).

[25] E. H. Hwang and S. Das Sarma, Phys. Rev. B **77**, 115449 (2008).

[26] T. Stauber, N. M. R. Peres, and F. Guinea, Phys. Rev. B **76**, 205423 (2007).

[27] A. J. M. Giesbers, P. Procházka, and C. F. J. Flipse, Phys. Rev. B **87**, 195405 (2013).

[28] S. Tanabe, Y. Sekine, H. Kageshima, M. Nagase, and H. Hibino, Phys. Rev. B **84**, 115458 (2011).

[29] J.-H. Chen, C. Jang, S. Adam, M. S. Fuhrer, E. D. Williams, and M. Ishigami, Nat. Phys. **4**, 377 (2008).

[30] J. Červenka, K. van de Ruit, and C. F. J. Flipse, Phys. Status Solidi B **247**, 2992 (2010).

[31] H. Nienhaus, T. U. Kampen, and W. Mönch, Surf. Sci. Lett. **324**, L328 (1995).

[32] C. Yu, J. Li, Q. B. Liu, S. B. Dun, Z. Z. He, X. W. Zhang, S. J. Cai, and Z. H. Feng, Appl. Phys. Lett. **102**, 013107 (2013).

[33] N. Ray, S. Shallcross, S. Hensel, and O. Pankratov, Phys. Rev. B **86**, 125426 (2012).

[34] Y.-W. Tan, Y. Zhang, K. Bolotin, Y. Zhao, S. Adam, E. H. Hwang, S. Das Sarma, H. L. Stormer, and P. Kim, Phys. Rev. Lett. **99**, 246803 (2007).

[35] J. Lee, L. Tao, Y. Hao, R. S. Ruoff, and D. Akinwande, Appl. Phys. Lett. **100**, 152104 (2012).

[36] J. Chan, A. Venugopal, A. Pirkle, S. McDonnell, D. Hinojos, C. W. Magnuson, R. S. Ruoff, L. Colombo, R. M. Wallace, and E. M. Vogel, ACS Nano **6**, 3224 (2012).

[37] K. M. Burson, W. G. Cullen, S. Adam, C. R. Dean, K. Watanabe, T. Taniguchi, P. Kim, and M. S. Fuhrer, Nano Lett. **13**, 3576 (2013).

[38] F. Guinea, J. Low Temp. Phys. **153**, 359 (2008).

[39] M. I. Katsnelson and A. K. Geim, Phil. Trans. R. Soc. A **366**, 195 (2008).

[40] J.-H. Chen, W. G. Cullen, C. Jang, M. S. Fuhrer, and E. D. Williams, Phys. Rev. Lett. **102**, 236805 (2009).

[41] S. Das Sarma, S. Adam, E. H. Hwang, and E. Rossi, Rev. Mod. Phys. **83**, 407 (2011).

[42] D. S. Novikov, Appl. Phys. Lett. **91**, 102102 (2007).

[43] S. Adam, P. W. Brouwer, and S. Das Sarma, Phys. Rev. B **79**, 201404 (2009).

[44] H. Suzuura and T. Ando, Phys. Rev. Lett. **89**, 266603 (2002).

[45] A. Schuessler, P. M. Ostrovsky, I. V. Gornyi, and A. D. Mirlin, Phys. Rev. B **79**, 075405 (2009).

[46] J. Tworzydło, C. W. Groth, and C. W. J. Beenakker, Phys. Rev. B **78**, 235438 (2008).

[47] F. Ortmann, A. Cresti, G. Montambaux, and S. Roche, Europhys. Lett. **94**, 47006 (2011).

[48] N. Leconte, A. Lherbier, F. Varchon, P. Ordejon, S. Roche, and J.-C. Charlier, Phys. Rev. B **84**, 235420 (2011).

5

Giant Quantum Hall Plateaus Generated by Charge Transfer in Epitaxial Graphene

Epitaxial graphene has proven itself to be the best candidate for quantum electrical resistance standards due to its wide quantum Hall plateaus with exceptionally high breakdown currents. However one key underlying mechanism, a magnetic field dependent charge transfer process, is yet to be fully understood. This chapter reports measurements of the quantum Hall effect in epitaxial graphene showing the widest quantum Hall plateau observed to date extending over 50 T, attributed to an almost linear increase in carrier density with magnetic field. This behaviour is strong evidence for field dependent charge transfer from charge reservoirs with exceptionally high densities of states in close proximity to the graphene. Using a realistic framework of broadened Landau levels, the densities of donor states are modelled and the field dependence of charge transfer is predicted in excellent agreement with experimental results, thus providing a guide towards engineering epitaxial graphene for applications such as quantum metrology.

The work in this chapter has been published in *Sci. Rep.* **6**, 30296 (2016).

Contents

5.1 Introduction

The quantum Hall effect [1], defined by a vanishing longitudinal resistivity ($\rho_{xx} = 0$) and a quantised Hall resistance ($\rho_{xy} = h/\nu e^2$) for ν = integer, has long been used in metrology as a quantum electrical resistance standard [2]. However, the traditional quantum resistance standard, based on GaAs, requires very low temperatures and high magnetic fields to achieve suitable levels of precision. Recently it has been shown that graphene, grown epitaxially on SiC, can maintain the $\nu = 2$ quantum Hall state up to critical current densities j_c more than a factor of 30 times larger than previously observed in other material systems [3]. Furthermore, these high values of j_c were also observed to persist up to significantly higher critical temperatures T_c when compared to GaAs for a given magnetic field [4], making epitaxial graphene the best candidate to date for the next generation of quantum resistance metrology applications [5–7]. This improved performance of graphene is in part due to its large cyclotron energy gaps arising from the high electron velocity at the Dirac point [8], and is also due to the

high electron-phonon energy relaxation rates, an order of magnitude faster than those in GaAs heterostructures, which play an important role in determining the high current breakdown of the QHE [9, 10].

In epitaxial graphene grown on the Si-terminated face of SiC, charge transfer from the underlying substrate to the graphene leads to a strongly magnetic field dependent carrier density and an exceptionally wide $\nu = 2$ QH plateau [11, 12]. The mechanisms which underlie this behaviour need to be fully understood if epitaxial graphene is to live up to its metrological potential. However, due to this charge transfer process and the high magnetic fields to which $\nu = 2$ is extended it is very difficult to experimentally observe the full extent of the $\nu = 2$ plateau [3, 6, 12–21]. Initial theoretical descriptions of this phenomenon are based on charge transfer from the underlying substrate, due to the large impact of the quantum capacitance in the system, into the $N = 0$ Landau level in graphene which has fixed zero energy independent of magnetic field [11, 12]. These predict a linear magnetic field dependence of the carrier density n in the $\nu = 2$ plateau such that the $N = 0$ Landau level remains exactly filled over a large range of magnetic fields, resulting in the exceptionally wide plateau and high critical current densities. In these models the linear magnetic field dependence of n is predicted to saturate at high magnetic fields. However, further work has suggested that the carrier density continues to increase when the magnetic field is further increased [3]. The assumptions made in early theoretical models include unbroadened δ-function Landau levels in graphene and constant densities of states within the charge reservoirs. Experimental data in which the full extent of the magnetic field dependence can be measured is therefore crucial in obtaining a comprehensive understanding of this charge transfer process which underpins the benefits of graphene in quantum metrology applications.

Using a combination of pulsed magnetic fields up to 57 T and samples with ultra-low carrier densities this chapter presents the first detailed study of the full magnetic field dependence of charge transfer in epitaxial graphene through a $\nu = 2$ plateau which

remarkably extends from $B = 3$ T to over 50 T. Using an occupancy dependence of the quantum Hall breakdown current, it is demonstrated that the carrier density increases almost linearly with B throughout the $\nu = 2$ plateau. This method is validated by a fit to the temperature dependence of the magneto-conductivity which provides a direct measure of the position of the Fermi energy with respect to the nearest ($N = 0$) Landau level and hence provides an independent measure of the carrier density. It is also demonstrated that by extending the existing models [11, 12, 16] for the field dependent charge transfer under the framework of broadened Landau levels, together with a proposed expression for the field dependent carrier density, a better understanding of the charge transfer process and its effects on the breakdown of the quantum Hall effect in epitaxial graphene grown on SiC is obtained.

5.2 Methods

The samples used in this study were grown and fabricated by T. Yager, S. Lara-Avila, S. Kubatkin and R. Yakimova in Sweden, and provided to us by T. J. B. M. Janssen and A. Tzalenchuk from the National Physical Laboratory in the UK. The devices studied were prepared from epitaxially grown graphene on the Si-terminated face of SiC. Each device was patterned using electron beam lithography and oxygen plasma etching into an eight-leg Hall bar geometry with a width $W = 20$ μm and length $L = 20$ μm. Electrical contacting was made using large area electron beam evaporated Ti and Au. The same non-volatile dual-polymer gating technique as described in Section 3.4.1 using PMMA/MMA and ZEP520A was also applied to tune the carrier density in the epitaxial graphene using a combination of UV illumination [20] and corona discharge [21] at room temperature. Measurements using pulsed magnetic fields of up to 57 T provided by a 19 kV long pulse magnet at the LNCMI-Toulouse were performed by my colleague Jack A. Alexander-Webber, and continuous field measurements were taken in

an Oxford Instruments superconducting solenoid magnet. Measurements were taken at a fixed temperature of $T = 2$ K unless otherwise stated.

5.3 Results and discussions

5.3.1 Breakdown of the quantum Hall effect in ultra-low carrier density epitaxial graphene

We begin with the sample having its lowest Fermi level, where the zero field electron density is 1.5×10^{10} cm^{-2}, as determined from the low field Hall coefficient ($\frac{\mathrm{d}\rho_{xy}}{\mathrm{d}B} = \frac{1}{ne}$). In this state the $\nu = 2$ quantum Hall state is observed to begin well below 1 T and the longitudinal resistivity, R_{xx} is undetectably small from 0.7 up to 14 T, as shown in Figure 5.1a. Due to its topological origin the quantum Hall state is comparatively robust, in particular to the presence of impurities [22]. However, at high temperatures and high current densities dissipation is introduced into the system and the quantum Hall state breaks down. Above a critical current density $j_c = I_c/W$ a sudden onset of longitudinal resistance indicates the breakdown of the quantum Hall effect (see also Section 2.5.3 for more descriptions). The value of j_c is defined as the current density above which $V_{xx} > V_c$, where the critical voltage V_c is determined by the noise limit of the measurement. It can be extracted from the $I - V_{xx}$ characteristics in the quantum Hall state, as shown in Figure 5.1b, where $V_c = 0.5$ μV. By measuring the breakdown current as a function of magnetic field throughout the $\nu = 2$ plateau we are able to extract a wealth of data, in particular about the magnetic field dependent carrier density.

In traditional semiconductor quantum Hall systems, where the carrier density is constant, the breakdown current has been shown to have a triangular dependence on both filling factor and magnetic field, where a sharp peak is observed in j_c centred

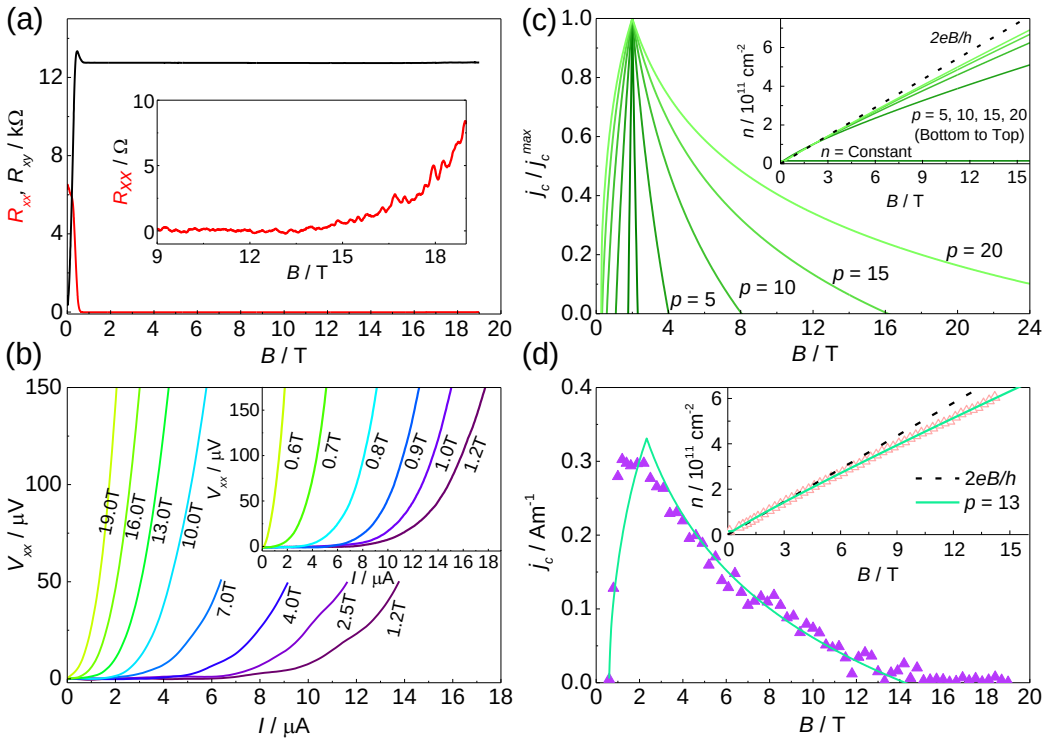

Figure 5.1: (a) Continuous field measurements of the quantum Hall effect at 2 K using a constant probing current of 1 μA in an SiC/G sample with the zero field carrier density reduced to 1.5×10^{10} cm^{-2} by corona discharge at room temperature. Inset: an expanded plot of R_{xx} towards the end of the plateau. (b) $I-V_{xx}$ traces indicating the onset of the quantum Hall breakdown for the high magnetic field side of the plateau and inset, for the low field side. (c) Theoretical dependence of the breakdown current for the $\nu = 2$ quantum Hall plateau using Equations 5.1 and 5.6 with $B_0 = 0.3$ T and $B_c = 2.0$ T. A set of dependences are shown with the power, p, chosen as 5, 10, 15, and 20. The traditional triangular dependence of breakdown current on magnetic field for constant n becomes stretched and asymmetric as the carrier density tends towards an almost linear dependence on magnetic field. The inset shows the corresponding field dependent carrier densities. (d) Magnetic field dependence of the breakdown current (purple triangles) for the $\nu = 2$ plateau and a best fit (solid line) using Equations 5.1 and 5.6 with the power $p = 13$. The inset shows the corresponding magnetic field dependent carrier density.

exactly at an integer filling factor (e.g. $\nu = 2$) and falling linearly to zero at the edges of the plateau (approximately at $\nu = 2 \pm \delta\nu$) [23–25], so that,

$$j_c(B) = j_c^{max}\left(1 - \frac{|\nu - 2|}{\delta\nu}\right), \tag{5.1}$$

where $\nu = \frac{nh}{eB}$ and $\delta\nu$ is typically in the range $0.2 < \delta\nu < 0.3$ [23–25]. As the Fermi

energy steadily moves away from the integer filling factor at higher or lower magnetic fields the extended states of the $N = 0$ or $N = 1$ Landau level become energetically easier to access, dissipation occurs at progressively lower probing currents until j_c decreases to zero. In order to explain the extremely wide plateaus observed in SiC/G both here and previously [3, 12, 16] it has been assumed that there is a strongly magnetic field dependent carrier density. As a result the occupancy of the $\nu = 2$ state changes only slowly with magnetic field thus creating an asymmetric and very broad j_c profile along the plateau (Figure 5.1d).

5.3.2 Determining the magnetic field dependence of E_F

In order to produce a quantitative measurement of the magnetic field dependent carrier density, the temperature dependence of the magneto-conductivity (σ_{xx}) of this sample has been studied.

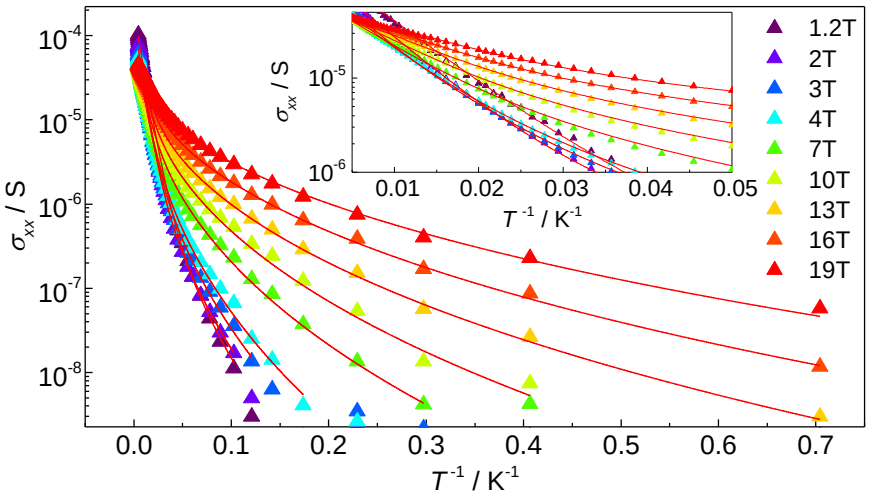

Figure 5.2: Longitudinal conductivity as a function of temperature from 1.4 to 200 K at various magnetic fields. Red solid lines are fits as described in the text. Inset: high temperature regime from 20 to 200 K.

The longitudinal conductivities as functions of inverse temperature from 1.4 to 200 K

for a series of magnetic fields are shown in Figure 5.2. The inset shows the relatively high temperature regime from 20 to 200 K where $\log \sigma_{xx}$ is more linear with $1/T$. In contrast, the non-linearity of the $\log \sigma_{xx} - 1/T$ plot at low temperatures shows the importance of variable range hopping (VRH) which causes significant deviations from the conventional Arrhenius activation behaviour. Excellent fits to the total longitudinal conductivity can be achieved however by combining thermal activation between extended states in adjacent Landau levels and VRH. The total conductivity is calculated as,

$$\sigma_{xx}(T) = \sigma_{TA} + \sigma_{VRH}, \tag{5.2}$$

where σ_{TA} and σ_{VRH} are due to the thermal activation and variable range hopping, respectively.

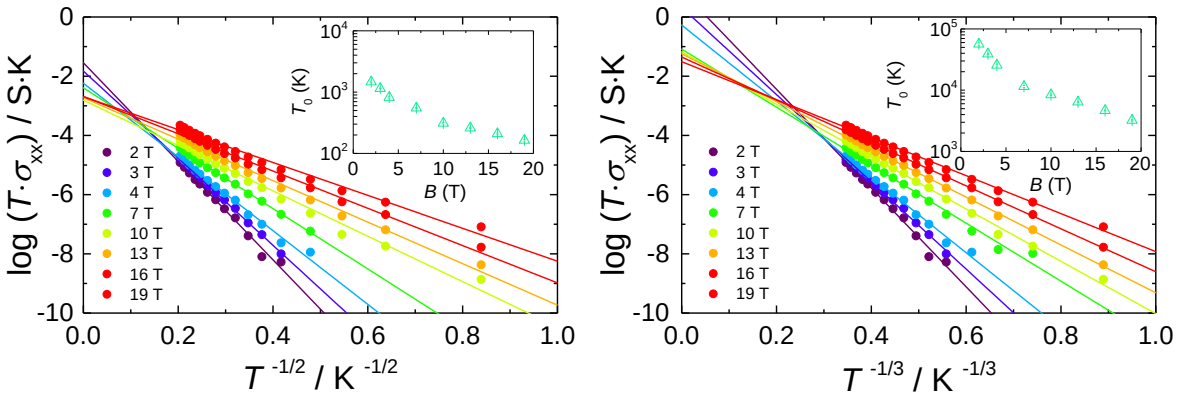

Figure 5.3: Comparison of the Efros-Shklovskii (left) and Mott (right) VRH models. The Mott model fits the high-field data only slightly better than the Efros-Shklovskii model, whereas for the low-field data, equally excellent fits are obtained using both models.

The most significant outcome of these fittings is the magnetic field dependence of the Fermi energy (E_F) which comes mainly from σ_{TA}, dominant at high temperatures. No significant difference in E_F is found by using either the Mott [26] or Efros-Shklovskii [27] VRH model for the low-temperature conductivity (see Figure 5.3 for comparisons), and in the subsequent analysis we show results using Mott VRH in two-dimensions [26],

i.e.,

$$\sigma_{VRH} \propto \frac{1}{T} \exp\left[-(T_0/T)^{1/3}\right], \tag{5.3}$$

where the characteristic temperature T_0 is a fitting parameter. In terms of σ_{TA}, obtaining a simple analytic formula can be difficult, especially when characteristics of Landau level broadening are taken into account [28–30]. Overall, the conductivity is fitted using a Gaussian DOS function as calculated from a path-integral method [31],

$$G(E) = \frac{g_v g_s eB}{2\pi\hbar} \sum_N (2\pi s^2)^{-1/2} \exp\left[-(E - E_N)^2/(2s^2)\right], \tag{5.4}$$

where $g_v = g_s = 2$ are the valley and spin degeneracies, E_N is the energy of the Nth Landau level, and the standard deviation s represents the Gaussian broadening of a Landau level. In our case the thermal energy is small compared with the Landau level separation and the only contributions are from the extended states within the mobility edges ($E_N \pm E_\mu$) at the centres of the $N = 0$ and $N = 1$ Landau levels. Since the Fermi level E_F is also well within the region of localised states, from the Kubo formula [30] we can then write,

$$\sigma_{TA} = \sum_{N=0,1} \left\{ \frac{e^2}{4\sqrt{\pi}\hbar} g_v g_s \left(N + \frac{1}{2}\right) \beta s \cdot e^{-k} \cdot \left[\mathrm{erf}\left(\gamma\beta s/2 + E_\mu/s\right) - \mathrm{erf}\left(\gamma\beta s/2 - E_\mu/s\right)\right] \right\}, \tag{5.5}$$

where $k = \gamma\beta(E_N - E_F) - (\beta s/2)^2$, $\beta = \frac{1}{k_B T}$, and $\gamma = \mathrm{sgn}(N - \frac{1}{2})$.

Employing the above formulation, the temperature-dependent magneto-conductivities are very well fitted across a wide temperature range from 1.4 up to 200 K, as shown in Figure 5.2. To avoid overfitting, the DOS of the $N = 0$ and $N = 1$ Landau levels are assumed to have fixed Gaussian broadening, i.e., s and E_μ are constants independent of magnetic field and temperature. The value of s is chosen to be ~ 12 meV in order to match the energy scale of the low-field Gaussian random disorder potentials in these systems [32] as shown in the previous chapter. E_μ is determined to be 7.8 meV

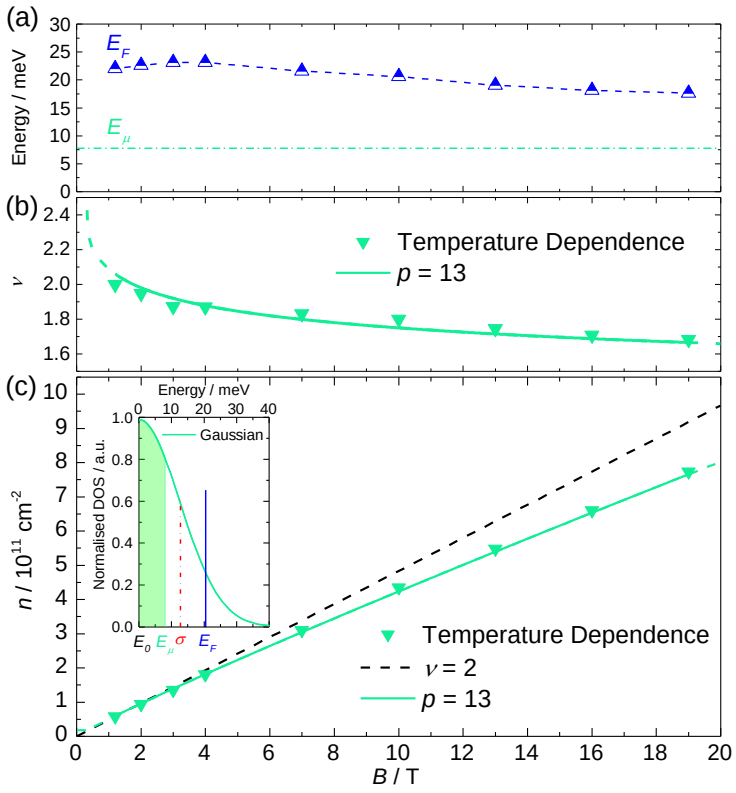

Figure 5.4: (a) E_F and E_μ as a function of magnetic field. (b), (c) Magnetic field dependence of the filling factor ν and the carrier density n extracted from the temperature dependence analysis (green triangles), and best fits (solid lines) with their extrapolation (dashed lines) using Equation 5.6 with the power $p = 13$. Inset: the Gaussian DOS used in the temperature dependence analysis with characteristic energy levels marked.

($|\Delta\nu| = 0.93$, i.e., almost 50% of the total states in each Landau level are extended) by fitting the data for $B = 1.2$ T, where E_F is known to be exactly at the mid-point between the two Landau levels since at elevated temperatures the minima in conductivity and R_{xx} are observed at this field. It is also noted that the dimensionless parameter $r = \frac{E_\mu}{\sqrt{2\ln 2}s} = 0.53$ in our sample is consistent with the value 0.5, which has been used to interpret similar Gaussian Landau level broadening and extended states widths from transport spectroscopy measurements in epitaxial graphene [33]. As the magnetic field increases, Figure 5.4a shows that E_F is a slowly decreasing quantity which approaches the mobility edge E_μ gradually. This suggests that the magnetic field dependent charge transfer rate is slightly lower than the increase in the total Landau level DOS. Figures

5.4b and 5.4c show the filling factor and the corresponding carrier density as functions of magnetic field, i.e. $n = \frac{\nu eB}{h} = \int_0^{E_F} G(E)dE$, where E_F as a function of magnetic field is given by Figure 5.4a and $G(E)$ is given by Equation 5.4.

In order to provide a quantitative relation to describe the charge transfer which can be compared to the magnetic field dependence of the breakdown current, the following phenomenological expression for the field dependent carrier density is introduced,

$$n(B) = \frac{2eB}{h}\left[\left(\frac{B_0}{B}\right)^p + \frac{B_c}{B}\right]^{1/p}, \tag{5.6}$$

where p, B_0 and B_c are fitting parameters. This expression is chosen as, for large values of p, it rapidly swaps over from a constant carrier density n_0 at low field, where $B_0 = \frac{n_0 h}{2e}$ corresponding to the magnetic field where $\nu = 2$ would occur if there were no charge transfer at this low field carrier density, to a slightly sublinear increase with field $\propto B^{1-\frac{1}{p}}$, where B_c is the magnetic field corresponding to j_c^{max} where $\nu = 2$ including the additional charge transfer. The carrier density and occupancy predicted by this equation for this sample are shown in Figure 5.4c and Figure 5.4b, and can be seen to provide an excellent description of the field dependence of both parameters when $p = 13$.

Using the analytical form for n given by Equation 5.6 we can now combine this with the expected form of the occupancy dependence of the quantum Hall breakdown current given by Equation 5.1 to give a prediction for the field dependence of the breakdown current density. A series of such predictions are shown in Figure 5.1c for $p = 5$, 10, 15 and 20, which demonstrates the appearance of a strong asymmetry and a considerable broadening of the breakdown current as a function of magnetic field. Figure 5.1d then compares the field dependence of j_c to the data deduced from Figure 5.1b with the optimum fitting parameter of $p = 13$ which gives an excellent description of the data and is therefore used in all subsequent fittings. The magnetic field at which j_c goes to zero (14 T) corresponds to an occupancy as deduced from the temperature dependence

of σ_{xx} of 1.74 (Figure 5.4b) so that we take $\delta\nu = 0.26$ in Equation 5.1, which is in good agreement with other measurements in both graphene and other systems [23–25]. In summary, the measurement of the field dependence of j_c is well described by fitting with Equations 5.1 and 5.6 and inversion of the fitting process also allows us to use the measurement of j_c as an independent measurement of the field dependent occupancy and hence of the field dependent carrier density, as shown in the inset to Figure 5.1d. It will be later shown that Equation 5.6 also agrees well, in the vicinity of the $\nu = 2$ plateau, with full numerical simulations as described in Section 5.3.5.

5.3.3 Pulsed field measurements of a 50 T wide $\nu = 2$ plateau

Using the above method we now use j_c to probe the carrier density up to much higher magnetic fields. Figure 5.5a shows the magnetic field dependence of the the longitudinal and Hall resistance, R_{xx} and R_{xy} respectively, measured using a constant current of 3 μA in a 57 T long pulse magnet. At both positive and negative magnetic fields the magnetotransport is dominated by the extended $\nu = 2$ plateau. Using the low field Hall coefficient an initial carrier density of 1.5×10^{11} cm^{-2} is extracted. Also at low magnetic fields a clear weak localisation peak in the resistivity [34], and even signatures of Shubnikov-de Haas oscillations for $\nu = 6$ and $\nu = 10$ (Figure 5.5a, lower inset) are observed. This shows that even with a total pulsed magnetic field measurement duration of around 300 ms the quality and accuracy of the data remains very high. The dissipationless $\nu = 2$ state begins at 3 T and is accompanied by a well quantised Hall resistance. Eventually at above $B = 50$ T, R_{xx} begins to increase as the Fermi level approaches the $N = 0$ Landau level and the extended states begin to be thermally populated. In order for the zero resistivity state to exist over this enormous magnetic field range this implies that the occupancy remains close to $\nu = 2$ due to a rapidly increasing carrier density as previously proposed.

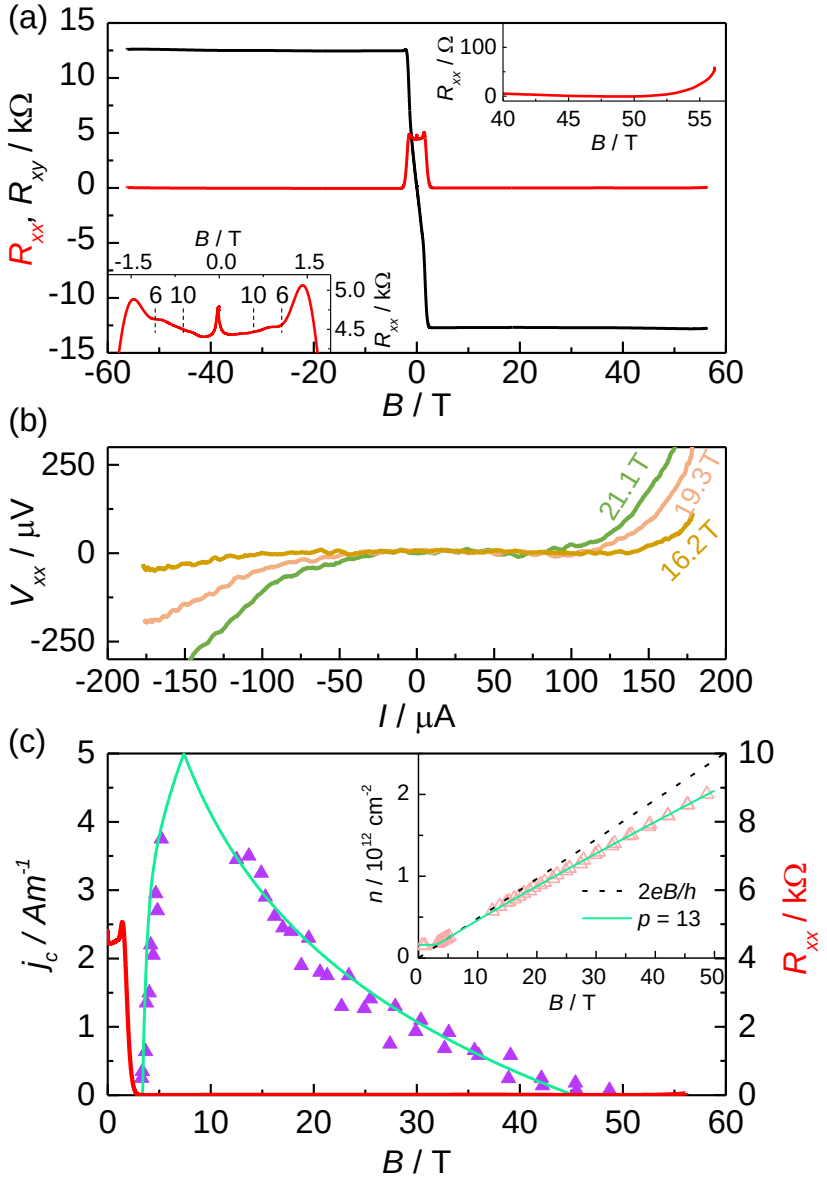

Figure 5.5: (a) Pulsed magnetic field measurements of the quantum Hall effect in epitaxial graphene on SiC at $T = 2$ K as observed in the longitudinal resistance (R_{xx}, red) and Hall resistance (R_{xy}, black) showing an exceptionally wide (~ 50 T) $\nu = 2$ plateau. Upper inset: The end of the plateau at $B > 50$ T. Lower inset: R_{xx} at low magnetic fields showing clear Shubnikov-de Haas oscillations and weak localisation. (b) Examples of high speed $I - V_{xx}$ traces taken during a single pulsed magnetic field measurement, showing that clear quantum Hall breakdown behaviour is observed. (c) Magnetic field dependence of the breakdown current (purple triangles) for the $\nu = 2$ plateau and a best fit (solid line) using Equations 5.1 and 5.6 with the power $p = 13$. The red line shows the longitudinal resistivity and the inset shows the corresponding magnetic field dependent carrier density.

To get a greater insight into this magnetic field dependent carrier density, the breakdown of the quantum Hall state at $\nu = 2$ is investigated by studying the increase of R_{xx} at high measurement currents, similar to the steady magnetic field measurements. To determine the value of I_c as a function of magnetic field during a magnetic field pulse, a set of $I - V_{xx}$ traces are measured using a 107 Hz alternating current source and digital oscilloscope with a sampling rate set at 1 MHz. Example traces are shown in Figure 5.5b. These traces are measured from both a rapid sinusoidal upsweep (50 ms) and a slower downsweep with an exponential decay constant of 100 ms of the pulses without showing any visible hysteresis. The time constant of the charge transfer process is therefore estimated to be a few milliseconds or less. From this we can extract I_c along the plateau, as shown in Figure 5.5c. The values extracted using this method compare well to those taken in the lower field range using steady-field measurements on the same sample.

As before, Equations 5.1 and 5.6 are used to fit the field dependence of j_c, with only the parameters B_0 and B_c varied as shown in Figure 5.5c. The fit is again excellent and when inverted to provide a measure of the carrier density from j_c, the density is found to increase from a zero field value of 1.5×10^{11} cm^{-2}, by over an order of magnitude to 2×10^{12} cm^{-2} at $B = 50$ T (Figure 5.5c inset).

5.3.4 Overview of samples

Using these results in combination with those previously published [3], a comparison of the magnetic field dependent carrier density of several samples can be made, with n_0 spanning almost three orders of magnitude. Figure 5.6a shows the fitted carrier density using Equations 5.1 and 5.6 as a function of magnetic field from six sets of measurements. The carrier density in all of the samples show a strong magnetic field dependence in the $\nu = 2$ regime. Additional measurements of the carrier density at low magnetic fields,

corresponding to the low field Hall coefficient and the magnetic field at which the $\nu = 6$ and 10 resistivity minima occur, show that carrier density remains almost constant at high filling factors.

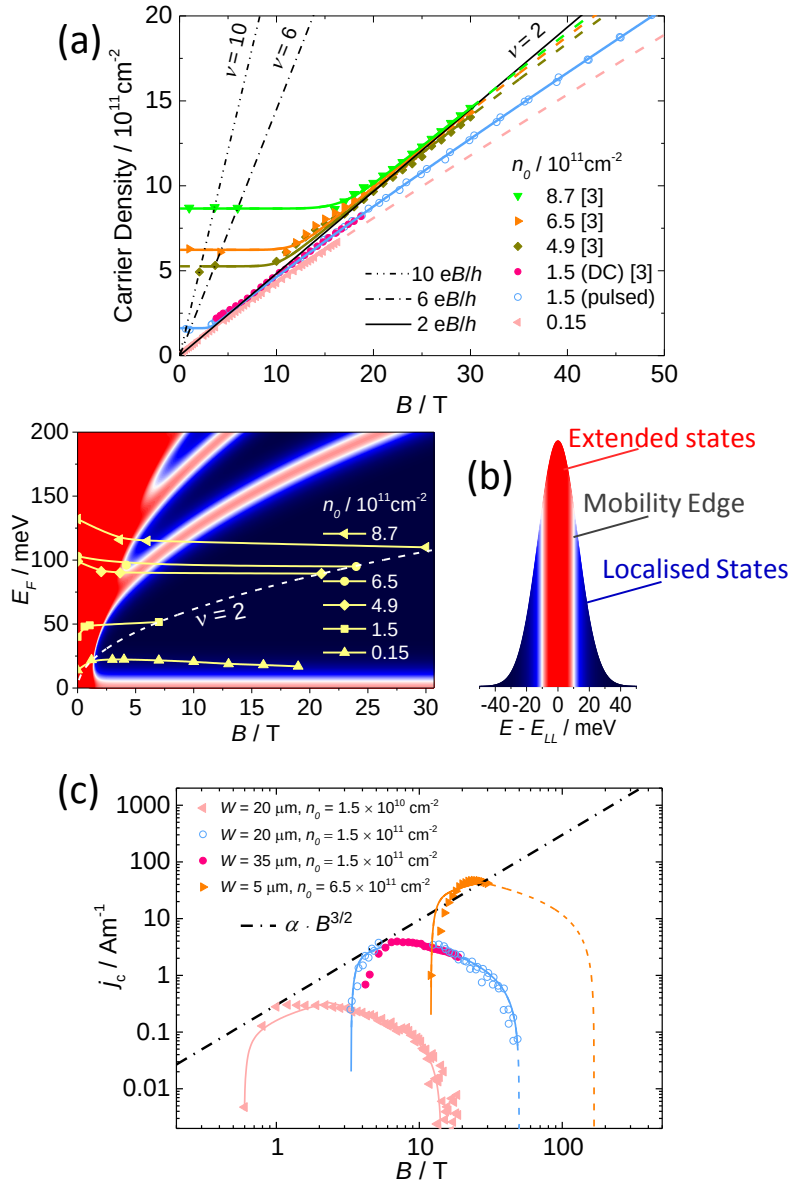

Figure 5.6: (a) Comparison of the carrier density deduced from the quantum Hall breakdown current with the values fitted with Equation 5.6 for several measurements on samples with different zero-field carrier densities. (b) The extracted magnetic field dependence of the Fermi energy in these samples based on the magnetic field assignments for $\nu = 4N + 2$. (c) Magnetic field dependence of j_c, showing that the peak breakdown current follows $B^{3/2}$ as observed in other quantum Hall systems. The solid lines show the predicted values from the fitting using Equations 5.1 and 5.6.

Finally, by using data points where the occupancy is known accurately such as at the resistivity minima for $\nu = 6$ and 10 and the field at which $\nu = 2$ peak breakdown occurs, we may estimate the chemical potential to be midway between Landau levels. This gives an estimate of the chemical potential as a function of magnetic field in all of the samples studied, in addition to the values extracted from the temperature dependence described above, which is plotted in Figure 5.6b relative to the energy of the Landau levels. In all cases the chemical potential is falling very slowly with increasing magnetic field. Together with the field dependence of the carrier density these results suggest the presence of charge reservoirs in close proximity to the graphene with exceptionally high densities of states. Using the field dependence of E_F and n in Figure 5.4a and Figure 5.6, these DOS can be estimated to be in the order of 10^{14} cm^{-2}eV^{-1} which is over an order of magnitude larger than suggested in initial reports [12]. Such a large density of states could arise from defects within the first few Si-C layers which may be created alongside the Si-sublimation process during the graphene growth, and also from the charge traps in the interface between graphene and the top gate materials.

These new data, combined with those published previously now also allow an investigation on the magnetic field dependence of the peak values of j_c, as shown in Figure 5.6c. It is seen that over a wide range of magnetic fields $j_c \propto B^{3/2}$, which has been observed previously in several studies in GaAs [24, 35, 36] and graphene [3]. In addition, by using the functional form of the carrier density given by Equation 5.6, the highest field limit at which the quantum Hall state should still exist (B_{max}^{QH}) can be predicted for the current batch of samples as,

$$B_{max}^{QH} \approx \left(\frac{2}{2-\delta\nu}\right)^{p} B_c = 6.1 B_c. \tag{5.7}$$

5.3.5 Modelling the magnetic field dependent charge transfer process

To get more insight into the magnetic field dependent charge transfer as discussed above and its effects on the breakdown of the QHE, this subsection now proposes a model which takes account of the interface states as charge reservoirs and the effects of quantum capacitances from each part of the system. It is noted that all the above analysis in this chapter is based on the picture of broadened Landau levels, instead of the unbroadened δ-function Landau levels which are assumed in the existing theoretical models [12, 16]. Therefore, this model may be viewed as an extension of those models to a framework of broadened Landau levels.

Given that all our epitaxial graphene samples are statically gated with PMMA as a gate insulator on top of the graphene, Equation (A12) from Ref. [16] can be adopted. At equilibrium with fixed gate voltage, we can write,

$$n - \gamma_{eff} E_F = Constant, \tag{5.8}$$

and,

$$\gamma_{eff} = \frac{\mathrm{d}n}{\mathrm{d}E_F} = -\left(\frac{\epsilon_1\gamma_1}{\epsilon_1 + \gamma_1 d_1 e^2} + \frac{\epsilon_2\gamma_2}{\epsilon_2 + \gamma_2 d_2 e^2}\right), \tag{5.9}$$

where $\epsilon_{1(2)}$, $\gamma_{1(2)}$, and $d_{1(2)}$ are the absolute permittivity, the assumed constant DOS of surface donor states, and the distance between graphene and the donor states for the SiC/graphene (graphene/PMMA) interface, respectively (see Figure 5.7b for a schematic representation[§]).

It is worth pointing out that in Equation 5.8, no assumption about the details of the DOS in graphene is required. Therefore, it is valid for both the equilibrium at zero field and the equilibria at high fields where the DOS of each Landau level is broadened. As

[§]An animated version of this figure may be found at https://youtu.be/F01zxlhT5JM.

the magnetic field increases, γ_{eff} is effectively the number of charges transferred into graphene per unit change of the Fermi energy, and it is a negative quantity as indicated in Equation 5.9 since the carrier density is increasing while the Fermi level is gradually falling to the mobility edge (Figures 5.4a and 5.6b) and eventually to zero.

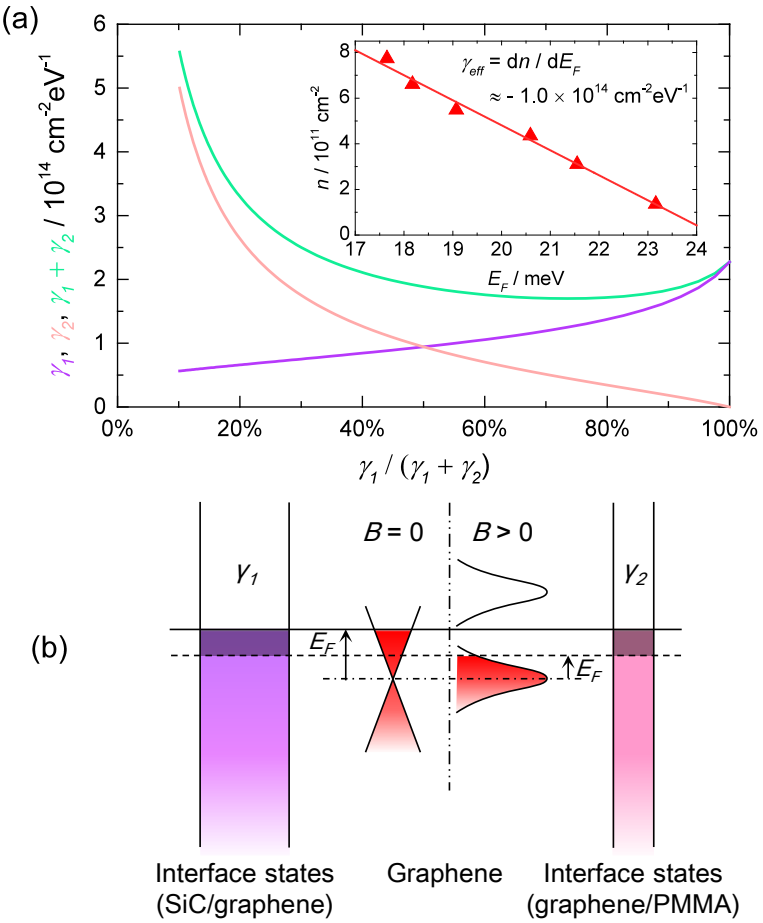

Figure 5.7: (a) Relation between the total density of interface states in the two charge reservoirs ($\gamma_1+\gamma_2$, green) and the individual component for SiC (γ_1, purple) and PMMA (γ_2, pink). Inset: carrier density as a function of Fermi level in our epitaxial graphene. (b) Schematic energy diagram of graphene at fixed gate voltage between two charge reservoirs with DOS γ_1 and γ_2, at $B = 0$ and $B > 0$. Shaded areas in the left and right reservoirs represent the additional electrons transferred into graphene due to magnetic field.

Figure 5.7a inset shows the carrier density as a function of the Fermi energy from the temperature dependence measurement (Figures 5.4a and 5.4c). It is well fitted with a straight line with its slope indicating $\gamma_{eff} \approx -1.0 \times 10^{14}$ cm^{-2}eV^{-1} for this

sample. Using $(\epsilon_1, \epsilon_2) = (9.7\epsilon_0, 3.5\epsilon_0)$ (ϵ_0 = vacuum permittivity), $d_1 = d_2 = 0.3$ nm, the relation between γ_1 and γ_2 is plotted in Figure 5.7a based on Equation 5.9. It is observed that when the density of surface states in SiC (γ_1) decreases from 30% to 0% of the total DOS in the two charge reservoirs, γ_2 will rapidly increase to infinity. It is not physical to have such a large DOS in the PMMA interface (γ_2), so it is unlikely that $\frac{\gamma_1}{\gamma_1+\gamma_2}$ will take a value below 30%. On the other hand, $\gamma_1 + \gamma_2$ remains roughly constant over a large range, $40\% < \frac{\gamma_1}{\gamma_1+\gamma_2} < 90\%$. We can therefore estimate the DOS in the reservoirs to be $\gamma_1 \sim 0.8 - 1.7 \times 10^{14}$ cm^{-2}eV^{-1}, $\gamma_2 \sim 0.3 - 1.3 \times 10^{14}$ cm^{-2}eV^{-1}, with $\gamma_1 + \gamma_2 \sim 2 \times 10^{14}$ cm^{-2}eV^{-1}. This estimation suggests that the surface states in SiC play a more significant role in the charge transfer process. The surface states responsible are closely related to the large number of atomic defects (vacancies and adatoms) predominantly located in the first underlying atomic layer, which consists of a non-conductive surface reconstruction of carbon atoms covalently bonded to the SiC which is formed during the growth process [12]. The existence of such surface defects with visually similar densities within this interfacial layer has been extensively reported from photo-emission and scanning tunnelling microscopy studies on various surface reconstructions [37–45]. These experiments have shown the existence of surface states distributed over an energy range of 0.5−1.5 eV in the region close to E_F [37, 40, 43–45] and have determined defect densities of order 2−4%. Assuming that one surface state originates from each defect site and the surface states are distributed in a typical energy range of 1 eV [42] within the bandgap, then using an atomic density $\sim 3.7 \times 10^{15}$ cm^{-2} for the reconstructed layer leads to DOS in the range of $0.8 - 1.5 \times 10^{14}$ cm^{-2}eV^{-1}. Despite the variations in experimental conditions, the reported values are consistent with the above estimate for γ_1. For the graphene/PMMA interface, the less significant but still relatively high γ_2 is attributed to the increased number of charge traps introduced by the intensive UV treatment [20, 46], and/or the high electric field involved in the corona gating process [21, 47].

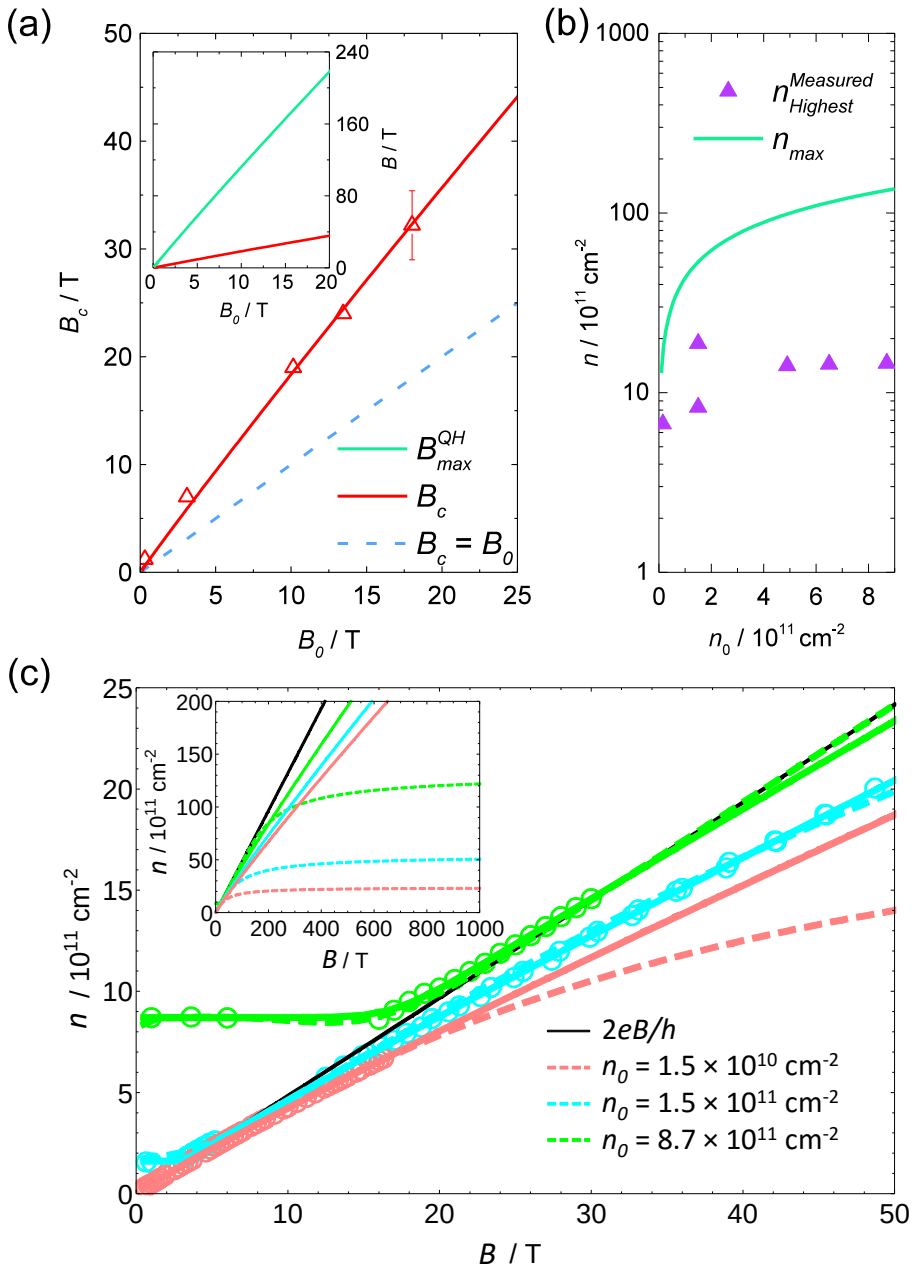

Figure 5.8: (a) B_c as a function of B_0, including the experimental data (red triangles), the prediction using Equation 5.10 (red solid line), and the case without charge transfer (blue dashed line). Inset: B^{QH}_{max} (green solid line) and B_c (red solid line) as functions of B_0. (b) Comparisons between n_{max} (green line) as a function of n_0 and $n^{Measured}_{Highest}$ (purple triangles) for our samples. (c) Simulations of complete $n(B)$ dependences given by our charge transfer model (dashed lines), compared with the experimental data (open circles) and Equation 5.6 (pink, cyan, green solid lines). Inset: Same comparisons up to extremely high magnetic fields.

Another important consequence from this model is that we can deduce B_c (the magnetic field corresponding to the occupancy $\nu = 2$ where the minimum R_{xx} and the maximum j_c occur) as a function of the zero field carrier density. Based on Equation 5.8, we have,

$$\frac{2eB_0}{h} - \gamma_{eff}\hbar v_F\sqrt{\pi\frac{2eB_0}{h}} = \frac{2eB_c}{h} - \gamma_{eff}\frac{v_F\sqrt{2\hbar eB_c}}{2}, \tag{5.10}$$

where v_F is the Fermi velocity. The left hand side and the right hand side of the equation represent the charge equilibrium at $B = 0$ and $B = B_c$, respectively, with E_F being $\hbar v_F\sqrt{\pi n_0}$ at $B = 0$, and at the mid-point between the $N = 0$ and $N = 1$ Landau levels $\frac{E_1+E_0}{2}$ at B_c. The solution to Equation 5.10 is plotted against B_0 (red lines) in Figure 5.8a, which is in excellent agreement with the experimental data (red triangles). Also shown (blue dashed line) is $B_c = B_0$, which represents the case of a constant carrier density without the field dependent charge transfer. Combining Equations 5.7 and 5.10, the model can also predict the magnetic field, B_{max}^{QH}, at which the end of the $\nu = 2$ plateau occurs, using B_0 as shown in the Figure 5.8a inset.

Finally, we can calculate the maximum carrier density n_{max} that can be transferred into graphene, corresponding to the limit $B \to \infty$ and $E_F \to 0$ when other high magnetic field effects (such as the fractional quantum Hall effect) are neglected. From Equation 5.8, we have,

$$n_0 - \gamma_{eff}\hbar v_F\sqrt{\pi n_0} = n_{max}, \tag{5.11}$$

or,

$$n_{max} = n_0 + 42.4\sqrt{n_0}, \tag{5.12}$$

where n_{max} and n_0 are both in units of 10^{11} cm^{-2}. This relation is shown in Figure 5.8b. n_{max} represents the upper limit to the possible validity of Equation 5.6 which occurs when the Fermi energy becomes pinned to the Dirac point as $B \to \infty$. In practice, the highest carrier densities reached in our measurements, $n_{Highest}^{Measured}$, as shown in Figure 5.8b, are much less than n_{max} due to the finite magnetic field strength that could be

applied. Therefore, in this regime, Equation 5.6 still provides an accurate description for $n(B)$.

Hence, with our model using a realistic framework of broadened Landau levels, we have been able to relate and accurately predict some of the most important characteristics (B_c, j_c^{max}, B_{max}^{QH}, n_{max}) of the breakdown of the quantum Hall effect and the field dependent charge transfer, using just the zero field carrier density (n_0 or B_0). These results can thus provide realistic references for the optimum operating conditions for a quantum Hall resistance standard using epitaxial graphene. It should be emphasised that this model can ultimately provide a complete $n(B)$ dependence, if the exact details of the Landau level broadening are known. Such dependences are simulated in Figure 5.8c, for three samples with each n_0 listed, by numerically solving the equation set,

$$n_0 - \gamma_{eff}\hbar v_F\sqrt{\pi n_0} = n - \gamma_{eff}E_F(n,B), \tag{5.13a}$$

$$n = \int_0^{E_F(n,B)} G(E)dE, \tag{5.13b}$$

where $G(E)$ is the DOS of Landau levels. In this simulation, we continue to assume Gaussian Landau level broadening, such that $G(E)$ is given by Equation 5.4, the same as in the above analysis of the temperature dependent conductivity. The same standard deviation $s = 12$ meV of the Gaussian broadening is also used for the same sample ($n_0 = 1.5\times10^{10}$ cm^{-2}) on which the temperature dependent measurements were made. For the samples with $n_0 = 1.5$ and 8.7×10^{11} cm^{-2} in which s is unknown, our model suggests values of about 25 and 30 meV, respectively, both well within the normal range among similar samples (see Table 4.1 in Section 4.3.1) [32]. As shown in Figure 5.8c, throughout the measurement range for each sample (i.e. $n < n_{Highest}^{Measured}$), excellent agreement is observed between the experimental data (open circles), the $n(B)$ dependences given by

our charge transfer model (dashed lines), and the those given by Equation 5.6 with $p = 13$ (solid lines). At high enough magnetic fields, the inset to Figure 5.8c shows that our model deviates from Equation 5.6 and predicts an upper limit to the number of electrons that can be transferred into graphene, corresponding to n_{max} as given by Equation 5.12 and shown in Figure 5.8b.

5.4 Summary

In summary, this chapter has presented studies on the breakdown and the temperature dependence of the quantum Hall effect using high magnetic fields and ultra-low density epitaxial graphene grown on SiC. The new measurements show that the full width of the $\nu = 2$ plateau can be observed in this system for low enough starting densities, n_0, and demonstrate the very large extent of the magnetic field dependent carrier density in epitaxial graphene. It has been shown that breakdown currents of the quantum Hall effect can be used to accurately measure this increase in carrier density with field, which is found to be over an order of magnitude in some cases. Using the models proposed, we have been able to accurately describe and predict some of the most important features of the field dependent charge transfer process and its effects on the quantum Hall breakdown. The models and results presented in this chapter are widely applicable towards a broader and deeper understanding of the magnetotransport properties of graphene and are crucial for engineering epitaxial graphene devices for applications such as quantum Hall metrology.

Bibliography

[1] K. von Klitzing, Rev. Mod. Phys. **58**, 519 (1986).

[2] B. Jeckelmann and B. Jeanneret, Meas. Sci. Technol. **14**, 1229 (2003).

[3] J. A. Alexander-Webber, A. M. R. Baker, T. J. B. M. Janssen, A. Tzalenchuk, S. Lara-Avila, S. Kubatkin, R. Yakimova, B. A. Piot, D. K. Maude, and R. J. Nicholas, Phys. Rev. Lett. **111**, 096601 (2013).

[4] L. B. Rigal, D. K. Maude, M. Potemski, J. C. Portal, L. Eaves, Z. R. Wasilewski, G. Hill, and M. A. Pate, Phys. Rev. Lett. **82**, 1249 (1999).

[5] T. J. B. M. Janssen, A. Tzalenchuk, S. Lara-Avila, S. Kubatkin, and V. I. Fal'ko, Rep. Prog. Phys. **76**, 104501 (2013).

[6] A. Tzalenchuk, S. Lara-Avila, A. Kalaboukhov, S. Paolillo, M. Syväjärvi, R. Yakimova, O. Kazakova, T. J. B. M. Janssen, V. Fal'ko, and S. Kubatkin, Nat. Nanotechnol. **5**, 186 (2010).

[7] T. J. B. M. Janssen, S. Rozhko, I. Antonov, A. Tzalenchuk, J. M. Williams, Z. Melhem, H. He, S. Lara-Avila, S. Kubatkin, and R. Yakimova, 2D Mater. **2**, 035015 (2015).

[8] R. S. Deacon, K.-C. Chuang, R. J. Nicholas, K. S. Novoselov, and A. K. Geim, Phys. Rev. B **76**, 081406 (2007).

[9] A. M. R. Baker, J. A. Alexander-Webber, T. Altebaeumer, and R. J. Nicholas, Phys. Rev. B **85**, 115403 (2012).

[10] A. M. R. Baker, J. A. Alexander-Webber, T. Altebaeumer, S. D. McMullan, T. J. B. M. Janssen, A. Tzalenchuk, S. Lara-Avila, S. Kubatkin, R. Yakimova, C.-T. Lin, L.-J. Li, and R. J. Nicholas, Phys. Rev. B **87**, 045414 (2013).

[11] S. Kopylov, A. Tzalenchuk, S. Kubatkin, and V. I. Fal'ko, Appl. Phys. Lett. **97**, 112109 (2010).

[12] T. J. B. M. Janssen, A. Tzalenchuk, R. Yakimova, S. Kubatkin, S. Lara-Avila, S. Kopylov, and V. I. Fal'ko, Phys. Rev. B **83**, 233402 (2011).

[13] B. Jouault, N. Camara, B. Jabakhanji, A. Caboni, C. Consejo, P. Godignon, D. K. Maude, and J. Camassel, Appl. Phys. Lett. **100**, 052102 (2012).

[14] T. Shen, J. J. Gu, M. Xu, Y. Q. Wu, M. L. Bolen, M. A. Capano, L. W. Engel, and P. D. Ye, Appl. Phys. Lett. **95**, 172105 (2009).

[15] J. Jobst, D. Waldmann, F. Speck, R. Hirner, D. K. Maude, T. Seyller, and H. B. Weber, Phys. Rev. B **81**, 195434 (2010).

[16] K. Takase, S. Tanabe, S. Sasaki, H. Hibino, and K. Muraki, Phys. Rev. B **86**, 165435 (2012).

[17] Y. Yang, L.-I. Huang, Y. Fukuyama, F.-H. Liu, M. A. Real, P. Barbara, C.-T. Liang, D. B. Newell, and R. E. Elmquist, Small **11**, 90 (2015).

[18] F. Lafont, R. Ribeiro-Palau, D. Kazazis, A. Michon, O. Couturaud, C. Consejo, T. Chassagne, M. Zielinski, M. Portail, B. Jouault, F. Schopfer, and W. Poirier, Nat. Comm. **6**, 6806 (2015).

[19] S. Lara-Avila, A. Tzalenchuk, S. Kubatkin, R. Yakimova, T. J. B. M. Janssen, K. Cedergren, T. Bergsten, and V. Fal'ko, Phys. Rev. Lett. **107**, 166602 (2011).

[20] S. Lara-Avila, K. Moth-Poulsen, R. Yakimova, T. Bjørnholm, V. Fal'ko, A. Tzalenchuk, and S. Kubatkin, Adv. Mater. **23**, 878 (2011).

[21] A. Lartsev, T. Yager, T. Bergsten, A. Tzalenchuk, T. J. B. M. Janssen, R. Yakimova, S. Lara-Avila, and S. Kubatkin, Appl. Phys. Lett. **105**, 063106 (2014).

[22] R. B. Laughlin, Surf. Sci. **113**, 22 (1982).

[23] H. Iizuka, S. Kawaji, and T. Okamoto, Physica E **6**, 132 (2000).

[24] B. Jeckelmann and B. Jeanneret, Rep. Prog. Phys. **64**, 1603 (2001).

[25] J. A. Alexander-Webber, A. M. R. Baker, P. D. Buckle, T. Ashley, and R. J. Nicholas, Phys. Rev. B **86**, 045404 (2012).

[26] N. F. Mott, Philos. Mag. **19**, 835 (1969).

[27] A. L. Efros and B. I. Shklovskii, J. Phys. C **8**, L49 (1975).

[28] R. J. Nicholas, R. A. Stradling, and R. J. Tidey, Solid State Commun. **23**, 341 (1977).

[29] T. Ando, A. B. Fowler, and F. Stern, Rev. Mod. Phys. **54**, 437 (1982).

[30] N. Shon and T. Ando, J. Phys. Soc. Jpn. **67**, 2421 (1998).

[31] R. R. Gerhardts, Surf. Sci. **58**, 227 (1976).

[32] J. Huang, J. A. Alexander-Webber, A. M. R. Baker, T. J. B. M. Janssen, A. Tzalenchuk, V. Antonov, T. Yager, S. Lara-Avila, S. Kubatkin, R. Yakimova, and R. J. Nicholas, Phys. Rev. B **92**, 075407 (2015).

[33] K. Takase, H. Hibino, and K. Muraki, Phys. Rev. B **92**, 125407 (2015).

[34] F. V. Tikhonenko, D. W. Horsell, R. V. Gorbachev, and A. K. Savchenko, Phys. Rev. Lett. **100**, 056802 (2008).

[35] G. Ebert, K. von Klitzing, K. Ploog, and G. Weinmann, J. Phys. C: Solid State Phys. **16**, 5441 (1983).

[36] H. Tanaka, H. Kawashima, H. Iizuka, H. Fukuda, and S. Kawaji, J. Phys. Soc. Jpn. **75**, 014701 (2006).

[37] I. Forbeaux, J.-M. Themlin, and J.-M. Debever, Phys. Rev. B **58**, 16396 (1998).

[38] F. Owman and P. Mårtensson, J. Vac. Sci. Technol. B **14**, 933 (1996).

[39] N. P. Guisinger, G. M. Rutter, J. N. Crain, C. Heiliger, P. N. First, and J. A. Stroscio, J. Vac. Sci. Technol. A **26**, 932 (2008).

[40] L. I. Johansson, F. Owman, and P. Mårtensson, Surf. Sci. **360**, L483 (1996).

[41] C. Riedl, U. Starke, J. Bernhardt, M. Franke, and K. Heinz, Phys. Rev. B **76**, 245406 (2007).

[42] F. Hiebel, L. Magaud, P. Mallet, and J.-Y. Veuillen, J. Phys. D: Appl. Phys. **45**, 154003 (2012).

[43] Th. Seyller, K. V. Emtsev, K. Gao, F. Speck, L. Ley, A. Tadich, L. Broekman, J. D. Riley, R. C. G. Leckey, O. Rader, A. Varykhalov, and A. M. Shikin, Surf. Sci. **600**, 3906 (2006).

[44] K. V. Emtsev, F. Speck, Th. Seyller, L. Ley, and J. D. Riley, Phys. Rev. B **77**, 155303 (2008).

[45] M. S. Nevius, M. Conrad, F. Wang, A. Celis, M. N. Nair, A. Taleb-Ibrahimi, A. Tejeda, and E. H. Conrad, Phys. Rev. Lett. **115**, 136802 (2015).

[46] N. Benson, C. Melzer, R. Schmechel, and H. von Seggern, Phys. Status Solidi A **205**, 475 (2008).

[47] H. Sirringhaus, Adv. Mater. **21**, 3859 (2009).

6

Hot Carrier Relaxation of Massive Dirac Fermions in Bilayer Epitaxial Graphene

Energy relaxation of hot massive Dirac fermions in bilayer epitaxial graphene is experimentally investigated by magnetotransport measurements on Shubnikov-de Haas oscillations and weak localisation. The hot-electron energy loss rates are found to follow the predicted Bloch-Grüneisen power-law behaviour of T^4 at carrier temperatures from 1.4 up to about 100 K, due to electron-acoustic phonon interactions with a deformation potential coupling constant of 22 eV. A carrier density dependence $n_e^{-1.5}$ in the scaling of the T^4 power law is observed in bilayer graphene, in contrast to the $n_e^{-0.5}$ dependence in monolayer graphene, leading to a crossover in the energy loss rate as a function of carrier density between these two systems. The electron-phonon relaxation time in bilayer graphene is also shown to be strongly carrier density dependent, while it remains constant for a wide range of carrier densities in monolayer graphene. The results and comparisons between the bilayer and monolayer presented in this chapter exhibit a more comprehensive picture of hot carrier dynamics in graphene systems.

The work in this chapter has been published in *J. Phys. Condens. Matter* **27**, 164202 (2015).

Contents

6.1 Introduction

The discovery of graphene [1], a truly 2D system in the carbon materials family, has sparked extensive theoretical and experimental research over the last decade, on the physics of the unique Dirac fermions [2, 3] as well as its potential to become a key element for a wide range of applications [4]. A significant focus has been on its carrier transport properties and scattering mechanisms. In particular, hot carrier dynamics in graphene has considerable importance in determining the performance of high frequency and high power electronics, high-speed sensors, thermal management of electronic devices, and quantum Hall metrology for accurate measurements under the conditions of elevated temperatures and/or currents [5].

In monolayer graphene, very high energy loss rates with electron-phonon relaxation times an order of magnitude shorter than that of a conventional 2DEG, such as in GaAs/$Ga_{1-x}Al_xAs$ heterojunctions, have been observed [6–9], making monolayer

graphene an even more promising candidate for the above mentioned applications. Despite the exceptional electronic properties, the lack of a bandgap in monolayer graphene limits its potential applications. On the other hand, a small energy gap can be opened and continuously tuned by an external electric field in a coupled graphene bilayer system [10], allowing more control and flexibility for technological purposes. Very recently, energy loss rates for hot carriers in bilayer graphene have been theoretically explored taking into account the interactions of electrons with acoustic and surface polar phonons as well as hot phonon effects [11–13], but to date this has yet to be studied in significant detail experimentally.

This chapter describes experimental investigations of the energy loss dynamics of hot carriers in bilayer epitaxial graphene obtained by magnetotransport measurements, using two independent techniques: firstly from the damping of Shubnikov-de Haas oscillations at high magnetic fields and secondly from the suppression of weak localisation peaks in the low magnetic field regime. Energy loss rates, together with electron-phonon relaxation times are extracted in the carrier temperature range of 1.4 to around 100 K and the carrier density dependence is determined. Comparisons are then made between our data and theoretical predictions [11–13], as well as the energy loss behaviour in monolayer graphene [6, 7, 14].

6.2 Methods

6.2.1 Sample preparation

The samples used in this study were grown and fabricated by R. L. Myers-Ward, V. D. Wheeler, D. K. Gaskill from the US Naval Research Laboratory, and T. Yager, S. Lara-Avila, S. Kubatkin from Chalmers University of Technology in Sweden, and were provided to us by T. J. B. M. Janssen and A. Tzalenchuk from the National Physical

Laboratory in the UK. Bilayer graphene was synthesised on semi-insulating (resistivity $> 10^9$ Ω·cm) (0001) 6H-SiC that was misoriented less than 0.1 degree from the $[11\bar{2}0]$ direction. Prior to graphene synthesis, the substrate was etched during the ramp to growth temperature in 5 standard litres per minute (slm) of Pd-purified H_2 at 200 mbar. Graphene synthesis was then performed at 1590 °C for 25 minutes in 10 slm of high purity Ar at 100 mbar [15]. The film was subsequently characterised by x-ray photoelectron spectroscopy (XPS), performed by Gaskill's group. Using the attenuation of the C 1s and Si 2p signals from the substrate [16], the graphene thickness was determined to be approximately 1.5 monolayers, corresponding to 50% coverage of bilayer graphene within a 400 μm spot size. Subsequent optical transmission measurements (performed by the Chalmers group) over micrometer lateral dimensions confirmed the thickness [17].

Eight-leg Hall bars of various sizes were fabricated using electron beam lithography followed by O_2 plasma etching and large-area titanium-gold Ohmic contacting. The non-volatile dual-polymer gating techniques (see Section 3.4.1 for more details) [18] using PMMA/MMA and ZEP520A were applied to tune the carrier density in our bilayer epitaxial graphene by UV illumination or corona discharge [19] at room temperature. Three devices with electron densities of 1.17, 1.90, 2.83 $\times 10^{12}$ cm^{-2}, and mobilities of 3080, 2055, 1503 cm^{2}V^{-1}s^{-1}, respectively, measured at 1.4 K, were used in this study. All the devices measured were selected from the bilayer-rich regions and have small dimensions ($20 - 30$ microns wide), in order to minimise the effects of long range inhomogeneities. Magnetotransport measurements, as will be shown below, confirmed that the devices used in this study had mostly bilayer graphene.

6.2.2 Magnetotransport measurements

Electrical measurements were carried out using a nitrogen and helium cooled Oxford Instruments 21 T superconducting magnet with a variable temperature insert which can

provide steady temperatures in the sample environment from 1.4 up to 300 K. Four-terminal measurements were made using Keithley 2000 DMMs. DC currents higher than 10 μA were supplied by a Keithley SMU and currents from 100 nA to 10 μA were supplied by a battery-powered constant current source to reduce noise as detailed in Section 3.4.2.

6.3 Results and discussions

6.3.1 Shubnikov-de Haas oscillations and effective mass of electrons in bilayer graphene

When external energy is added to a system of charge carriers, they will gain energy and heat up if the power loss to the lattice is less than the power input to the system. After the system undergoes an ultra-fast quasithermalisation within the electron gas via electron-electron interaction in a timescale of tens of femto-seconds, the distribution function of the hot carriers deviates from the original low-energy equilibrium form and manifests itself into a Fermi-Dirac distribution which can be described by an effective temperature T_e. The hot carriers then lose energy to the lattice via electron-phonon interaction on a much longer timescale.

To study the hot carrier dynamics for the case of external energy supplied by an electric field, the carrier temperature, T_e, as a function of electrical input power is determined. This relation can be obtained by recording the damping of the amplitudes of Shubnikov-de Haas oscillations [6–8, 20] versus current at a fixed low lattice temperature T_L, and then comparing those with the measurements under a fixed small current condition while changing the ambient temperature, since the damping is a result of thermal broadening of the hot carrier distribution in both cases. The damped amplitude

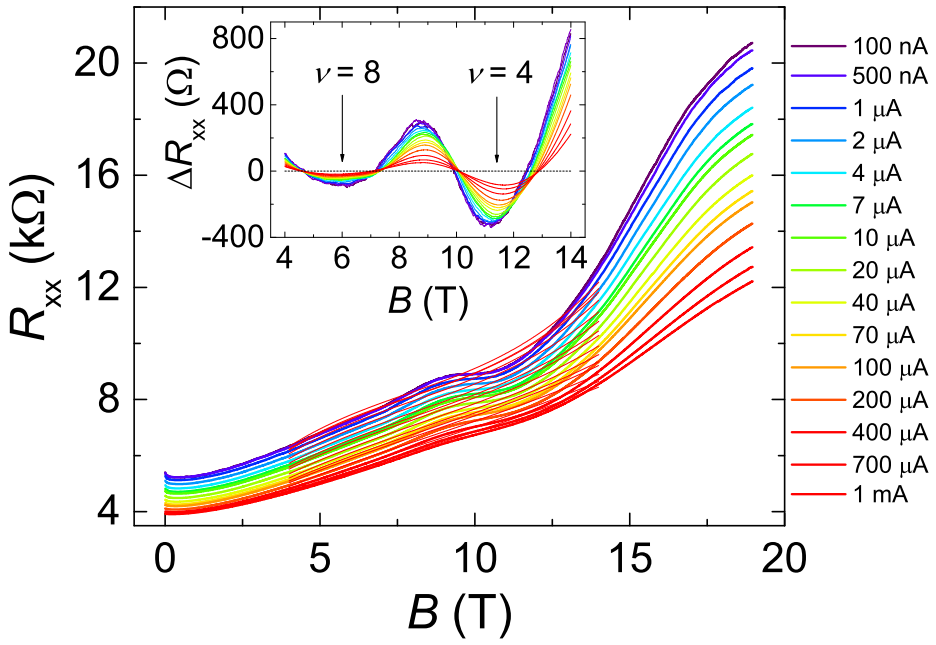

Figure 6.1: Longitudinal resistance R_{xx} as a function of magnetic field for different input currents ranging from 100 nA to 1 mA, taken at 1.4 K from a bilayer epitaxial graphene sample with carrier density of 1.17×10^{12} cm^{-2}. Red lines between 4 and 14 T are 3rd order polynomials used to subtract the slowly varying background in order to reveal small SdH oscillations. Inset shows the results after the background subtraction.

ΔR_{xx} (the change in two-dimensional magneto-resistance R_{xx}) can be expressed using the Lifshitz-Kosevich formula [21],

$$\frac{\Delta R_{xx}}{R_{xx}} \propto \frac{\chi}{\sinh \chi}, \tag{6.1}$$

where χ is a function of the effective mass m^*, the electron temperature and the magnetic field B, for a conventional two-dimensional electron gas,

$$\chi = \frac{2\pi^2 k_B T_e m^*}{\hbar e B}. \tag{6.2}$$

Equation 6.2 (also shown as Equation 2.40 in Chapter 2) is based on the assumption that data is taken from the regime where $\frac{\Delta R_{xx}}{R_{xx}}$ is small so that the electric field across the sample and the two-dimensional density of states can both be regarded as constants.

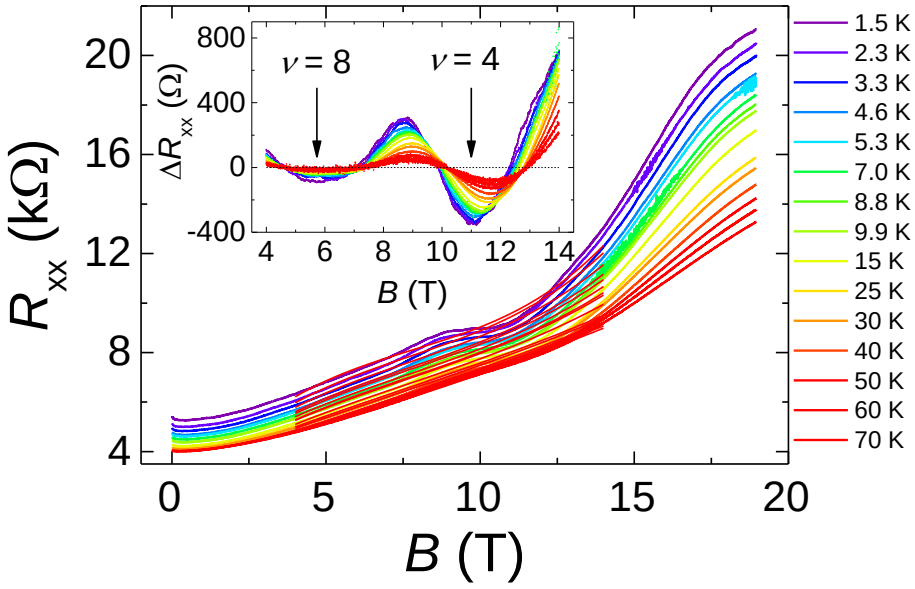

Figure 6.2: Longitudinal resistance R_{xx} as a function of magnetic field for different temperatures ranging from 1.5 to 70 K, taken at a fixed current of 100 nA from the same sample as in Figure 6.1. Red lines between 4 and 14 T are 3rd order polynomials used to subtract the slowly varying background in order to reveal small SdH oscillations. Inset shows the results after the background subtraction.

Figure 6.1 shows the magneto-resistance for a series of currents from 100 nA to 1 mA at a fixed low lattice temperature of 1.4 K, which is effectively anchored by the continuous cooling via helium gas flow in the sample environment. A third order polynomial background subtraction is used to reveal the Shubnikov-de Haas oscillations (Figure 6.1 inset) from the observed slowly varying background. The polynomial lines are best fits to the data in the range of interest from 4 to 14 T with more weight given to the low magnetic field regime where SdH oscillations are relatively small. Two clear resistance minima are observed corresponding to filling factors ($\nu = n_e h/eB$) of 4 and 8, which are also consistent with plateau-like features in the R_{xy}, confirming the bilayer nature of the sample [22]. The amplitudes of the SdH oscillations are found to be strongly damped by increasing input current. The damping was then measured as a function of ambient temperature (i.e. $T_e = T_L = T_{VTI}$) as shown in Figure 6.2, using a constant low current (100 nA) condition to avoid additional carrier heating. Using the

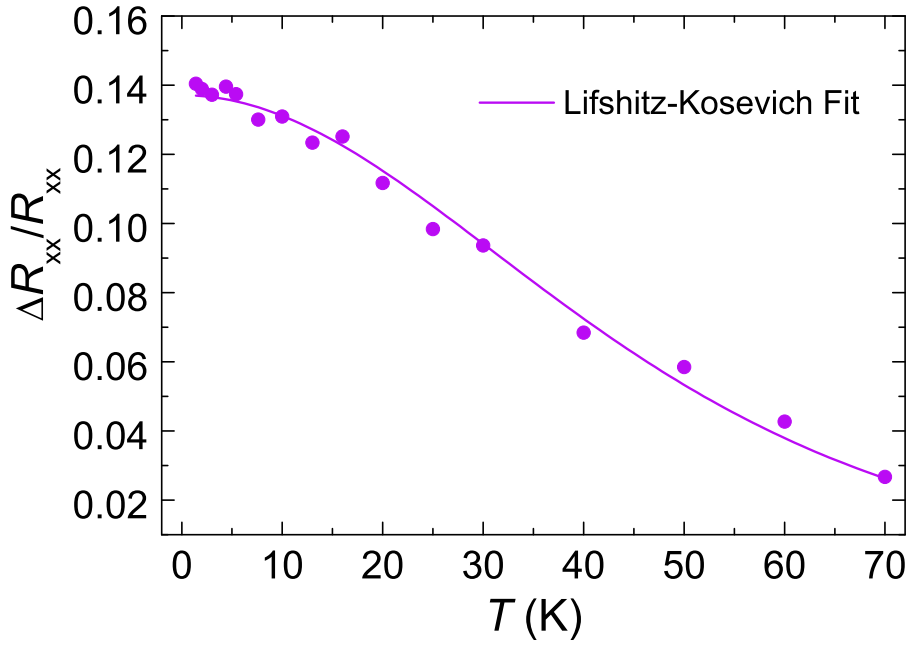

Figure 6.3: Temperature dependence of the normalised amplitude of SdH oscillations, fitted with Equations 6.1 and 6.2, giving an effective mass of $0.033m_e$ for bilayer epitaxial graphene.

Lifshitz-Kosevich formula (Equation 6.1), the effective mass m^* of electrons in bilayer graphene is determined to be $0.033m_e$ (for an electron density of 2.83×10^{12} cm^{-2} as an example shown in Figure 6.3), which coincides with the value found in previous experiments and theoretical calculations [23–26].

Comparing the damped amplitudes using both minima and maxima of the SdH oscillations from the current and temperature dependences, the electron temperature as a function of applied current is obtained, shown in Figure 6.4. In steady state, energy balance requires that the energy loss rate should equal the power input to the system. The energy loss rate per carrier for a given electron temperature can be therefore deduced as

$$P(T_e) = \frac{I^2 R_{xx}}{n_e A}, \tag{6.3}$$

where I is the applied current, n_e is the carrier density which can be extracted from low field Hall coefficients, and A is the area within the device over which R_{xx} is measured.

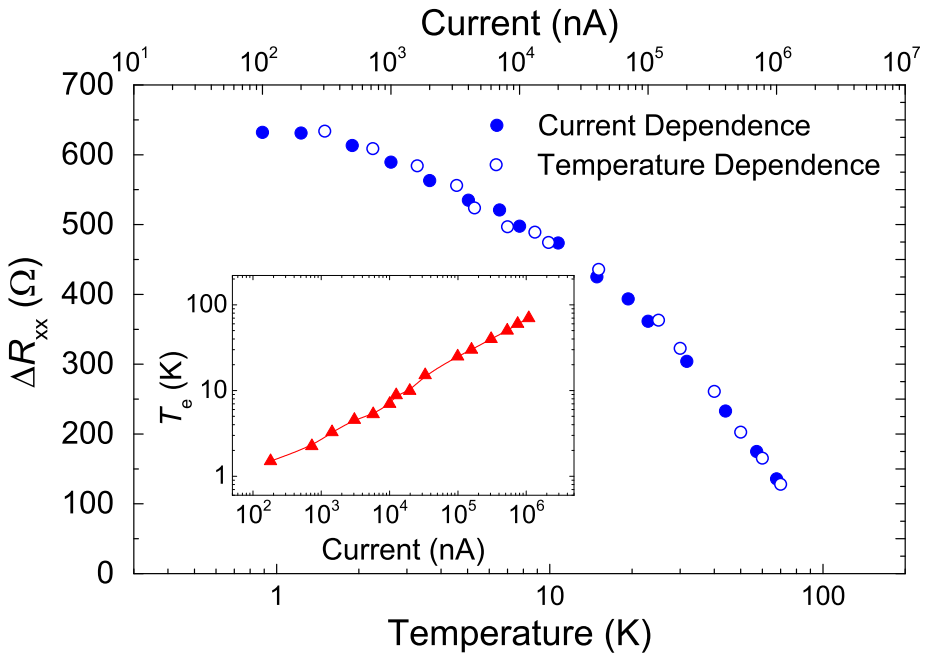

Figure 6.4: Comparison between the current (full circles) and temperature (open circles) dependences of the amplitudes of SdH oscillations. Inset shows the obtained carrier temperature T_e as a function of injected current.

6.3.2 Weak localisation

Another prominent feature of the magnetotransport is the presence of resistance peaks due to weak localisation (see also Section 2.4.2 for further information) arising from constructive quantum interference [27] at low magnetic fields (Figure 6.5). This leads to a second experimental technique to obtain the relationship between the carrier temperature and the corresponding current by measuring the suppression of the weak localisation peak heights. This technique has been demonstrated to be extremely helpful in determining the energy loss rates for samples in which SdH oscillations are difficult to be observed [6]. Moreover, it enables a more accessible measurement using magnetic fields less than 1 Tesla.

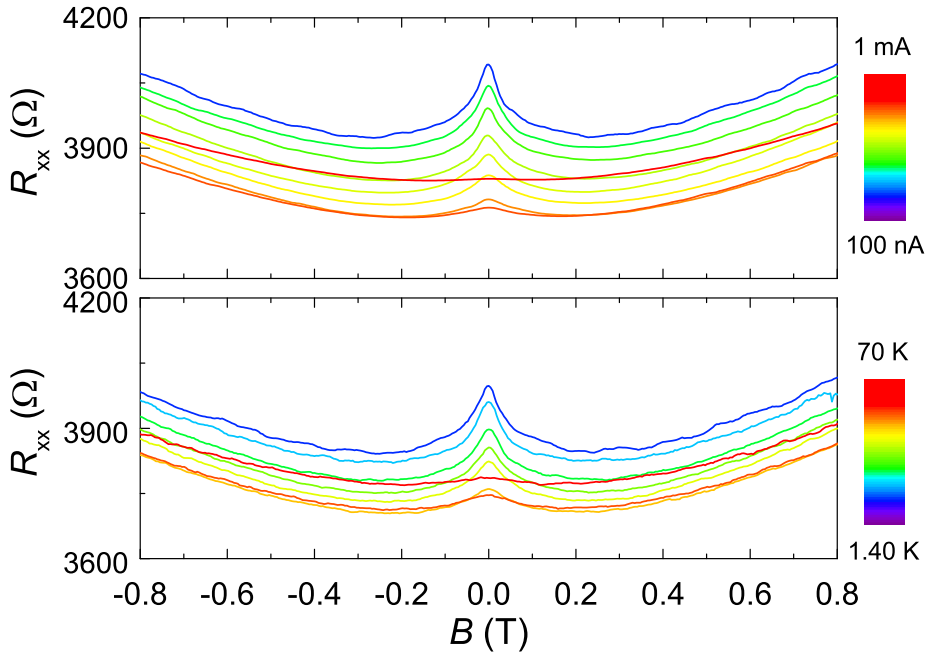

Figure 6.5: Suppression of the weak localisation peaks by increasing current (top) from 100 nA to 1 mA at a fixed $T_L = 1.4$ K, and by increasing ambient temperature (bottom) from 1.4 to 70 K at a fixed small current of 100 nA.

The peak height can be calculated as the difference of the longitudinal resistance R_{xx} between 0 T and fixed small magnetic field of 0.2 T. All the current dependence data were taken at a very low lattice temperature of 1.4 K, while all the temperature dependence data were obtained from measurements using a low fixed current of 100 nA. The peak height is significantly suppressed by increasing current or ambient temperature, and the comparison of the suppressed values between these two dependences generates a separate measure of the carrier temperature as a function of applied current (Figure 6.6), in addition to the SdH method.

This method is based on the fact that the amplitude of the weak localisation correction to the magneto-resistivity is mainly controlled by the dephasing rate (τ_ϕ^{-1}), which is normally considered to be primarily due to electron-electron interactions [6, 28–30] at low temperatures and only depends on T_e. Therefore, at equilibrium, an increase of the ambient temperature and the electron temperature will have an equal effect on the

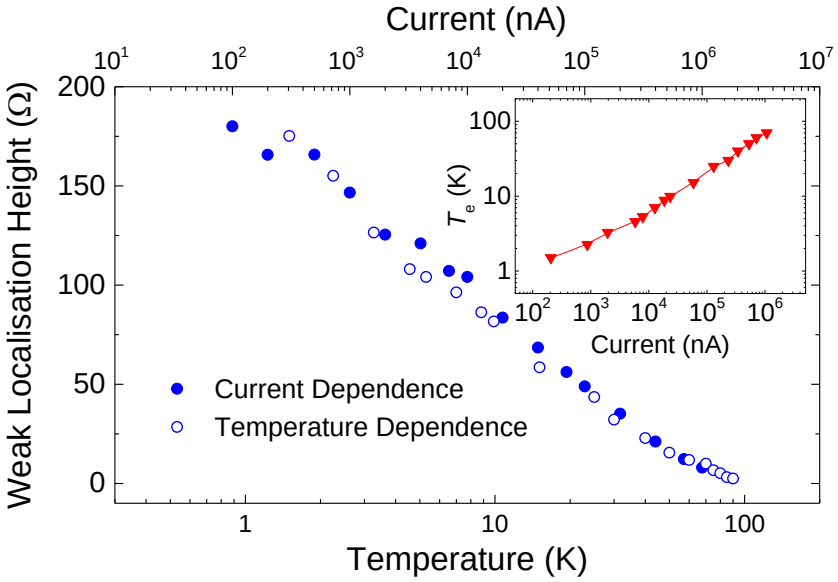

Figure 6.6: Current (full circles) and temperature (open circles) dependences of the weak localisation peak height. Inset shows the $I - T_e$ relationship obtained using this WL method.

weak localisation. This is also shown in Figure 6.6, where the forms of the current and temperature dependences qualitatively agree with each other.

6.3.3 Energy loss rates

The energy loss rate as a function of electron temperature is evaluated using Equation 6.3 from the $I - T_e$ relationships determined by both the SdH and WL techniques. Previous studies including our previous work have found that, in various materials from conventional semiconductors, such as GaAs, to monolayer graphene, the energy loss rates obtained from the two techniques show good correspondence [6, 28, 31]. Even though the WL is a low-field effect and the SdH oscillations are observed at high magnetic fields, good agreement is also found here for bilayer graphene.

In Figure 6.7 the energy loss rates per carrier are shown for the bilayer epitaxial graphene sample with an electron density of 1.17×10^{12} cm^{-2} over a carrier temperature

range of 1.4 to 80 K. The SdH and WL techniques give nearly identical results, which are both well described using a power law dependence

$$P = \alpha \left(T_e^4 - T_L^4\right), \tag{6.4}$$

where α is a carrier density dependent scaling factor, and the lattice temperature T_L is 1.4 K, resulting in a downward turn of the curve at very low temperatures. The results for bilayer graphene are firstly compared with the power loss in monolayer epitaxial and mechanically exfoliated graphene with similar carrier densities, taken from our previous studies [6, 7]. For this particular carrier density, hot carriers with an identical thermally broadened distribution (same T_e) in bilayer graphene lose energy at a rate approximately 2 to 3 times higher than in monolayer graphene. However, as we will show below, the energy loss rate for these two systems have significantly different carrier density dependences.

To further validate the T^4 behaviour and study the effects of carrier density on α in bilayer graphene, results from three different carrier densities are compared (Figure 6.8) from measurements using both the SdH and WL techniques. The energy loss rates associated with the three different carrier densities all behave in very good agreement with Equation 6.4, with different pre-factors. The inset of Figure 6.8 shows α as a function of carrier density. In contrast with the T_e^5 behaviour [32] of other conventional 2DEG, according to theoretical predictions for the power loss in bilayer graphene by Kubakaddi [11], within the low-temperature Bloch-Grüneisen (BG) regime, interactions between hot electrons and 2D acoustic phonons indeed give a T^4 power law

$$P_{el-ap} = F(T_e) - F(T_L), \tag{6.5}$$

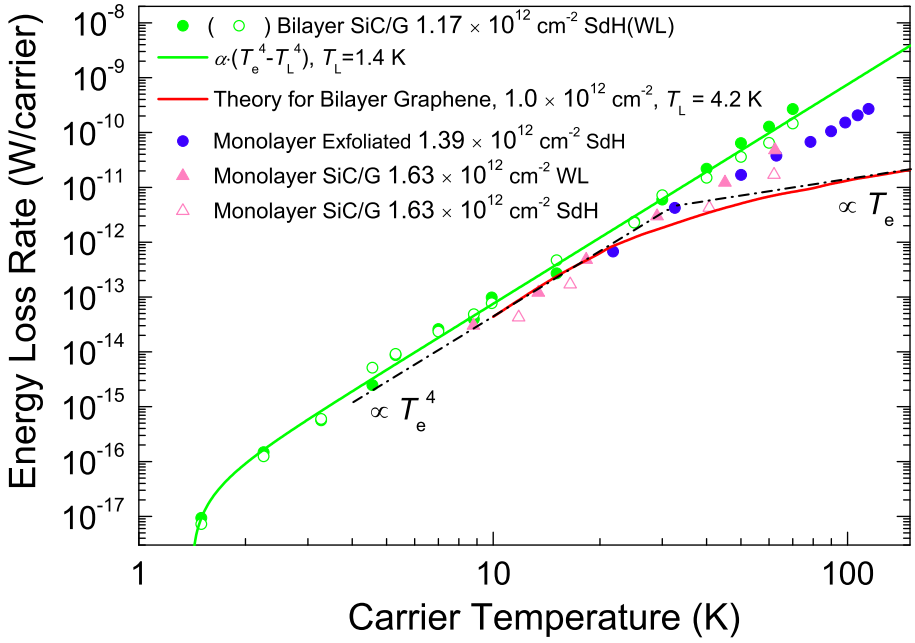

Figure 6.7: Energy loss rate per charge carrier as a function of carrier temperature for bilayer epitaxial graphene (green circles) with $n_e = 1.17\times10^{12}$ cm^{-2} measured using both SdH and WL techniques. The energy loss rates are well fitted by the T^4 power law shown as the green curve. The red curve is the theoretical prediction from Kubakaddi [11] for energy loss due to acoustic phonons. The dash-dot lines signify the T^4 dependence at low temperatures and the linear-T dependence at very high temperatures. Also shown, for comparison, are the energy loss rates of monolayer graphene with similar carrier densities [6, 7].

and

$$F(T) = \frac{m^{*2}D^2(k_BT)^4 3!\zeta(4)}{\pi^{5/2}n_e^{3/2}\rho\hbar^3(\hbar v_s)^3} = \alpha T^4, \tag{6.6}$$

where D is the deformation potential constant, $\zeta(4)$ is the Riemann zeta function, ρ is the areal mass density, and v_s is acoustic wave velocity. The theory has an $n_e^{-1.5}$ dependence of α, which matches our experimental results very well for the carrier density dependent α using Equation 6.6 (Figure 6.8 inset). We emphasise that this $n_e^{-1.5}$ dependence in bilayer graphene, due to its parabolic dispersion relation at low energies [11], is very different from the $n_e^{-0.5}$ dependence for monolayer graphene which has been theoretically predicted [14] and already experimentally observed [6]. As a comparison, the carrier

density dependence of α in monolayer graphene is plotted in the same figure. Below the crossing point corresponding to a carrier density of approximately 1.86×10^{12} cm^{-2} and at carrier temperatures between 1.4 and 100 K, hot carriers in bilayer graphene will be able to lose energy faster than those in monolayer and vice versa. This therefore explains the power loss difference shown in Figure 6.7 both qualitatively and quantitatively. It also suggests a higher tunability in the power loss behaviour of bilayer graphene by controlling the carrier density, and could potentially become an important criterion to consider especially for applications where either higher (e.g. ultra-fast electronics) or lower (e.g. photo-thermoelectric detectors) energy loss rates are favoured. In addition, the above fittings give a deformation potential constant of 22 eV for our bilayer epitaxial graphene, which is very close to the value used in theoretical studies [11–13] and falls in the relatively broad range ($10 - 50$ eV) found in the literature [33–36].

It is worth pointing out that the theoretically predicted range in which the T^4 power law is valid extends only up to about 20 K before slowing to approach the high-temperature limit of a linear temperature dependence (red curve and dash-dot lines in Figure 6.7). Our results, on the other hand, demonstrate a much wider carrier temperature range up to at least 80 K for the T^4 dependence. The BG temperatures (T_{BG}) corresponding to the three carrier densities for our bilayer graphene are calculated to be 83 K, 114 K and 161 K, suggesting the T^4 dependence has not been altered even as the electron temperature approaches T_{BG}. This is not commonly seen in conventional 2DEG [37–39], however, very similar behaviour has already been observed in monolayer graphene in a number of experimental studies [6, 40–42]. One explanation for this are additional cooling pathways, due to disorder-assisted electron-phonon interaction know as "supercollisions" [43] which has been proposed for monolayer graphene, leading to a gradual transition where the energy loss rate changes to a T^3 dependence [40, 41] between the BG regime and the high-temperature regime. So far, no theoretical extension of the "supercollisions" to bilayer graphene has been reported and our results show

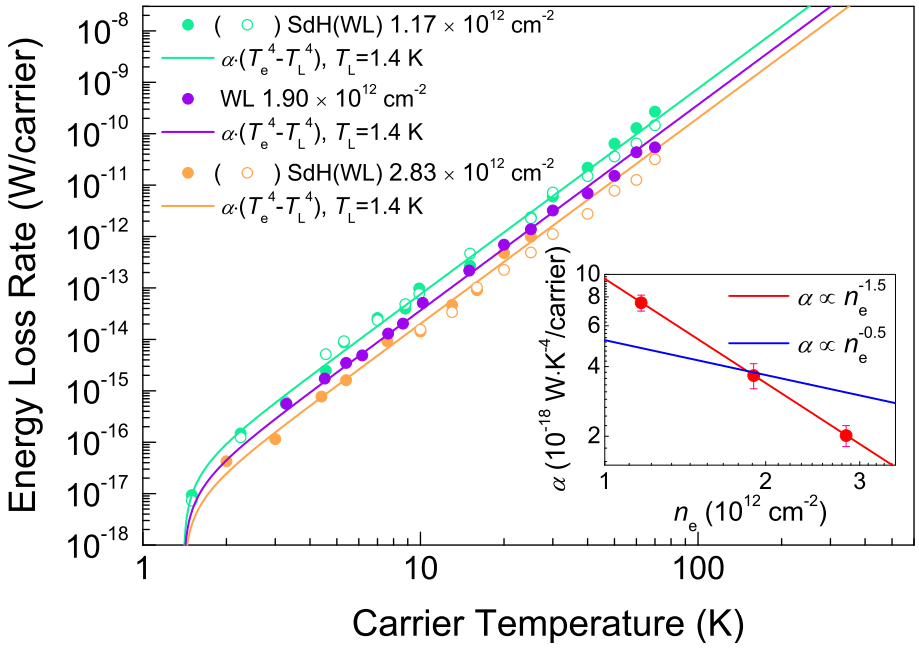

Figure 6.8: Energy loss rate per carrier versus carrier temperature for bilayer graphene with different carrier densities. Fitted curves are using Equation 6.5 with α as the fitting parameter. Inset shows the $n_e^{-1.5}$ dependence (red line) of α in bilayer graphene, theoretically predicted by Kubakaddi [11] with a deformation potential constant of 22 eV. The blue line in the inset is the $n_e^{-0.5}$ dependence [6, 14] for monolayer graphene. A crossing point at $n_e \approx 1.86 \times 10^{12}$ cm^{-2} is clearly observed between the bilayer and monolayer dependences.

no evidence of the transition to a T^3 dependence as observed in monolayer graphene. Another possible cooling mechanism to retain the energy loss rate increasing as T^4 in a substrate supported bilayer graphene sample could be the interaction between hot electrons and surface polar phonons (SPPs) [11–13], combined with hot phonon effects which occur when the hot phonon decay rate is not as fast as the phonon emission rate. However, theoretical calculations based on a SiC substrate suggest the contribution from SPPs can only be clearly observed for electron temperatures higher than 100 K [13], due to the relatively low dielectric constant and high surface polar phonon energies of SiC, compared with substrates such as HfO_2. As a result, more theoretical attention and comparable experimental work on this could prove fruitful. For application purposes, this wide temperature range $(2-80$ K) of the T^4 dependence may also be advantageous

for hot-electron detectors operating at liquid-helium to liquid-nitrogen temperatures.

6.3.4 Electron-phonon relaxation time

Another important factor characterising the hot carrier dynamics is the electron-phonon relaxation time, τ_{el-ph} (also often referred to as the energy loss time). The energy loss time at low temperatures can be generally deduced from the energy loss rate P using the Mott formula through energy balance equations [14]

$$\tau_{el-ph} = \frac{\pi^2 k_B^2 (p+1) (T_e^2 - T_L^2)}{6 E_F P}, \tag{6.7}$$

where p is a constant taking the value of ~1.0 for monolayer and bilayer graphene [12]. The energy loss time can therefore be plotted as a function of carrier temperature for the three different carrier densities shown in Figure 6.9. Also shown for comparison is the determined τ_e for monolayer graphene of various synthesis methods and a wide range of carrier density from the reported energy loss rates [6, 7] using Equation 6.7.

Through substitution of the energy loss rate given by Equation 6.4, the energy loss time is expected to take the form

$$\tau_{el-ph} = \frac{\pi^2 k_B^2 (p+1)}{6 \alpha E_F (T_e^2 + T_L^2)} + \tau_0. \tag{6.8}$$

where a limiting phonon relaxation time τ_0 is added to account for the hot phonon and other high-order effects at high temperatures [7, 44]. Very good agreement between our experimental results and Equation 6.8 has been observed as shown in Figure 6.9 for both the bilayer and previously reported [6, 7] monolayer graphene. One obvious difference between the bilayer and monolayer cases is that the energy loss time significantly depends on the carrier density in bilayer graphene even though the change in carrier density is only a factor of 2.4. On the contrary, for the monolayer case, the carrier temperature

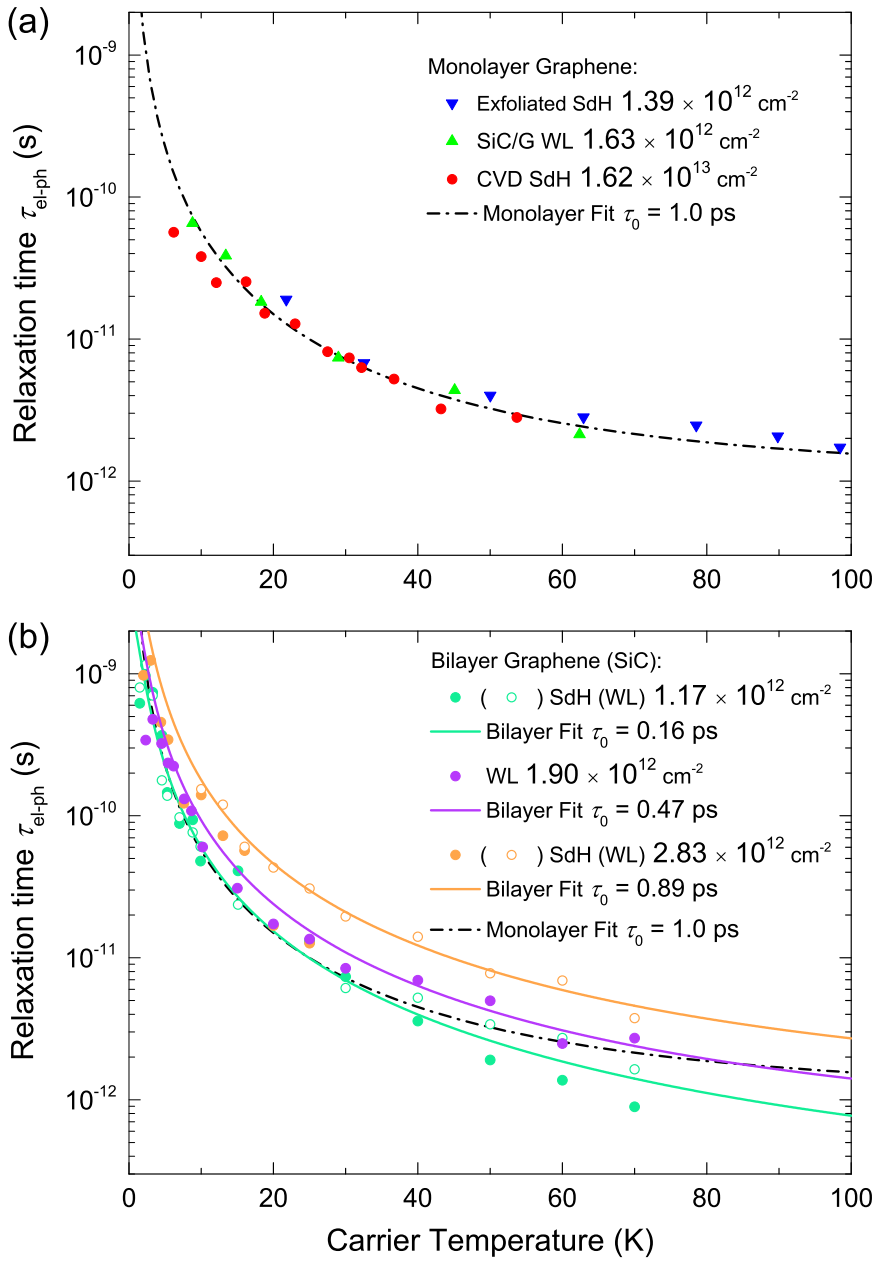

Figure 6.9: Relaxation time of electron-phonon scattering as a function of carrier temperature between 1.4 to 100 K. Data shown are deduced from Equation 6.7 (a) for monolayer graphene with carrier densities spanning over more than an order of magnitude, as well as (b) for bilayer epitaxial graphene with the measured three carrier densities. Fitted lines are using Equation 6.8 with different phonon relaxation times τ_0.

dependence of τ_{el-ph} seems unchanged for a carrier density variation of over an order of magnitude as shown in Figure 6.9a. This can be partly explained from Equation 6.8 by noticing that both the scaling factor α and the Fermi level E_F are carrier density

dependent. In bilayer graphene, $\alpha \propto n_e^{-1.5}$ [11] and $E_F \propto n_e$, resulting in τ_{el-ph} having a net carrier density dependence of $n_e^{0.5}$ at low temperatures. However, in monolayer graphene due to its massless Dirac fermions, $\alpha \propto n_e^{-0.5}$ [6, 14] and $E_F \propto n_e^{0.5}$ [45], leaving αE_F constant over a wide range of n_e.

Another contribution to the observed strong carrier density dependence of τ_{el-ph} could be from a carrier density dependence of τ_0, as shown in Figure 6.9b. Changing the value of τ_0 affects the shape of the fitting curves more significantly at temperatures above 50 K, consistent with its role in limiting the energy loss rate due to high temperature effects, as discussed above. In addition to its carrier density dependence, τ_0 is predicted to be sensitive to the size of the sample, defects inside the lattice and also edge roughness of the graphene [46]. Characterising all the above factors would require sophisticated analysis from measurements on better controlled samples at higher carrier temperatures. Given that the values used in our fits are all within the normal range appearing in the literature [7, 44, 47–50], we would for now only consider τ_0 as a carrier density dependent parameter, which enhances the overall carrier density dependence of τ_{el-ph}.

Thus, the strong carrier density dependence of the electron-phonon relaxation time in bilayer graphene suggests that even faster energy relaxation can be achieved at low carrier densities, which is very important for ultra-fast electronics and high-speed communications, as well as for quantum Hall metrology where it plays an important role in limiting the breakdown current [51]. On the other hand, for some applications, slower electron-phonon relaxation times are preferred for operation. An example of this kind would be detectors based on the photo-thermoelectric effect (PTE). The responsivity of PTE at a given input power directly depends on the resulted carrier temperature [52], and thus can be significantly enhanced by longer energy loss time, which, as has been shown, can be easily achieved in bilayer graphene by increasing its carrier density within certain limits. A long energy loss time also suggests a long cooling length [52], which would be beneficial to large area PTE devices, or allows higher operating temperatures

using bilayer graphene.

6.4 Summary

In summary, hot carrier relaxation characteristics in epitaxially grown bilayer graphene have been experimentally studied by magnetotransport measurements. Both the SdH and WL techniques have been demonstrated to give consistent results. Energy loss rates in bilayer graphene have been found to follow a T^4 dependence for carrier temperatures from 1.4 up to about 100 K, and increase with decreasing carrier density as $n_e^{-1.5}$. The electron-phonon relaxation time has also been observed to be carrier density dependent. These behaviours are in good agreement with the theory [11] accounting for electron scattering due to acoustic phonons at low temperatures. At temperatures above 20 K, the energy loss rates have shown to be much higher than are predicted, with no evidence of approaching the high-temperature linear-T dependence, indicating contributions from other possible cooling mechanisms in this intermediate temperature range, such as the supercollision mechanism [43], which has not been explored for bilayer graphene.

Comparisons have been made between bilayer and monolayer graphene. A stronger carrier density dependence ($n_e^{-1.5}$ vs $n_e^{-0.5}$) of the energy loss rate has been confirmed in bilayer graphene, resulting in a crossover point at $n_e \approx 1.86 \times 10^{12}$ cm^{-2} for energy loss in the two systems. The strong carrier density dependence of τ_{el-ph} in the bilayer is also in contrast with the carrier density independent behaviour in the monolayer. These relations can thus provide us with higher tunability of the electron-phonon interactions and the possibility to achieve even faster/slower energy loss for more efficient hot-carrier applications using bilayer graphene.

Bibliography

[1] K. S. Novoselov, A. K. Geim, S. Morozov, D. Jiang, Y. Zhang, S. V. Dubonos, I. V. Grigorieva, and A. A. Firsov, Science **306**, 666 (2004).

[2] K. S. Novoselov, A. K. Geim, S. V. Morozov, D. Jiang, M. I. Katsnelson, I. V. Grigorieva, S. V. Dubonos, and A. A. Firsov, Nature **438**, 197 (2005).

[3] Y. Zhang, Y.-W. Tan, H. L. Stormer, and P. Kim, Nature **438**, 201 (2005).

[4] K. S. Novoselov, V. I. Fal'ko, L. Colombo, P. Gellert, M. Schwab, and K. Kim, Nature **490**, 192 (2012).

[5] A. Tzalenchuk, S. Lara-Avila, A. Kalaboukhov, S. Paolillo, M. Syväjärvi, R. Yakimova, O. Kazakova, T. J. B. M. Janssen, V. Fal'ko, and S. Kubatkin, Nat. Nanotechnol. **5**, 186 (2010).

[6] A. M. R. Baker, J. A. Alexander-Webber, T. Altebaeumer, S. D. McMullan, T. J. B. M. Janssen, A. Tzalenchuk, S. Lara-Avila, S. Kubatkin, R. Yakimova, C.-T. Lin, L.-J. Li, and R. J. Nicholas, Phys. Rev. B **87**, 045414 (2013).

[7] A. M. R. Baker, J. A. Alexander-Webber, T. Altebaeumer, and R. J. Nicholas, Phys. Rev. B **85**, 115403 (2012).

[8] Y. Ma, R. Fletcher, E. Zaremba, M. D'Iorio, C. T. Foxon, and J. J. Harris, Phys. Rev. B **43**, 9033 (1991).

[9] J. A. Alexander-Webber, A. M. R. Baker, P. D. Buckle, T. Ashley, and R. J. Nicholas, Phys. Rev. B **86**, 045404 (2012).

[10] Y. Zhang, T.-T. Tang, C. Girit, Z. Hao, M. C. Martin, A. Zettl, M. F. Crommie, Y. R. Shen, and F. Wang, Nature **459**, 820 (2009).

[11] K. S. Bhargavi and S. S. Kubakaddi, Physica E **56**, 123 (2014).

[12] K. S. Bhargavi and S. S. Kubakaddi, Physica E **52**, 116 (2013).

[13] V. S. Katti and S. S. Kubakaddi, J. Appl. Phys. **113**, 063705 (2013).

[14] S. S. Kubakaddi, Phys. Rev. B **79**, 075417 (2009).

[15] L. O. Nyakiti, V. D. Wheeler, N. Y. Garces, R. L. Myers-Ward, C. R. Eddy, and D. K. Gaskill, MRS Bull. **37**, 1149 (2012).

[16] G. G. Jernigan, T. J. Anderson, J. T. Robinson, J. D. Caldwell, J. C. Culbertson, R. Myers-Ward, A. L. Davidson, M. G. Ancona, V. D. Wheeler, L. O. Nyakiti, A. L. Friedman, P. M. Campbell, and D. K. Gaskill, J. Vac. Sci. Technol., B **30**, 03D110 (2012).

[17] T. Yager, A. Lartsev, S. Mahashabde, S. Charpentier, D. Davidovikj, A. Danilov, R. Yakimova, V. Panchal, O. Kazakova, A. Tzalenchuk, S. Lara-Avila, and S. Kubatkin, Nano Lett. **13**, 4217 (2013).

[18] S. Lara-Avila, K. Moth-Poulsen, R. Yakimova, T. Bjørnholm, V. Fal'ko, A. Tzalenchuk, and S. Kubatkin, Adv. Mater. **23**, 878 (2011).

[19] A. Lartsev, T. Yager, T. Bergsten, A. Tzalenchuk, T. J. B. M. Janssen, R. Yakimova, S. Lara-Avila, and S. Kubatkin, Appl. Phys. Lett. **105**, 063106 (2014).

[20] G. Stoger, G. Brunthaler, G. Bauer, K. Ismail, B. Meyerson, J. Lutz, and F. Kuchar, Semicond. Sci. Tech. **9**, 765 (1994).

[21] I. M. Lifshitz and A. M. Kosevich, Sov. Phys. JETP **2**, 636 (1956), [1955 *Zh. Eksp. Teor. Fiz.* **29** 730].

[22] K. S. Novoselov, E. McCann, S. V. Morozov, V. I. Fal'ko, M. I. Katsnelson, U. Zeitler, D. Jiang, F. Schedin, and A. K. Geim, Nat. Phys. **2**, 177 (2006).

[23] G. M. Rutter, S. Jung, N. N. Klimov, D. B. Newell, N. B. Zhitenev, and J. A. Stroscio, Nat. Phys. **7**, 649 (2011).

[24] M. Koshino and T. Ando, Phys. Rev. B **73**, 245403 (2006).

[25] K. Zou, X. Hong, and J. Zhu, Phys. Rev. B **84**, 085408 (2011).

[26] A. F. Garcia-Flores, H. Terashita, E. Granado, and Y. Kopelevich, Phys. Rev. B **79**, 113105 (2009).

[27] F. V. Tikhonenko, D. W. Horsell, R. V. Gorbachev, and A. K. Savchenko, Phys. Rev. Lett. **100**, 056802 (2008).

[28] R. Fletcher, J. J. Harris, C. T. Foxon, and R. Stoner, Phys. Rev. B **45**, 6659 (1992).

[29] P. A. Lee and T. V. Ramakrishnan, Rev. Mod. Phys. **57**, 287 (1985).

[30] A. M. R. Baker, J. A. Alexander-Webber, T. Altebaeumer, T. J. B. M. Janssen, A. Tzalenchuk, S. Lara-Avila, S. Kubatkin, R. Yakimova, C.-T. Lin, L.-J. Li, and R. J. Nicholas, Phys. Rev. B **86**, 235441 (2012).

[31] R. Leturcq, D. L'Hôte, R. Tourbot, V. Senz, U. Gennser, T. Ihn, K. Ensslin, G. Dehlinger, and D. Grützmacher, Europhys. Lett. **61**, 499 (2003).

[32] R. Fletcher, V. M. Pudalov, Y. Feng, M. Tsaousidou, and P. N. Butcher, Phys. Rev. B **56**, 12422 (1997).

[33] K. M. Borysenko, J. T. Mullen, X. Li, Y. G. Semenov, J. M. Zavada, M. B. Nardelli, and K. W. Kim, Phys. Rev. B **83**, 161402 (2011).

[34] J. K. Viljas and T. T. Heikkilä, Phys. Rev. B **81**, 245404 (2010).

[35] E. H. Hwang and S. Das Sarma, Phys. Rev. Lett. **101**, 156802 (2008).

[36] E. H. Hwang and S. Das Sarma, Phys. Rev. B **75**, 205418 (2007).

[37] H. L. Stormer, L. N. Pfeiffer, K. W. Baldwin, and K. W. West, Phys. Rev. B **41**, 1278 (1990).

[38] C. E. Martinez, N. M. Stanton, A. J. Kent, M. L. Williams, I. Harrison, H. Tang, J. B. Webb, and J. A. Bardwell, Semicond. Sci. Tech. **21**, 1580 (2006).

[39] Y. Y. Proskuryakov, J. T. Nicholls, D. I. Hadji-Ristic, A. Kristensen, and C. B. Sørensen, Phys. Rev. B **75**, 045308 (2007).

[40] A. C. Betz, S. H. Jhang, E. Pallecchi, R. Ferreira, G. Fève, J.-M. Berroir, and B. Plaçais, Nat. Phys. **9**, 109 (2013).

[41] M. W. Graham, S.-F. Shi, D. C. Ralph, J. Park, and P. L. McEuen, Nat. Phys. **9**, 103 (2013).

[42] A. C. Betz, F. Vialla, D. Brunel, C. Voisin, M. Picher, A. Cavanna, A. Madouri, G. Fève, J.-M. Berroir, B. Plaçais, and E. Pallecchi, Phys. Rev. Lett. **109**, 056805 (2012).

[43] J. C. W. Song, M. Y. Reizer, and L. S. Levitov, Phys. Rev. Lett. **109**, 106602 (2012).

[44] M. Breusing, C. Ropers, and T. Elsaesser, Phys. Rev. Lett. **102**, 086809 (2009).

[45] E. H. Hwang, S. Adam, and S. Das Sarma, Phys. Rev. Lett. **98**, 186806 (2007).

[46] S. S. Kubakaddi and K. S. Bhargavi, Phys. Rev. B **82**, 155410 (2010).

[47] H. Wang, J. H. Strait, P. A. George, S. Shivaraman, V. B. Shields, M. Chandrashekhar, J. Hwang, F. Rana, M. G. Spencer, C. S. Ruiz-Vargas, and J. Park, Appl. Phys. Lett. **96**, 081917 (2010).

[48] T. Kampfrath, L. Perfetti, F. Schapper, C. Frischkorn, and M. Wolf, Phys. Rev. Lett. **95**, 187403 (2005).

[49] X. Zou, D. Zhan, X. Fan, D. Lee, S. K. Nair, L. Sun, Z. Ni, Z. Luo, L. Liu, T. Yu, Z. Shen, and E. E. M. Chia, Appl. Phys. Lett. **97**, 141910 (2010).

[50] K. Kang, D. Abdula, D. G. Cahill, and M. Shim, Phys. Rev. B **81**, 165405 (2010).

[51] J. A. Alexander-Webber, A. M. R. Baker, T. J. B. M. Janssen, A. Tzalenchuk, S. Lara-Avila, S. Kubatkin, R. Yakimova, B. A. Piot, D. K. Maude, and R. J. Nicholas, Phys. Rev. Lett. **111**, 096601 (2013).

[52] N. M. Gabor, J. C. W. Song, Q. Ma, N. L. Nair, T. Taychatanapat, K. Watanabe, T. Taniguchi, L. S. Levitov, and P. Jarillo-Herrero, Science **334**, 648 (2011).

7 Concluding Remarks

This chapter summarises the key findings present in this thesis. It provides an overview of the new knowledge discovered as well as the significance and limitations of the research. Areas for further development and future research are also recommended.

Contents

7.1 Summary of key results

During the course of work for this thesis magnetotransport properties of graphene and its bilayer systems were studied. Devices based on epitaxial graphene grown on silicon carbide were fabricated by developed nanolithography and sample processing techniques, including multi-step electron-beam lithography/photolithography, plasma etching and evaporation processes. Using high field superconducting magnets, cryogenics as well as high-sensitivity electrical measurements, magnetotransport studies in these two-dimensional systems were conducted.

The disorder effects in graphene when the Fermi energy lies in the vicinity of the Dirac point were investigated. It was shown from temperature-dependent Hall effect measurements that the carrier density increases quadratically with temperature. This is in good agreement with theoretical predictions which take into account intrinsic thermal excitation combined with electron-hole puddles present in the system assuming a Gaussian disordered potential landscape. Disorder strengths of the samples studied were deduced in the range $10.2 - 31.2$ meV, depending on the sample treatment. Scattering mechanisms in those samples were investigated. A scattering asymmetry for electrons and holes has been observed and is consistent with theoretical calculations for graphene on SiC substrates due to charged impurities. The impurity density was estimated to be $3.0 - 9.1 \times 10^{10}$ cm^{-2}. It was also shown that the minimum conductivity increases with increasing disorder strength, in good agreement with numerical quantum-mechanical

calculations. It was demonstrated that the application of this method can be used to provide a simple and effective route to characterise how clean a graphene sample is, which is particularly crucial for studies and applications of graphene in the ballistic transport regime. Moreover, it is emphasised that this method can be used for quantitatively studying the disorder characteristics not only in graphene but also in other two-dimensional materials.

The magnetic field dependent charge transfer process in epitaxial graphene grown on SiC were investigated from measurements of the breakdown and the temperature dependence of the quantum Hall effect using ultra-high magnetic fields and low density samples. These new measurements showed that the full extent of the $v = 2$ plateau can be observed in this system for low enough starting carrier densities, with the widest quantum Hall plateau observed to date and its associated dissipationless state extending over 50 T. This giant quantum Hall plateau is strong evidence for magnetic field dependent charge transfer from charge reservoirs with exceptionally high densities of states in close proximity to the graphene, giving rise to an almost linear increase in carrier density with magnetic field. The quantum Hall breakdown current was shown to be asymmetrically stretched compared with a symmetric triangular dependence on magnetic field in traditional 2DEG. This effect was used to accurately measure this increase in carrier density with field, which is found to be over an order of magnitude in some cases. Such strong magnetic field dependence of the carrier density was independently confirmed by the temperature dependence of the magneto-conductivity of the samples, fitted by combining thermal activation between extended states in Gaussian broadened Landau levels and variable range hopping. Using a realistic framework of broadened Landau levels, a charge transfer model was proposed, and has been used to extract the densities of donor states, accurately describe characteristics of the field dependent carrier density, and predict its effects on the breakdown of the quantum Hall effect in excellent agreement with experimental results. These results and models (as detailed

in Chapter 5) are widely applicable towards a more comprehensive understanding of the magnetotransport properties of graphene, and can be used to provide a practical guide towards engineering applications such as an epitaxial graphene-based quantum Hall resistance standard.

Hot carrier relaxation characteristics in graphene bilayer systems were investigated independently through analysing the temperature and current dependences of the SdH oscillations and weak localisation. Both methods were demonstrated to provide consistent results. Energy loss rates in graphene bilayer follow a T^4 power-law dependence for carrier temperatures from 1.4 up to about 100 K. The pre-factor of this T^4 dependence scales with carrier density as $n_e^{-1.5}$ in graphene bilayer in contrast to the $n_e^{-0.5}$ dependence in monolayer graphene. This leads to a crossover point at $n_e \approx 1.86 \times 10^{12}$ cm^{-2} for energy loss in the two systems. The electron-phonon relaxation time at fixed electron temperatures in the bilayer system was also found to be strongly carrier density dependent, while it maintains a nearly constant value for a wide range of carrier densities in monolayer graphene. At low temperatures, these behaviours are in good agreement with the theoretical prediction which accounts for electron-acoustic phonon interactions. At temperatures above 20 K, the energy loss rates observed experimentally are much higher than what the theory has predicted, i.e., with no evidence of approaching the linear-T dependence of the high temperature regime. This can be evidence for contributions from other cooling mechanisms which can result in an enhancement of the energy loss rates in this intermediate temperature range, such as the supercollision mechanism, which has been reported in monolayer graphene but yet to be explored for the bilayer system. These results and comparisons exhibit a more complete picture of hot carrier dynamics in graphene and its bilayer systems. It is shown that either faster or slower energy loss can be achieved using bilayer graphene due to its higher tunability of the electron-phonon interactions by adjusting its carrier density, a potentially important factor to contribute to more efficient hot-carrier applications using bilayer graphene.

7.2 Future work and outlook

In pursuit of the above findings several limitations and new questions to the current work have emerged, generating opportunities for promising future work.

Firstly, in the study of disorder effects on epitaxial graphene, the theories and models applied require the condition that the Fermi level lies exactly at the Dirac point, where the electron and hole densities are equal, in order to have the most rigorous description. Experimentally, this can not be easily achieved with our current device structure as the polymer gating techniques used do not allow a continuous and precise tuning of the Fermi level. One can construct a conventional top gate to allow better control. Even so, it is non-trivial to determine the precise position of the Fermi level from the measured field-effect resistance because of the fact that the mobilities of electrons and holes are not necessarily equal, which adds further complications to the problem. Nonetheless, since it is demonstrated that the Fermi level is in the vicinity of the Dirac point, we would expect the errors to be minor. Moreover, in the discussion of the scattering mechanisms and minimum conductivities, for simplicity, only effects from a single species of charged impurities are considered. In practice, the situation could be much more complex, and it is therefore recommended that more experimental studies and systematic comparisons for well-controlled samples with deliberately introduced disorders combined with various imaging techniques would be highly beneficial. Data from similar experiments can be seen in the literature [1, 2], and it would be very interesting to make some comparisons. Unfortunately, it is found that most of the published data are insufficient to be analysed using our approach, and this makes direct comparisons very difficult.

Secondly, in the investigation of charge transfer from SiC to epitaxial graphene, a relatively large density of surface states distributed over a wide energy range was estimated. It is suspected that these states are originated from the defects in the buffer layer. Direct confirmations from photo-emission or scanning tunnelling microscopy studies would

be needed to understand the exact origins and characteristics of these surface states. In addition, on multiple occasions, the analysis in this study has assumed a constant Landau level broadening with a Gaussian shape. While no major difference is expected using different approximated shapes of broadening, the Landau level broadening may be different for different levels and may also depend on magnetic field and temperature as several theoretical and experimental works have reported, even though sometimes the results are found to be contradictory [3–10]. One would expect this knowledge may not be universal for all two-dimensional systems and are strongly related to microscopic details of all disorder characteristics present in the systems, making this question/task even more challenging.

Thirdly, the present study has only considered the hot carrier dynamics in AB-stacked epitaxial graphene bilayer, while other stacking types with various twisting angles may result in completely differently behaviours. Also, different substrates may contribute to unique interactions at the interface, modifying the energy loss characteristics. These areas are all good candidates among the scope of future investigations.

Finally, the main experimental studies present in this thesis are confined within epitaxial graphene and its bilayer system grown on SiC, while it is worth emphasising that most of the methods involved in this thesis are also suitable for different types of graphene, such as CVD grown and exfoliated graphene, as well as many other two-dimensional materials. It would be very interesting to explore them and make comparisons where applicable.

Research centred around graphene and related two-dimensional systems has become one of the most active fields during the last one and half decades, bringing together numerous academic and industrial researchers working collaboratively towards various goals in both fundamental science and real-world applications. Being a wonderful playground for condensed matter physics, despite being extensively explored, graphene and

its related systems will continue to help answer various unsolved problems, especially in quantum Hall physics such as the exact nature of quantum Hall breakdown.

The emergence of other two-dimensional materials has recently evolved this field to a voyage of discovery which couples families of materials and their heterostructures in vast numbers. These heterostructures are not only limited to among two-dimensional crystals but can also be constructed with bulk materials and assemblies of macromolecules, with one interesting example being nanostructures formed by graphene covered with porphyrin nanorings in which a superlattice modulation could potentially allow the observation of the Hofstadter's butterfly.

Stepping forward, in the following years, with substantial breakthroughs, optimisations, and steadily decreasing fabrication costs, the integration of graphene, its related two-dimensional materials and heterostructures is expected to provide multifunctional applications, ranging from electronics, energy solutions to nano-composites and biomedical advancements [11], which are promising to unleash transformational impact on science and technology, at the same time becoming a non-negligible force to help in resolving health, environmental and social issues.

Bibliography

[1] S. Wiedmann, H. J. van Elferen, E. V. Kurganova, M. I. Katsnelson, A. J. M. Giesbers, A. Veligura, B. J. van Wees, R. V. Gorbachev, K. S. Novoselov, J. C. Maan, and U. Zeitler, Phys. Rev. B **84**, 115314 (2011).

[2] E. V. Kurganova, S. Wiedmann, A. J. M. Giesbers, R. V. Gorbachev, K. S. Novoselov, M. I. Katsnelson, T. Tudorovskiy, J. C. Maan, and U. Zeitler, Phys. Rev. B **87**, 085447 (2013).

[3] T. Ando, A. B. Fowler, and F. Stern, Rev. Mod. Phys. **54**, 437 (1982).

[4] R. R. Gerhardts, Surf. Sci. **58**, 227 (1976).

[5] M. E. Raikh and T. V. Shahbazyan, Phys. Rev. B **47**, 1522 (1993).

[6] C. H. Yang, F. M. Peeters, and W. Xu, Phys. Rev. B **82**, 075401 (2010).

[7] H. Funk, A. Knorr, F. Wendler, and E. Malic, Phys. Rev. B **92**, 205428 (2015).

[8] L. Wang and R. F. O'Connell, Phys. Rev. B **37**, 3052 (1988).

[9] L. A. Ponomarenko, R. Yang, R. V. Gorbachev, P. Blake, A. S. Mayorov, K. S. Novoselov, M. I. Katsnelson, and A. K. Geim, Phys. Rev. Lett. **105**, 136801 (2010).

[10] A. J. M. Giesbers, U. Zeitler, M. I. Katsnelson, L. A. Ponomarenko, T. M. Mohiuddin, and J. C. Maan, Phys. Rev. Lett. **99**, 206803 (2007).

[11] Work Package Dissemination, *Graphene Flagship Annual Report 2015*, Tech. Rep. (Graphene Flagship, 2015).

A

Poster Presentations

This appendix includes posters related to the work described in this thesis that have been presented at major international conferences.

Physics of a disordered Dirac point in epitaxial graphene from temperature-dependent magnetotransport measurements

J. Huang[1], J. A. Alexander-Webber[1], T. J. B. M. Janssen[2], A. Tzalenchuk[2,3], V. Antonov[3], T. Yager[4], S. Lara-Avila[4], S. Kubatkin[4], R. Yakimova[5], R. J. Nicholas[1,*]

[1]Department of Physics, University of Oxford, Clarendon Laboratory, Parks Road, Oxford OX1 3PU, United Kingdom
[2]National Physical Laboratory, Hampton Road, Teddington TW11 0LW, United Kingdom
[3]Department of Physics, Royal Holloway, University of London, Egham TW20 0EX, United Kingdom
[4]Department of Microtechnology and Nanoscience, Chalmers University of Technology, S-412 96 Göteborg, Sweden
[5]Department of Physics, Chemistry and Biology (IFM), Linköping University, S-581 83 Linköping, Sweden
*Email: r.nicholas@physics.ox.ac.uk

Read more at Huang *et al.*, Phys. Rev. B 92, 075407 (2015)

I. Introduction

- Electrical transport properties of graphene can be dominated by the effects of disorder when the Fermi energy approaches the Dirac point.
- Recently, epitaxial graphene on SiC (SiC/G) has been shown to have very high quantum Hall breakdown current density [1], which potentially allows a quantum electrical resistance standard operating at even higher T and lower B [2].
- Low and well controlled carrier density is required to achieve high breakdown current in these conditions, and understanding the disorder effects is therefore highly important.
- Using extremely low carrier density SiC/G, we describe the role of disorder in governing the temperature-dependent magnetotransport.

II. Samples and Experimental Methods

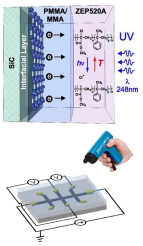

- SiC/G samples were epitaxially grown on the Si-terminated face of 4H-SiC at $T = 2000$ °C and $P = 1$ atm Ar [2].
- 8-leg Hall bars have been fabricated by e-beam lithography followed by O_2 plasma etching and large-area Ti/Au contacting.
- 3 samples were measured, all with bilayer polymer top-gates to tune E_F to the Dirac point by deep UV illumination [3] (Sample UV1) using a 248-nm mercury lamp, or by corona discharge [4] (Sample CD1, CD2) using a piezo-activated antistatic gun.
- DC and AC magnetotransport measurements have been made using an Oxford Instruments 21 T superconducting magnet with a variable temperature insert from 1.4 K up to 300 K.

III. Intrinsic Activation in the Presence of Electron-Hole Puddles

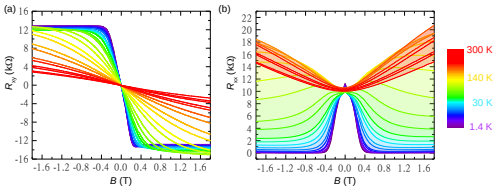

- The Hall resistance R_{xy} and the longitudinal resistance R_{xx} as a function of magnetic field at temperatures from 1.4 K to 300 K (e.g. for sample CD2). The sample enters the quantum Hall regime ($\nu = 2$) already from about 0.6 T at low temperatures.
- Microscopically, the fluctuating electrostatic disorder potential breaks up the intrinsically homogeneous charge distribution into electron-hole puddles.
- At the Dirac point, $n_e = n_h$. The carrier density directly extracted from the low-field Hall coefficients using a two-carrier model is therefore effectively, $n_{eff} = \alpha \cdot n_e$. The pre-factor α is a function of electron/hole mobility ratio (μ_e/μ_h), $\alpha = (\mu_e/\mu_h + 1)/(\mu_e/\mu_h - 1)$.

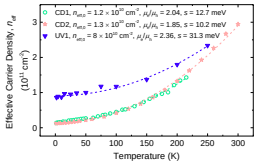

- Quadratic increase of n_{eff} with increasing temperature
- Distinct non-zero residual carrier densities at the low-temperature limit, indicating that the potential landscape is highly inhomogeneous.
- Well modelled by intrinsic excitation combined with disorder-induced electron-hole puddles with a Gaussian potential variation [5],

$$P(V) = \frac{1}{\sqrt{2\pi s^2}} \exp\left(-V^2/2s^2\right)$$

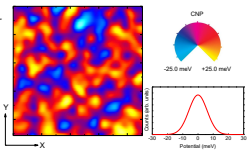

- The disorder strength s and μ_e/μ_h can be extracted from the fittings,

$$n_{eff} = \alpha \cdot \frac{g_s g_v}{2\pi(\hbar v_F)^2}\left[\frac{s^2}{4} + \frac{(\pi k_B T)^2}{12}\right]$$

IV. Disorder Strength of Electron-Hole Puddles in Graphene: Comparisons

Synthesis (Treatment)	*Disorder Strength*	*Probing Method*
Epitaxial on SiC (**CD1**)	**12.7 ± 0.6 meV**	**Magnetotransport**
Epitaxial on SiC (**CD2**)	**10.2 ± 0.4 meV**	**Magnetotransport**
Epitaxial on SiC (**UV1**)	**31.3 ± 2.0 meV**	**Magnetotransport**
Epitaxial on SiC (**AO**) [6]	**15 ± 1 meV**	**Magnetotransport**
Epitaxial on SiC	12 meV	KPM [7]
Exfoliated on SiO_2/Si	50 meV	SET [8]
Exfoliated on SiO_2/Si	~ 20 meV	STM [9]
Exfoliated on h-BN	5.4 meV	STM [10]
CVD on Ir(111)	~ 30 meV	STM/STS [11]

V. Scattering Mechanisms

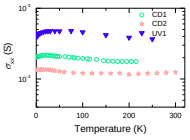

- Conductivity: slowly varying with weak non-monotonic fluctuations for a large range of temperatures
- Mainly due to the temperature-dependent carrier density as described above and the $\mu(T)$ dependence as we will show below
- Electron mobility: well fitted by the combination of impurity scattering, longitudinal acoustic (LA) phonon scattering, and remote interfacial phonon (RIP) scattering at the SiC/graphene interface
- Impurity scattering dominates at low temperatures (< 100 K), RIP scattering dominates at high temperatures
- Unequal electron and hole mobilities: quantitatively in good agreement with charged impurity scattering [12]

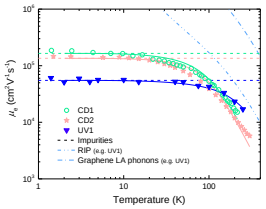

- Charged impurity densities for our SiC/G: 3.0 ~ 9.1 × 10^{10} cm^{-2}, 10 ~ 100 times lower than that in typical exfoliated and CVD grown graphene on SiO2, comparable to that of h-BN supported graphene

VI. Minimum Conductivity of Disordered Graphene

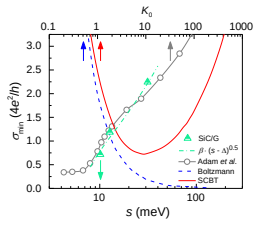

- Minimum conductivity: increasing with increasing disorder strength s, roughly following a $\beta(s - \Delta)^{0.5}$ dependence locally in the (0.5 ~ 2.5) × $4e^2/h$ range
- Qualitatively agrees well with the theoretical predictions [13] from the quantum-mechanical approach, where we assume $s \propto \sqrt{K_0}$ ($K_0 \propto \langle U_C(\mathbf{r})UG(\mathbf{r}')\rangle$), while in contrast to the Boltzmann and the self-consistent Boltzmann theory

VII. Conclusions

- From temperature-dependent magnetotransport measurements on epitaxial graphene, we have demonstrated the disorder effects when the Fermi energy lies in the vicinity of the Dirac point, and have been able to identify the main origin of those effects to be charged impurities.
- The disorder strength and the impurity densities of our samples have been estimated from experimental results.
- The minimum conductivity increases with increasing disorder strength, in good agreement with numerical quantum-mechanical calculations.
- Overall, the application of this method can, therefore, provide an alternative and effective route for quantitatively studying the disorder characteristics in graphene and other 2D materials.

References: **[1]** Alexander-Webber *et al.*, PRL **111**, 096601 (2013); **[2]** Tzalenchuk *et al.*, Nat. Nanotechnol. **5**, 186 (2010); **[3]** Lara-Avila *et al.*, Adv. Mater. **23**, 878 (2011); **[4]** Lartsev *et al.*, APL **105**, 063106 (2014); **[5]** Li *et al.*, PRB **84**, 115442 (2011); **[6]** Yager *et al.*, APL **106**, 063503 (2015); **[7]** Curtin *et al.*, APL **98**, 243111 (2011); **[8]** Martin *et al.*, Nat. Phys. **4**, 144 (2008); **[9]** Zhang *et al.*, Nat. Phys. **5**, 722 (2009); **[10]** Xue *et al.*, Nat. Mater. **10**, 282 (2011); **[11]** Martin *et al.*, PRB **91**, 041406 (2015); **[12]** Novikov, APL **91**, 102102 (2007); **[13]** Adam *et al.*, PRB **79**, 201404 (2009).
Acknowledgments: This work was supported by the U.K. EPSRC and NMS, E.U. Graphene Flagship (Contract No. CNECT-ICT-604391), and EMRP GraphOhm, the Swedish Foundation for Strategic Research (SSF), Linnaeus Centre for Quantum Engineering, Knut and Alice Wallenberg Foundation and Chalmers AoA Nano.

Figure A.1: Poster presented at the 21st International Conference on Electronic Properties of Two-Dimensional Systems (EP2DS-21), during 26 – 31 July 2015, in Sendai, Japan.

Giant quantum Hall plateaus generated by charge transfer in epitaxial graphene

J. A. Alexander-Webber,[1] J. Huang,[1] D. K. Maude,[2] T. J. B. M. Janssen,[3] A. Tzalenchuk,[3,4] V. Antonov,[4] T. Yager,[5] S. Lara-Avila,[5] S. Kubatkin,[5] R. Yakimova,[6] and R. J. Nicholas[1,*]

[1]Department of Physics, University of Oxford, Oxford, United Kingdom
[2]Laboratoire National des Champs Magnétiques Intenses, Toulouse, France
[3]National Physical Laboratory, Teddington, United Kingdom
[4]Department of Physics, Royal Holloway, University of London, Egham, United Kingdom
[5]Department of Microtechnology and Nanoscience, Chalmers University of Technology, Göteborg, Sweden
[6]Department of Physics, Chemistry and Biology (IFM), Linköping University, Linköping, Sweden

Open access at Sci. Rep. 6, 30296 (2016). doi:10.1038/srep30296

1. Introduction

- Epitaxial graphene grown on SiC (SiC/G), one of the best candidates for the next generation of quantum resistance metrology applications[1,2], can maintain a quantum Hall (QH) state up to critical current densities more than 30 times larger than previously observed in other material systems[3].
- In SiC/G, charge transfer from the underlying substrate leads to a strongly magnetic field dependent carrier density $n(B)$ and an exceptionally wide quantised $\nu = 2$ plateau[4]. Experimental data in which the full extent of $n(B)$ can be measured is crucial in obtaining a complete understanding of this process.
- Using a combination of high magnetic fields (HMF) and ultra-low carrier density samples we present here the first detailed study of the full magnetic field dependence of the charge transfer process which underpins the benefits of graphene in quantum metrology.

2. Samples and Experimental Setup

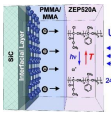

- SiC/G samples grown on the Si-terminated face of 4H-SiC at T = 2000 °C and P = 1 atm Ar[4]
- 8-leg Hall bars by e-beam lithography followed by O_2 plasma etching and large-area Ti/Au contacting
- Bilayer polymer top-gates to tune E_F by deep UV illumination[5] or by corona discharge[6]
- Steady field measurements using an Oxford Instruments 21 T superconducting magnet from 1.4 up to 300 K with a variable temperature insert
- Pulsed magnetic fields of up to 57 T provided by a 19 kV long pulse magnet at the LNCMI-Toulouse

3. Breakdown of the quantum Hall effect in ultra-low carrier density epitaxial graphene

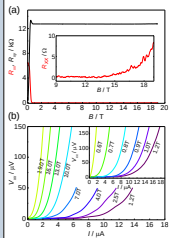

- In a sample with $n_0 = 1.5 \times 10^{10}$ cm^{-2} (at $B = 0$), the full $\nu = 2$ QH state is observed, from 0.7 T up to 14 T.
- Upon increasing the current density above a critical value j_c, a sudden onset of longitudinal resistance indicates the breakdown of the QHE.
- In traditional 2DEG, where the carrier density is constant, j_c has a symmetric triangular dependence on both filling factor and magnetic field[7,8], i.e. $j_c(B) = j_c^{max}\left(1 - \frac{|\nu-2|}{\delta\nu}\right)$, where $0.2 < \delta\nu < 0.3$ typically, and $\nu = nh/eB$.
- In SiC/G, the triangular dependence is asymmetrically stretched indicating n is strongly magnetic field dependent. Using the above formula, $n(B)$ can be calculated from $j_c(B)$.

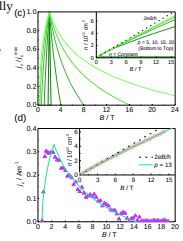

- We also propose a phenomenological expression for the field dependent carrier density, which rapidly swaps over from a value n_0 at low field to a slightly sublinear increase with field $\propto B^{1-\frac{1}{p}}$, for large p,

$$n(B) = \frac{2eB}{h}\left[\left(\frac{B_0}{B}\right)^p + \frac{B_0}{B}\right]^{1/p}, \quad (1)$$

where $B_0 = \frac{n_0 h}{2e}$, and $j_c = j_c^{max}$ at B_c.

- Using $p = 13$, excellent fits are obtained for both n and j_c, corresponding to a plateau $\nu = 2 \pm 0.26$ (see Sec. 4).

4. Determining the field dependence of E_F

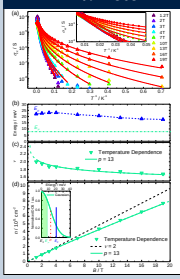

- Temperature dependent magneto-conductivity is well fitted by combining thermal activation between extended states in Gaussian broadened Landau levels and variable range hopping.
- E_F as a function of magnetic field, slowly decreasing to the mobility edge E_μ, is obtained from the fitting.
- $\nu(B)$ and $n(B)$ are therefore deduced.
- The width of the $\nu = 2$ plateau is determined to be $\delta\nu = \pm 0.26$.
- $n(B)$ from the temperature dependence analysis is in good agreement with the QH breakdown analysis, giving $p = 13$.

5. Pulsed field measurements of a 50 T wide $\nu = 2$ plateau

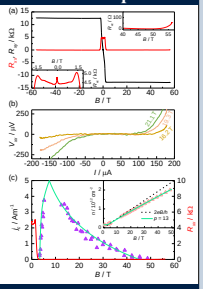

- At $n_0 = 1.5 \times 10^{11}$ cm^{-2}, the $\nu = 2$ QH state extends to 50 T, measured using a constant current of 3 μA in a 57 T long pulse magnet.
- QH breakdown measurements were made using a 107 Hz alternating current source and digital oscilloscope with a sampling rate of 1 MHz.
- No visible hysteresis is observed in both a rapid sinusoidal upsweep (50 ms) and a slower downsweep with an exponential decay constant of 100 ms.
- The field dependence of j_c and n are again well described by Eq. (1) in Sec. 3 with $p = 13$.

6. Overview of samples

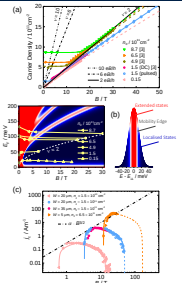

- More samples with n_0 spanning almost three orders of magnitude are studied.
- $n(B)$ in the $\nu = 2$ regime for all samples are in excellent agreement with Eq. (1) with $p = 13$.
- The chemical potential is falling very slowly with increasing magnetic field.
- These results suggest the presence of charge reservoirs in close proximity to the graphene with exceptionally high DOS in the order of 10^{14} cm^{-2}eV^{-1}.
- Over a wide range of magnetic fields, $j_c \propto B^{3/2}$ is observed.

7. Modelling the magnetic field dependent charge transfer

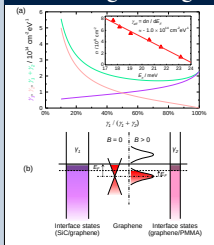

- The magnetic field dependent charge transfer is modelled between the interface states[4,10] and disorder broadened Landau levels.
- DOS of surface donor states for the SiC/graphene interface ($\gamma_1 \sim 0.8 - 1.7 \times 10^{14}$ cm^{-2}eV^{-1}) and the graphene/PMMA interface ($\gamma_2 \sim 0.3 - 1.3 \times 10^{14}$ cm^{-2}eV^{-1}) are estimated.

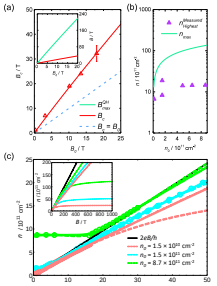

- Our model predicts B_c in excellent agreement with our experimental data. The magnetic field, B_{max}^{QH}, corresponding to the end of the $\nu = 2$ plateau is also predicted.
- The maximum carrier density that can be transferred into graphene, n_{max}, representing the upper limit to the possible validity of the phenomenological Eq. (1), is also calculated.
- A complete $n(B)$ for a Gaussian broadening[11] is numerically calculated, in comparison with our experimental data and Eq. (1).

7. Conclusions

- We have studied the breakdown and the temperature dependence of the QHE using HMF and ultra-low density SiC/G. We have demonstrated the full width of the $\nu = 2$ plateau and the very large extent of $n(B)$, which can be accurately determined from QH breakdown measurements.
- Our model and results show some of the most important features of the field dependent charge transfer process and its effects on the QH breakdown, thus are widely applicable towards a broader and deeper understanding of HMF transport properties of graphene and are crucial for engineering SiC/G devices for applications such as QH metrology.

*Email: r.nicholas1@physics.ox.ac.uk
Notes/References: 1. Tzalenchuk et al., Nat. Nanotechnol. 5, 186 (2010); 2. Janssen et al., 2D Mater. 2, 035015 (2015); 3. Alexander-Webber et al., Phys. Rev. Lett. 111, 096601 (2013); 4. Janssen et al., Phys. Rev. B 83, 233402 (2011); 5. Lara-Avila et al., Adv. Mater. 23, 878 (2011); 6. Lartsev et al., Appl. Phys. Lett. 105, 063106 (2014); 7. Iizuka et al., Physica E 6, 132 (2000); 8. Jeckelmann et al., Rep. Prog. Phys. 64, 1603 (2001); 9. Alexander-Webber et al., Phys. Rev. B 86, 045404 (2012); 10. Takase et al., Phys. Rev. B 86, 165435 (2012); 11. Huang et al., Phys. Rev. B 92, 075407 (2015).
Acknowledgments: This work was supported by the UK EPSRC, the Graphene Flagship contract No. CNECT-ICT-604391, the EMRP project GraphOhm, AFRL grant FA9550-15-C-0067 and the LNCMI-CNRS, member of the European Magnetic Field Laboratory (EMFL), and the International Collaborative Energy Technology R&D Program of the Korean Institute of Energy Technology Evaluation and Planning (KETEP) with financial resource from the Ministry of Trade, Industry & Energy, Republic of Korea (no. 20148520011250). The authors would like to thank Thomas Seyller for useful discussions.

Figure A.2: Poster presented at the 33rd International Conference on the Physics of Semiconductors (ICPS), during 31 July – 5 August 2016, in Beijing, China. (*Best Poster Award.*)

Hot carrier relaxation of Dirac fermions in bilayer epitaxial graphene

J. Huang[1], J. A. Alexander-Webber[1], T. J. B. M. Janssen[2], A. Tzalenchuk[2,3], T. Yager[4], S. Lara-Avila[4], S. Kubatkin[4], R. L. Myers-Ward[5], V. D. Wheeler[5], D. K. Gaskill[5], R. J. Nicholas[1,*]

[1]Department of Physics, University of Oxford, Clarendon Laboratory, Parks Road, Oxford OX1 3PU, United Kingdom
[2]National Physical Laboratory, Hampton Road, Teddington TW11 0LW, United Kingdom
[3]Department of Physics, Royal Holloway, University of London, Egham TW20 0EX, United Kingdom
[4]Department of Microtechnology and Nanoscience, Chalmers University of Technology, S-412 96 Göteborg, Sweden
[5]U.S. Naval Research Laboratory, 4555 Overlook Avenue SW, Washington D.C. 20375, USA

Read more at JPCM 27, 164202 (2015)

1. Introduction

- Hot carrier dynamics in graphene has considerable importance in determining the performance of high frequency and high power electronics, high-speed sensors, thermal management of electronic devices, and quantum Hall metrology for accurate measurements under higher temperature and current conditions.
- **Monolayer graphene:** very high energy loss rates[1,2], electron-phonon relaxation times an order of magnitude shorter than conventional 2DEGs, the lack of a bandgap limiting its potential applications
- **Bilayer graphene:** small energy gaps can be opened[3] and continuously tuned by an external electric field, allowing more control and flexibility for technological purposes. Energy loss rates for hot carriers have been theoretically[4-6] explored but to date this has yet to be studied in significant detail experimentally.

2. Samples and Experimental Setup

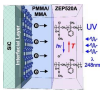

- Bilayer graphene was synthesized epitaxially[7] on (0001) 6H-SiC. Film thickness was determined by XPS[8] and optical transmission[9] measurements.
- 8-leg Hall bars have been fabricated by e-beam lithography. Non-volatile photochemical gating[10] and a corona discharge method[11] were used to control the carrier density.

- DC transport measurements have been made using an Oxford Instruments 21T superconducting magnet with a variable temperature insert from 1.4K up to 100K.

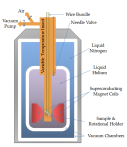

3. Shubnikov-de Haas Oscillations and Effective Mass of Electrons in Bilayer Graphene

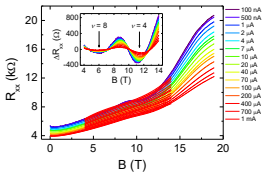

- Resistance minima corresponding to filling factors of 4 and 8
- SdH oscillations strongly damped by increasing input current or ambient temperature

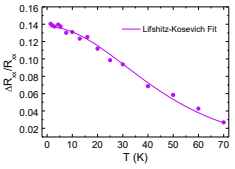

- The effective mass of electrons in bilayer graphene: $0.033m_e$ (for an electron density of 2.83×10^{12} cm^{-2})

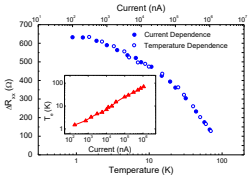

- Electron temperature as a function of applied current obtained by comparing the damped amplitudes of the SdH oscillations from the current and temperature dependences

4. Weak Localization

- WL peak height significantly suppressed by increasing current (at a low fixed temperature) or ambient temperature (at a small fixed current)

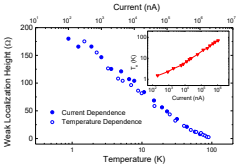

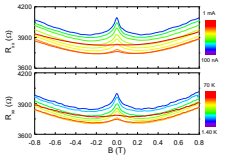

- Similar to the SdH method, comparison of the suppressed values between these two dependences generates a second measure of the carrier temperature as a function of applied current

5. Energy Loss Rates in Bilayer Graphene

- Consistent energy loss rates from both the SdH and WL techniques
- T^4 power law in bilayer graphene
- Well described by the theory[4] considering the electron-acoustic phonon interactions in the low-temperature Bloch-Grüneisen regime
- Much wider carrier temperature range (up to at least 80 K) than predicted for the T^4 dependence suggesting additional cooling pathways

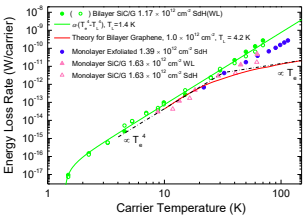

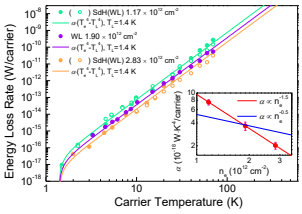

- The energy loss rates in bilayer graphene is found to have a carrier density dependence of $n^{1.5}$ rather than $n^{0.5}$ in the monolayer.
- Crossover point at 1.86×10^{12} cm^{-2}
- Higher tunability in the power loss behaviour of bilayer graphene by controlling the carrier density
- Important for applications where either higher or lower energy loss rates are favoured

6. Electron-phonon Relaxation Time

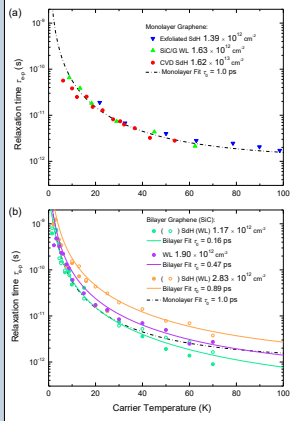

- The electron-phonon relaxation time is well fitted by the equation deduced from the energy loss rate using the Mott formula through energy balance equations and adding a limiting phonon relaxation time

$$\tau_{el-ph} = \frac{\pi^2 k_B^2 (p+1)}{6\alpha E_F (T_e^2 + T_L^2)} + \tau_0.$$

- ***Monolayer graphene:*** carrier density independent for a carrier density variation of over an order of magnitude
- ***Bilayer graphene:*** significant carrier density dependence

7. Conclusions

- Energy loss rates in bilayer graphene have been found to follow a T^4 dependence for carrier temperature from 1.4 K up to 100 K.
- Comparisons between bilayer and monolayer graphene: stronger carrier density dependence of the energy loss in bilayer graphene, a crossover point for energy loss, strong carrier density dependence of electron-phonon relaxation time in the bilayer, and carrier density independent behaviour in the monolayer.
- These relationships can provide us with higher tunability of the electron-phonon interactions and the possibility to achieve even faster/slower energy loss for more efficient hot-carrier applications using bilayer graphene.

*Email: r.nicholas1@physics.ox.ac.uk

Notes/References: **1.** Baker *et al.*, Phys. Rev. B **87**, 045414 (2013); **2.** Baker *et al.*, Phys. Rev. B **85**, 115403 (2012); **3.** Zhang *et al.*, Nature **459**, 820 (2009); **4.** Bhargavi and Kubakaddi, Physica E **56**, 123 (2014); **5.** Bhargavi and Kubakaddi, Physica E **52**, 116 (2013); **6.** Katti and Kubakaddi, J. Appl. Phys. **113**, 063705 (2013); **7.** Nyakiti *et al.*, MRS Bull. **37**, 1149 (2012); **8.** Jernigan *et al.*, J. Vac. Sci. Technol., B **30**, 03D110 (2012); **9.** Yager *et al.*, Nano Lett. **13**, 4217 (2013); **10.** Lara-Avila *et al.*, Adv. Mater. **23**, 878 (2011); **11.** Lartsev *et al.*, Appl. Phys. Lett. **105**, 063106 (2014).

Acknowledgments: This work was supported by the UK EPSRC and NMS, EU Graphene Flagship, EMRP GraphOhm, and also by the US Office of Naval Research.

Figure A.3: Poster presented at the Graphene Week 2015, during 22 – 26 June 2015, in Manchester, United Kingdom.

B

Abbreviations

0D, 1D, 2D, 3D	Zero-, One-, Two-, Three-dimensional/dimension(s)
2DEG	Two-dimensional Electron Gas
AC	Alternating Current
AFM	Atomic Force Microscopy
AO	Aqueous Ozone
BG	Bloch-Grüneisen
BNC	Bayonet Neill-Concelman
BSEH	Bootstrap-type Electron Heating
CNP	Charge Neutrality Point
CVD	Chemical Vapour Deposition
DC	Direct Current
DI	Deionised (water)
DMM	Digital Multimeter
DOS	Density of States
EBL	Electron Beam Lithography
FinFET	Fin Field Effect Transistor
HOPG	Highly-oriented Pyrolytic Graphite

I/O	Input/Output
IPA	Isopropyl Alcohol, or Isopropanol
ITO	Indium Tin Oxide
KPM	Kelvin Probe Microscopy
LA	Longitudinal Acoustic (phonons)
LL	Landau level
LO	Longitudinal Optical (phonons)
MIBK	Methyl Isobutyl Ketone
MWCNT	Multi-walled Carbon Nanotube
NMP	N-methyl-2-pyrrolidone
PET	Polyethylene Terephthalate
PID	Proportional-Integral-Derivative (controller)
PMMA	Poly(Methyl Methacrylate)
PTE	Photo-thermoelectric Effect
QHE	Quantum Hall Effect
QILLS	Quasielastic Inter-Landau Level Scattering
RIP	Remote Interfacial Phonon
RTD	Research and Technological Development
S/N	Signal-to-Noise Ratio
SCI	Science Citation Index
SdH	Shubnikov-de Haas (oscillations)
SEM	Scanning Electron Microscopy
SET	Single-electron Transistor
SiC/G	Epitaxial Graphene on Silicon Carbide
SMU	Source-measure Unit
SPP	Surface Polar Phonon
STM	Scanning Tunnelling Microscopy

STS	Scanning Tunnelling Spectroscopy
SWCNT	Single-walled Carbon Nanotube
TMD	Transition Metal Di-chalcogenide
TO	Transverse Optical (phonons)
UV	Ultraviolet (light)
VRH	Variable Range Hopping
VTI	Variable Temperature Insert
WL	Weak Localisation
XPS	X-ray Photoelectron Spectroscopy

N. J. H., 30th September 2016